



**Michigan
Technological
University**

Michigan Technological University
Digital Commons @ Michigan Tech

Dissertations, Master's Theses and Master's Reports

2021

Base Vibration Effects on Additive Manufactured Part Quality: A Study of 3D Printing Onboard U.S. Navy Ships

Nick Jensen

Michigan Technological University, njjensen@mtu.edu

Copyright 2021 Nick Jensen

Recommended Citation

Jensen, Nick, "Base Vibration Effects on Additive Manufactured Part Quality: A Study of 3D Printing Onboard U.S. Navy Ships", Open Access Master's Thesis, Michigan Technological University, 2021.
<https://doi.org/10.37099/mtu.dc.etr/1201>

Follow this and additional works at: <https://digitalcommons.mtu.edu/etr>



Part of the [Acoustics, Dynamics, and Controls Commons](#), and the [Manufacturing Commons](#)

BASE VIBRATION EFFECTS ON ADDITIVE MANUFACTURED PART
QUALITY: A STUDY OF 3D PRINTING ONBOARD U.S. NAVY SHIPS

By

Nicholas J. Jensen

A THESIS

Submitted in partial fulfillment of the requirements for the degree of

MASTER OF SCIENCE

In Mechanical Engineering

MICHIGAN TECHNOLOGICAL UNIVERSITY

2021

© 2021 Nicholas J. Jensen

This thesis has been approved in partial fulfillment of the requirements for the Degree of MASTER OF SCIENCE in Mechanical Engineering.

Department of Mechanical Engineering-Engineering Mechanics

Thesis Co-advisor: *Dr. Gordon G. Parker*

Thesis Co-advisor: *Dr. Jason R. Blough*

Committee Member: *Dr. Vijaya V. N. Sriram Malladi*

Department Chair: *Dr. William W. Predebon*

Contents

List of Figures	ix
List of Tables	xxxvii
Acknowledgments	xxxix
Abstract	xli
1 Introduction	1
1.1 Additive Manufacturing at Large	2
1.2 The U.S. Navy's Interest	3
1.2.1 Origins	3
1.2.2 Trajectories	4
1.2.3 Technological Limitations	4
1.2.4 Plans Moving Forward	6
1.3 Research Target	6
2 The Environment	9
2.1 Military and Marine Factors	10

2.1.1	Sources and Side Effects Onboard Ships	11
2.1.2	Mitigation Schemes	12
2.2	Focus on Vibration	13
3	Vibration Effects on Additive Manufactured (AM) Part Quality	15
3.1	Machine Limitations in Harsh Environments	16
3.1.1	Vibration Mitigation Strategies	17
3.1.2	State of Research	17
3.1.3	Research Approach	18
3.2	Additive Manufactured (AM) Part Quality	20
3.2.1	Factors and Measures	20
3.2.2	Part Roughness	23
3.2.2.1	Preliminary Experimental Observations	24
3.2.2.2	Extended Issues	25
3.3	Experiments	26
3.3.1	Vibration-Sensitive Components	27
3.3.1.1	Initial Testing	27
3.3.1.2	Refined Testing	36
3.3.1.3	Shaker Testing Preparation	42
3.3.1.4	Summary	50
3.3.2	Setup	50
3.3.2.1	Hardware Arrangement	51

3.3.2.2	Part Production Procedure	55
3.3.3	Results and Discussion	56
3.3.3.1	Printer Response from Base Vibration and Machine Vibration	56
3.3.3.2	Part Roughness With and Without Base Vibration	61
3.3.3.3	A Path for Other Printers in Harsh Environments .	63
3.3.3.4	Summary	67
4	Final Remarks	69
4.1	Summary and Conclusion	70
4.2	Work Outlook	72
	References	75
A	Vibration-Sensitive Components Data	79
A.1	Initial Testing	79
A.2	Refined Testing	82
A.3	Shaker Testing Preparation	89
B	Vibration Effects Experiment Data	95
B.1	Dongling Shaker Sweep Boundary Condition Check	95
B.2	Dongling Shaker Passive Isolation Tuning	98
B.3	Dongling Shaker Other Tests	102
B.4	Printed Part Photos	110

List of Figures

- 3.1 Overall approach for this research. The overall factors are common in the AM literature [1]. Our factors are additional for the research at hand. Preliminary experiments indicated vibration effects on part quality to capture, and the sponsor weighed in based on an economical and straightforward interests. 20
- 3.2 Side-view of two AM parts produced by an extrusion process. The top part was generated without vertical base vibration, and the bottom part was produced with it. The roughness values for each were 237.65 μin and 946.15 μin , respectively. The sketches appended to each illustrate the detrimental effects on part surface observed and used to guide the part quality metric selection. “Choppiness” and angularity issues on the highlighted feature were one observed effect. 25
- 3.3 Experimental approach. A modal impact test preceded the vibration effects experiment, identifying vibration-sensitive components to target with vertical base vibration. A passive vibration isolation scheme was implemented as an example for vibration mitigation. 27

3.4	Makerbot Method X fully assembled on the left and a slight disassembly of the plastic accessories on the right.	28
3.5	Accelerometer placement on the print heads. Two single axis accelerometer positions are highlighted, one in the negative X-direction and one in a positive Y-direction. These sensors were used to measure the printer's vibration during operation based on the printing pattern shown in Figure 3.6	29
3.6	Array of parts printed during a vibration experiment. The final parts are the small cylinders shown in the left and the numeric array indicating the spot of each part is shown on the right.	29
3.7	Averaged power spectral density functions (PSDs) for the two accelerometer locations in Figure 3.5 and for several print head locations. The array is a key for the print head location for each measurement. Plotted on the top are curves recorded during each material layer. All 18 plots, nine for each sensor location, are archived in A.1.	31
(a)	Head 4 Spot 01	31
(b)	Head 5 Spot 01	31
(c)	Head 6 Spot 01	31
(d)	Head 4 Spot 06	31
(e)	Head 5 Spot 06	31
(f)	Head 6 Spot 06	31

(g)	Array numbering the print head locations.	31
3.8	Experimental setup for the modal impact test in the horizontal direction. Highlighted are the locations of six single axis accelerometers that were used to record the printer's vibration response in the positive or negative X-directions. These same locations were also impacted with a modal hammer.	32
3.9	Illustration of the limited areas that could be used for measurements and impacts during the horizontal modal impact test. This image shows an impact hammer trying to strike the printer's frame in the Y-direction. However, the area is too tight to get a clear hit.	33
3.10	Horizontal X-direction frequency response function estimates (FRFs) and coherence from modal impact test. The legend shows the output/input location for each function.	34
3.11	Experimental setup for the refined modal impact test that preceded the vibration effects experiment. Accelerometer locations are highlighted on the print bed and print head gantry. Impact and measurement locations are indicated for results discussed in Figure 3.15. The figures represent two asynchronous tests as only six accelerometers were used.	36
3.12	Varying printer configurations for the refined modal impact test. The top set and bottom set of photos represent two asynchronous tests as only six accelerometers were used as described in Figure 3.11.	38

3.13	Mode shapes of the printer manifest on the gantry and print bed. The modal analysis was performed when the printer was in the “centered” <u>bottom</u> configuration as shown in Figure 3.12.	39
(a)	Gantry/trolley mode shape at ≈ 38 Hz. Mode shapes manifest on the gantry. Note that nodes without motion correspond to areas where data was not collected or was corrupted. The main obstruction was the print heads centered on the gantry.	39
(b)	Print bed/build plate mode shape at ≈ 47 Hz.	39
3.14	Frequency response function estimates (FRFs) and coherence compared on the print bed and gantry for varying print bed and print head locations. The varying locations are illustrated in Figure 3.12. The plot titles referring to different locations on the gantry and print bed refer to the node names from the shapes in Figure 3.13. An alternate reference for the geometry used to map the test results can be found in Figure A.3 and Figure A.7.	40
(a)	Comparing the response on the print bed for varying print head positions.	40
(b)	Comparing the response on the print bed for varying print bed positions.	40
(c)	Comparing the response on the gantry for varying print head positions.	40

(d) Comparing the response on the gantry for varying print bed positions.	40
---	----

3.15 Frequency response function estimates (FRFs) in the top left and top right, coherence (left bottom), and phase (right bottom) for the print bed and print head gantry as indicated in Figure 3.11. One FRF from the print head gantry and print bed shows the vibration effects experiment’s targeted resonance area. A mode is present on the print head gantry at ≈ 38 Hz, and another is present on the print bed at ≈ 47 Hz. The shaded region centers on 40.7 Hz with a 10% bound in either direction, which was the vibration effects experiment’s excitation. Another vibration mode is also present at ≈ 58 Hz on the print head gantry.	41
---	----

(a)	41
---------------	----

(b)	41
---------------	----

3.16 Accelerometer locations for the printer disassembly process and tests. The left photo shows the location of the accelerometer on the printer’s gantry. The right photo shows the accelerometer position on the printer’s print bed.	43
--	----

3.17	The procedure for disassembling the printer's accessories. The iterative process was used to assure that the printer's vibration response did not vary following the removal of plastic components. Once the printer's response changed after a disassembly step, the previous disassembly state was determined as final.	43
3.18	Frequency response function estimates (FRFs) for the printer disassembly test. The left figure are measurements from the gantry. The right figure are measurements from the print bed. Step 2 was deemed as the final disassembly state for the printer, while it maintained a similar vibration response to the baseline data. These measurements were recorded according to Figure 3.16. The gantry response was at point 03 and the impact at point 05 according to Figure A.7. The print bed response was at point 05 and the impact at point 05 according to Figure A.3.	44
(a)	Frequency response function estimates (FRFs) on the gantry.	44
(b)	Frequency response function estimates (FRFs) on the print bed.	44
3.19	A table representing the disassembly step details and two photos showing the final disassembly state of the printer. These photos correspond to the state of the printer after disassembly step 2.	45

3.20	Three test setups for modal shaker tests. The left photo has the printer hanging from the ceiling with the shaker exciting the base plate. The middle photo has the printer grounded on a standoff while excited from the bottom by the shaker. The right photo has the printer grounded with the shaker exciting the top left corner of the structure that supports the gantry.	46
(a)	46
(b)	46
(c)	46
3.21	One of the three configurations for the modal shaker tests from Figure 3.20(b). The overall setup is shown on the left with arrows pointed at the accelerometers placed during the tests. The top right photo displays an accelerometer placed on top of the primary print head, recording acceleration in the positive Z-direction. The bottom right photo shows an accelerometer placed under the closest right corner, recording acceleration in the negative Z-direction. In addition, but not visible here, an accelerometer was placed by the excitation location of the shaker measuring in the input in the negative Z-direction. . . .	47
3.22	Crosspower colormap recordings during a manual sine sweep from \approx 25-50 Hz corresponding to Figure 3.21.	48

(a)	Crosspower colormap of the shaker and print head accelerometer. The complex conjugate of the shaker was premultiplied by the print head; both were linear spectrum acceleration data. Key point(s): 40, 46-47 Hz	48
(b)	Crosspower colormap of the shaker and print bed accelerometer. The complex conjugate of the shaker was premultiplied by the print bed; both were linear spectrum acceleration data. Key point(s): 45-47 Hz	48
(c)	Crosspower colormap of the print head and print bed accelerom- eter. The complex conjugate of the print head was premultiplied by the print bed; both were linear spectrum acceleration data. Key point(s): 40, 46-47 Hz	48
(d)	Crosspower colormap of the shaker and print head/print bed crosspower from Figure 3.22(c) accelerometer. The complex con- jugate of the shaker was premultiplied by the print head/print bed crosspower from Figure 3.22(c); both were linear spectrum acceleration data. Key point(s): 45-47 Hz	48
3.23 Printed part results from the modal shaker tests.		49

(a) Top-view of two 3D printed parts. The left was printed with no modal shaker vibration present. The right was printed with the test configuration in Figure 3.20(c) using a sine input at 30 Hz at an amplitude of 0.32 g. 49

(b) Side-views of three 3D printed parts. The top part was printed with no modal shaker vibration present. The middle part was with the test configuration in Figure 3.20(c), using a sine input at 30 Hz at an amplitude of 0.32 g. The bottom part was printed with the test configuration in Figure 3.20(b) with a sine input at 40 Hz with an amplitude of 0.05 g. Highlighted by the circles is layer separation for parts printed with modal shaker vibration, which was not present for the top part printed without vibration. 49

(c) Side-view of two 3D printed parts. The left was printed with no modal shaker vibration present. The right was printed with the test configuration in Figure 3.20(b) using a sine input at 40 Hz at an amplitude of 0.05 g. Highlighted by the circle is a layering difference for the part printed with modal shaker vibration, which was not present for the left part printed without vibration. Notice that the area circled has a line separating the two areas of printed layers. This line represents the moment when the modal shaker was shutoff. Meaning, below the line are layers printed with vibration, and above the line is printed with not vibration. . . 49

(d) Two photos representing catastrophic failure of a part printed with vibration. The isolated part on the left corresponds to the right part in the right photo, which was printed with the test configuration in Figure 3.20(c) using a sine input at 30 Hz at an amplitude of 0.32 g. The left photo was taken while the printer was in operation. Notice the melt areas on the left of the part. This was where the heated print head tip ran into the curled part. The right photo shows a part printed without vibration (left) and with vibration (right). Notice the amplified curling for the part on the right when the shaker vibration was induced. . 49

3.24	Experimental setup of the MakerBot Method X printer rigidly mounted to an ES-10D-240 Dongling shaker. Two mounting plates, separated by aluminum standoffs, provide a mating interface for the printer base and the Dongling head expander/spacer. Two accelerometers/sensors were positioned to measure the vibration of the printer: on top of the primary print head (administers X-Y motion with stepper motors driving the belt-fed gantry) and underneath the center of the print bed (provides Z motion via a leadscrew driven by a stepper motor) where a part would be built.	52
3.25	Crosspower colormap recordings during a sine sweep from ≈ 20 -60 Hz corresponding to Figure 3.24.	54
	(a) Crosspower colormap of the shaker and print head accelerometer. The complex conjugate of the shaker was pre-multiplied by the print head; both were linear spectrum acceleration data. . . .	54
	(b) Crosspower colormap of the shaker and print bed accelerometer. The complex conjugate of the shaker was pre-multiplied by the print bed; both were linear spectrum acceleration data. . . .	54
	(c) Crosspower colormap of the print head and print bed accelerometer. The complex conjugate of the print head was pre-multiplied by the print bed; both were linear spectrum acceleration data. . . .	54

(d) Crosspower colormap of the shaker and print head/print bed crosspower from Figure 3.25(c) accelerometer. The complex conjugate of the shaker was premultiplied by the print head/print bed crosspower from Figure 3.25(c); both were linear spectrum acceleration data. 54

3.26 Geometry of parts produced during vibration experiments. The part's base is approximately 2"x2". The circled area and arrow is the area and the direction the surface roughness measurements were acquired using a Mitutoyo SJ-210 profilometer. This measurement location was used because it was one of the few areas that permitted enough space for the profilometer tool to perform a full measurement stroke. . . . 56

3.27 Diagram and data representing the relative motion between the print head and print bed for two scenarios: with and without vertical base vibration. Rapid motion from the print head travel set to a maximum of 500 $\frac{mm}{s}$ for inducing machine vibration in each case. Relative motion was measured between the print head and print bed accelerometers (see Figure 3.24). The base vibration scenario was excited by a 0.1 g sinusoid at 40.7 Hz for the entire production. The plots show the results for approximately one extruded material layer. 58

(a) Relative motion without vertical base vibration. 58

(b) Relative motion with vertical base vibration. 58

(c) MakerBot Method X printer sketch of motion components targeted in an experiment. The print bed enables Z-direction motion and X-Y motion is permitted by the print head gantry. The coordinate frames present on the print bed and print head indicate where two accelerometers were positioned for measuring and calculating relative motion between them. 58

3.28 Relative motion measured between the print head and print bed accelerometers (see Figure 3.24). The base vibration scenario was excited by a 0.1 g sinusoid at 40.7 Hz for the entire production. The curves are maximum values for data recorded while the printer applied one extruded material layer. Notice the peak of each curve is near the large energy resonance that was identified in the refined modal impact test. In addition, the maximum value for the base vibration case is over $10\times$ larger than without base vibration. Rapid motion from the print heads set to a maximum travel speed of $500 \frac{mm}{s}$ induced machine vibration in each case. 59

3.29 Histogram of part roughness measurements R_a collected for parts printed with (qty: 10) and without base vibration (qty: 33). Parts printed with vertical base vibration had amplitude inputs between 0.0325 and 0.13 g. Different sample sizes were due to the long print time for the base vibration test that required an observer. Bin values are counts for a range of roughness values. Included are the median values for each sample set. Both data sets have a similar skewness. However, the median of parts printed with base vibration is two times higher than those printed without base vibration. Meaning, parts are expected to be of lower quality when printed amidst base vibration. Lastly, the spread of the parts printed with base vibration (Std Dev: 349.01 μin) is nearly double that of the parts without base vibration (Std Dev: 187.71 μin). This comparison indicates that part quality is also less predictable when vertical base vibration is present. 62

3.30 Relative motion between the print head and print bed for two scenarios: with and without passive vibration isolation. The data was measured between the print head and print bed accelerometers (see Figure 3.24). 66

(a) No isolation. 66

(b) With 3 sponge rubber hockey puck isolation. 66

(c) The curves are maximum values for data recorded while the printer applied one extruded material layer. One curve was from a test with passive isolation and the other without. Both resulted from vertical base vibration on the printer at 0.1 g and 40.7 Hz. Circled at 46 Hz is a new mode that is an artifact of using passive isolation. This new mode is still a factor of 22 lower than the targeted frequency of 40.7 Hz. Notice the 38% reduction of the response once isolation is introduced. 66

3.31 An adapted overall approach of this research indicates how future work can use the present results to move directly from a part quality metric decision to testing vibration effects and mitigating them. The present results support the assumption that relative vertical print bed and head vibration dominate an extrusion printer’s vibration response and should be the focus for applying a vibration mitigation scheme. . . 68

4.1 Potential future of AM deployed in harsh environments. 74

A.1 Averaged power spectral density functions (PSDs) for the Spot 01 accelerometer location from Figure 3.5. Plotted are curves recorded during each material layer for a given print head position as in Figure 3.6. 80

(a) Head 7 80

(b) Head 8 80

(c)	Head 9	80
(d)	Head 4	80
(e)	Head 5	80
(f)	Head 6	80
(g)	Head 1	80
(h)	Head 2	80
(i)	Head 3	80

A.2	Averaged power spectral density functions (PSDs) for the Spot 06 accelerometer location from Figure 3.5. Plotted are curves recorded during each material layer for a given print head position as in Figure 3.6.	81
(a)	Head 7	81
(b)	Head 8	81
(c)	Head 9	81
(d)	Head 4	81
(e)	Head 5	81
(f)	Head 6	81
(g)	Head 1	81
(h)	Head 2	81
(i)	Head 3	81

A.3	Print bed/build plate geometry. This layout was used for recording vibration data according to specific nodes.	82
A.4	Stabilization diagram for modal analysis with the print bed vibration data. Pole selections are highlighted.	83
A.5	Experimental and synthesized frequency response function estimates (FRFs) for the print bed modal analysis. Pole selections are highlighted.	84
	(a)	84
	(b)	84
	(c)	84
	(d)	84
	(e)	84
A.6	Mode shapes manifest on the print bed.	85
	(a)	85
	(b)	85
	(c)	85
A.7	Gantry/trolley geometry. This layout was used for recording vibration data according to specific nodes.	86
A.8	Stabilization diagram for modal analysis with the gantry vibration data. Pole selections are highlighted.	86

A.9	Experimental and synthesized frequency response function estimates (FRFs) for the gantry modal analysis. Pole selections are highlighted.	87
(a)	87
(b)	87
(c)	87
(d)	87
(e)	87
A.10	Mode shapes manifest on the gantry. Note that nodes without motion correspond to areas where data was not collected or was corrupted. The main obstruction was the print heads centered on the gantry.	88
(a)	88
(b)	88
(c)	88
(d)	88
A.11	Crosspower colormap recordings during a manual sine sweep from \approx 25-50 Hz.	90
(a)	Crosspower colormap of the shaker and print head accelerometer. The complex conjugate of the shaker was pre-multiplied by the print head; both were linear spectrum acceleration data. Key point(s): 40, 46-47 Hz	90

(b)	Crosspower colormap of the shaker and print bed accelerometer. The complex conjugate of the shaker was premultiplied by the print bed; both were linear spectrum acceleration data. Key point(s): 45-47 Hz	90
(c)	Crosspower colormap of the print head and print bed accelerometer. The complex conjugate of the print head was premultiplied by the print bed; both were linear spectrum acceleration data. Key point(s): 40, 46-47 Hz	90
(d)	Crosspower colormap of the shaker and print head/print bed crosspower from Figure 3.22(c) accelerometer. The complex conjugate of the shaker was premultiplied by the print head/print bed crosspower from Figure 3.22(c); both were linear spectrum acceleration data. Key point(s): 45-47 Hz	90
A.12 Colormap recordings during a manual sine sweep from ≈ 25 -50 Hz.		91
(a)	Colormap of the shaker linear spectrum acceleration data. Key point(s): 46-47 Hz	91
(b)	Colormap of the print head linear spectrum acceleration data. Key point(s): 34-47 Hz	91
(c)	Colormap of the print bed linear spectrum acceleration data. Key point(s): 24-28, 37-47 Hz	91
A.13 Crosspower colormap recordings during a sine input at ≈ 40 Hz. . .		92

(a)	Crosspower colormap of the shaker and print head accelerometer. The complex conjugate of the shaker was premultiplied by the print head; both were linear spectrum acceleration data.	92
(b)	Crosspower colormap of the shaker and print bed accelerometer. The complex conjugate of the shaker was premultiplied by the print head; both were linear spectrum acceleration data.	92
(c)	Crosspower colormap of the print head and print bed accelerom- eter. The complex conjugate of the shaker was premultiplied by the print head; both were linear spectrum acceleration data.	92
(d)	Crosspower colormap of the shaker and print head/print bed crosspower from Figure 3.22(c) accelerometer. The complex con- jugate of the shaker was premultiplied by the print head/print bed crosspower from Figure 3.22(c); both were linear spectrum acceleration data.	92
A.14	Colormap recordings during a sine input at ≈ 40 Hz.	93
(a)	Colormap of the shaker linear spectrum acceleration data.	93
(b)	Colormap of the print head linear spectrum acceleration data.	93
(c)	Colormap of the print bed linear spectrum acceleration data.	93
B.1	Crosspower colormap recordings during a sine sweep from ≈ 20 -60 Hz corresponding to Figure 3.24.	96

(a)	Crosspower colormap of the shaker and print head accelerometer. The complex conjugate of the shaker was premultiplied by the print head; both were linear spectrum acceleration data.	96
(b)	Crosspower colormap of the shaker and print bed accelerometer. The complex conjugate of the shaker was premultiplied by the print bed; both were linear spectrum acceleration data.	96
(c)	Crosspower colormap of the print head and print bed accelerom- eter. The complex conjugate of the print head was premultiplied by the print bed; both were linear spectrum acceleration data.	96
(d)	Crosspower colormap of the shaker and print head/print bed crosspower from Figure 3.25(c) accelerometer. The complex con- jugate of the shaker was premultiplied by the print head/print bed crosspower from Figure 3.25(c); both were linear spectrum acceleration data.	96
B.2	Colormap recordings during a sine sweep from ≈ 20 -60 Hz.	97
(a)	Colormap of the shaker linear spectrum acceleration data.	97
(b)	Colormap of the print head linear spectrum acceleration data.	97
(c)	Colormap of the print bed linear spectrum acceleration data.	97
B.3	Crosspower colormap recordings during a sine sweep corresponding to Figure 3.24.	99

(a)	Crosspower colormap of the shaker and print head accelerometer. The complex conjugate of the shaker was pre-multiplied by the print head; both were linear spectrum acceleration data.	99
(b)	Crosspower colormap of the shaker and print bed accelerometer. The complex conjugate of the shaker was pre-multiplied by the print bed; both were linear spectrum acceleration data.	99
(c)	Crosspower colormap of the print head and print bed accelerom- eter. The complex conjugate of the print head was pre-multiplied by the print bed; both were linear spectrum acceleration data.	99
(d)	Crosspower colormap of the shaker and print head/print bed crosspower from Figure B.3(c) accelerometer. The complex con- jugate of the shaker was pre-multiplied by the print head/print bed crosspower from Figure B.3(c); both were linear spectrum acceleration data.	99
B.4	Colormap recordings during a sine sweep.	100
(a)	Colormap of the shaker linear spectrum acceleration data.	100
(b)	Colormap of the print head linear spectrum acceleration data.	100
(c)	Colormap of the print bed linear spectrum acceleration data.	100
B.5	Crosspower colormap recordings during a sine sweep corresponding to Figure 3.24.	101

(a)	Crosspower colormap of the shaker and print head accelerometer. The complex conjugate of the shaker was pre-multiplied by the print head; both were linear spectrum acceleration data.	101
(b)	Crosspower colormap of the shaker and print bed accelerometer. The complex conjugate of the shaker was pre-multiplied by the print bed; both were linear spectrum acceleration data.	101
(c)	Crosspower colormap of the print head and print bed accelerom- eter. The complex conjugate of the print head was pre-multiplied by the print bed; both were linear spectrum acceleration data.	101
(d)	Crosspower colormap of the shaker and print head/print bed crosspower from Figure B.5(c) accelerometer. The complex con- jugate of the shaker was pre-multiplied by the print head/print bed crosspower from Figure B.5(c); both were linear spectrum acceleration data.	101
B.6	Colormap recordings during a sine sweep.	102
(a)	Colormap of the shaker linear spectrum acceleration data.	102
(b)	Colormap of the print head linear spectrum acceleration data.	102
(c)	Colormap of the print bed linear spectrum acceleration data.	102
B.7	Colormap recordings.	103
(a)	Colormap of the print head linear spectrum acceleration data.	103
(b)	Colormap of the print bed linear spectrum acceleration data.	103

(c)	Colormap of the relative motion between the print head and print bed linear spectrum acceleration data.	103
(d)	Colormap of the relative motion between the print head and print bed linear spectrum displacement data.	103
B.8	Colormap recordings.	104
(a)	Colormap of the print head linear spectrum acceleration data.	104
(b)	Colormap of the print bed linear spectrum acceleration data. .	104
(c)	Colormap of the relative motion between the print head and print bed linear spectrum acceleration data.	104
(d)	Colormap of the relative motion between the print head and print bed linear spectrum displacement data.	104
B.9	Colormap recordings.	106
(a)	Colormap of the print head linear spectrum acceleration data.	106
(b)	Colormap of the print bed linear spectrum acceleration data. .	106
(c)	Colormap of the relative motion between the print head and print bed linear spectrum acceleration data.	106
(d)	Colormap of the relative motion between the print head and print bed linear spectrum displacement data.	106
B.10	Colormap recordings.	107
(a)	Colormap of the print head linear spectrum acceleration data.	107
(b)	Colormap of the print bed linear spectrum acceleration data. .	107

(c)	Colormap of the relative motion between the print head and print bed linear spectrum acceleration data.	107
(d)	Colormap of the relative motion between the print head and print bed linear spectrum displacement data.	107
B.11	Colormap recordings.	109
(a)	Colormap of the print head linear spectrum acceleration data.	109
(b)	Colormap of the print bed linear spectrum acceleration data. .	109
(c)	Colormap of the relative motion between the print head and print bed linear spectrum acceleration data.	109
(d)	Colormap of the relative motion between the print head and print bed linear spectrum displacement data.	109
B.12	Top-view of PETG part photos for various testing scenarios.	110
(a)	No vibration. No isolation. Ra roughness: 237.65 μin	110
(b)	0.13 g vibration at 40.7 Hz. No isolation. Ra roughness: 946.15 μin	110
(c)	0.0325 g vibration at 40.7 Hz. 3 sponge hockey puck isolation. Ra roughness: 290.64 μin	110
(d)	0.0325 g vibration at 40.7 Hz. No isolation. Ra roughness: 849.71 μin	110
B.13	Top-view of PETG part photos with camera flash for various testing scenarios.	111

(a) No vibration. No isolation. Ra roughness: 237.65 $\mu\text{in.}$	111
(b) 0.13 g vibration at 40.7 Hz. No isolation. Ra roughness: 946.15 $\mu\text{in.}$	111
(c) 0.0325 g vibration at 40.7 Hz. 3 sponge hockey puck isolation. Ra roughness: 290.64 $\mu\text{in.}$	111
(d) 0.0325 g vibration at 40.7 Hz. No isolation. Ra roughness: 849.71 $\mu\text{in.}$	111
B.14 Front-view of PETG part photos for various testing scenarios.	112
(a) No vibration. No isolation. Ra roughness: 237.65 $\mu\text{in.}$	112
(b) 0.13 g vibration at 40.7 Hz. No isolation. Ra roughness: 946.15 $\mu\text{in.}$	112
(c) 0.0325 g vibration at 40.7 Hz. 3 sponge hockey puck isolation. Ra roughness: 290.64 $\mu\text{in.}$	112
(d) 0.0325 g vibration at 40.7 Hz. No isolation. Ra roughness: 849.71 $\mu\text{in.}$	112
B.15 Left-view of PETG part photos for various testing scenarios.	112
(a) No vibration. No isolation. Ra roughness: 237.65 $\mu\text{in.}$	112
(b) 0.13 g vibration at 40.7 Hz. No isolation. Ra roughness: 946.15 $\mu\text{in.}$	112
(c) 0.0325 g vibration at 40.7 Hz. 3 sponge hockey puck isolation. Ra roughness: 290.64 $\mu\text{in.}$	112

(d) 0.0325 g vibration at 40.7 Hz. No isolation. Ra roughness: 849.71

$\mu\text{in.}$ 112

List of Tables

3.1	Experiment parameters for the vibration test while printing parts in an array with accelerometers on the print heads.	30
3.2	Experiment parameters for the horizontal modal impact test.	32
3.3	Experimental parameters for the refined modal impact test.	38
3.4	Testing parameters for the printer disassembly tests.	44
3.5	Experiment parameters for the modal shaker tests.	46
3.6	Experiment parameters for a sweep test on the Dongling shaker to check the new boundary conditions.	53
3.7	Experiment parameters for a test on the Dongling shaker to compare the sources of vibration.	57
B.1	Experiment parameters for tests on the Dongling shaker to tune the passive isolation strategy.	98
B.2	Experiment parameters for tests on the Dongling shaker.	103
B.3	Experiment parameters for tests on the Dongling shaker.	104
B.4	Experiment parameters for tests on the Dongling shaker.	105
B.5	Experiment parameters for tests on the Dongling shaker.	107

B.6 Experiment parameters for tests on the Dongling shaker. 108

Acknowledgments

Beyond anyone I could thank, I thank God for His grace and love towards me. They are the best things I have ever experienced and sustain me every day. Thank you, my lovely Sabrina, for your support, friendship, and encouragement over these last few years. Thank you, Dr. Gordon Parker, Dr. Jason Blough, and Dr. Sriram Malladi, for being a part of my committee and for all your support behind the scenes. There are many people to thank from Michigan Tech who supported this work. A few people are: Marty Toth and Jon Lund from the machine shop for their patience during my 3-day process of machining the printer mounting plates, Cora Taylor for her help with the experimental setup on the shaker, Karavela Zeiter, Julia Barnes, and Artemis Allison for their editing assistance throughout the writing process. Thank you to my family, brothers and their families, my in-laws, and especially my parents, Pete and Louanne. To my friends, thank you for being a part of my life and supporting me these last few years. Thank you to the project sponsors, the folks at the ATR Corporation, and the Naval Sea Systems Command. It has been a great experience working with you all. This work was supported by Naval Sea Systems Command (NAVSEA). The views and conclusions contained in this document are those of the authors and should not be interpreted as representing the official policies, either expressed or implied, of the Naval Sea Systems Command (NAVSEA).

Abstract

The current landscape of manufacturing is evolving because of technology like additive manufacturing (AM). The mobility and compactness of AM are what make it desirable for many industry sectors. The U.S. Navy has shown interest in deploying AM on ships as it could alleviate their dependency on off-route docking to recharge supplies. However, the U.S. Navy's aspiration is currently hindered due to harsh ship-borne environments that degrade AM part quality.

This thesis focuses on vertical base vibration effects on AM part quality. An introduction is first given in Chapter 1 to familiarize the reader with the U.S. Navy's predicament. The harsh environmental factors of marine military environments are discussed in Chapter 2, centered on vibration < 100 Hz. With the context established, Chapter 3 narrows in on the experimental approach to 1) understand how vertical base vibration affects AM part quality and 2) provide an example for how to mitigate the vibration effects with a passive isolation scheme. The overall approach of Chapter 3 is a suggested path for inspecting other AM printers and applying mitigation strategies for deployment in harsh environments. Finally, the thesis concludes with a discussion on the main results and future work to continue or extend this research.

Chapter 1

Introduction

This chapter provides the necessary background for this thesis by describing Additive Manufacturing (AM) 's sensational characteristics that have attracted many academic and industry users, including the United States Navy. Introducing the research focus provides the backbone for the remainder of this work. The purpose of this chapter is to frame the context for the research so the reader can grasp, appreciate, and hopefully benefit from the detailed accomplishments of this work.

1.1 Additive Manufacturing at Large

Additive manufacturing (AM) has revolutionized manufacturing possibilities over the last few decades through its elegant approach to consolidate production to a single machine. Though AM frequently functions as a utility for rapid prototyping (RP), it rivals traditional subtractive manufacturing (SM) at small-scale production as the machinery and processes have become more reliable.

AM - also known as 3D printing - sets itself apart from SM in that it simplifies supply chains and logistics through efficient and adaptable techniques [2]. While SM exhibits high throughput characteristics via multi-step raw material removal with several machines, AM directly builds a device from the ground up with one machine, minimizing production steps for a finished product. This aspect of AM has been attractive for many parties, especially the U.S. Navy.

1.2 The U.S. Navy's Interest

1.2.1 Origins

2013 marked the beginning of the U.S. Navy's consideration of adopting technology from the evolving AM field [3]. Service members from other military branches had started to wonder about how AM could alleviate burdens they experience while deployed. Army Lt. Col. Jeckell described the immense burden soldiers bear due to managing large part stockpiles to remain functional while deployed [4]. Jeckell's precise identification of this hindrance, typical for other military branches as well [4], aligns with what the U.S. Navy began to pursue in 2016 [5].

By 2016, the U.S. Navy caught on to AM's potential to improve their operations. Specifically, they were captivated by how AM could abbreviate production and enable novel and economical designs for responsiveness to evolving warfare needs [5]. Convinced of this approach, the Navy asserted that, "coupled with digital design and manufacturing, AM will improve warfighting systems in ways never before imagined" [5].

1.2.2 Trajectories

Ever since the Navy set off to deploy AM on ships, instances have come up where they have attempted to realize AM's potential practically. In 2014, a crew onboard the USS Essex was equipped with a 3D printer and promptly created products to assist in their daily activities [6]. Useful items ranged from “disposable medical supplies (think plastic syringes), to a new cap they designed for an oil tank, to model planes to move around their mockup of the flight deck...” [6]. Though these simple products were standard for what many hobbyists worldwide have pursued with their 3D printers, they marked a step towards implementing AM on ships at sea.

1.2.3 Technological Limitations

AM seemed promising for the Navy until Lt. Benjamin Kohlmann – a member of the initial project to deploy 3D printers on U.S Navy ships in 2014 [6] – pointed out a known limitation of AM thus far. Kohlmann was pleased by these AM parts' value but was disappointed that nothing like spare parts for airplanes was on the horizon [6]. Others who hoped for AM to enhance the Navy's capabilities also recognized this shortcoming [6, 7, 8].

The main concern is that AM could not produce parts that can withstand the dynamic

environment and the extended life expectation of marine conditions. The marine industry is not the only industry sector that worries about this as it is also a concern for aviation and aerospace industries where part expectations are similar. However, the U.S. Navy has stated [5] one unique challenge as they envision 3D printers on board their ships. This challenge is *printing* parts amidst the harsh environment on board a ship.

The Navy's implementation plan's primary goal from 2016-2017 highlights the Navy's distinct concern [5]. In the implementation plan, the Navy desires simplified supply chains through the use of onboard 3D printers. This adaptive supply chain management approach is beyond the Navy's experiences thus far and could enable them to achieve their goals as laid out in the implementation plan. However, most "off-the-shelf" AM equipment rely on gravity to assist in leveling part structures. This requirement for a calm environment is far from present in the dynamic nature onboard a ship where large amplitude motion/vibration is normal [7].

Though it seems that harsh marine environments are a considerable roadblock for the onboard deployment of AM, resolving this issue may not be as far out as Alan Epstein – vice-president of Pratt & Whitney, a large government contractor – thought. He said, "come back in 20 years" to see 3D printers on every ship [6]. With this paper's research, having printers on ships may happen much sooner than 2034¹.

¹20 years from the written article [6]

1.2.4 Plans Moving Forward

The U.S. Navy is committed to resolving the issue of vibration affecting AM production to carry on with their aspirations enabled by AM [5]. They have recently distilled their pursuit into actionable projects. A project called the “Ship Vibration Mitigation for Additive Manufacturing Equipment” was launched at the beginning of 2020, which has funded this research.

1.3 Research Target

The crux of this research is examining how base vibration onboard U.S. Navy ships affects AM part quality and how to mitigate the detrimental effects. This knowledge levels up the understanding of how typical AM machines respond to their environment, not by any *new* analysis or theory. Instead, this exploratory work uses *current* methods for machine vibration problems and provides narrowed insight for anyone interested in placing AM equipment in harsh environments without sacrificing part quality.

The remainder of this thesis unfolds by characterizing the naval environment that AM equipment shall be exposed to and how this environment affects the quality of

AM parts produced in it. An example of mitigating adverse effects is given and the thesis concludes with implications of this research and discussion for building on these understandings.

Chapter 2

The Environment

This chapter explores the dominant properties of environmental vibration typical for naval environments. An explanation of military and marine factors describes the fierce events that cause troubles with all types of onboard machinery during operation. Vibration, with a threshold of approximately 100 Hz, emerges as the main character for the following discussions. This chapter stresses serious vibration sources of naval environments to establish the experimental context of the subsequent chapter.

2.1 Military and Marine Factors

Military scenarios are generally dynamic and relatively extreme in terms of forces, weather, and temperature. Explosions, intense heat, and chemical fallout are prevalent in military settings. Equipment designers often account for these intense factors by creating military technology with maximized reliability and robustness not matched in other types of environments. This expectation should be no different for AM equipment.

The collision of many environmental factors makes marine environments possibly the most extreme conditions that can hurt humans and operating machinery. These situations often harm humans and equipment with severe disruptive forces from many sources, including waves slamming [9], discharged explosives from or onto the ship, propeller and drivetrain vibration, structural resonance from vortex shedding, aircraft takeoffs, and onboard machinery vibration [10]. Many of these disruptions are side effects of the improved performance of military ships.

2.1.1 Sources and Side Effects Onboard Ships

Robustness, speed, and agility are all crucial factors for the design of military ships, and each comes with limitations that can hinder AM production. Durable materials such as steel were historically used to make ships tough but resulted in a loss of agility. Modern engineering analysis tools have enabled ship designers to create faster ships utilizing lighter or less material [10], but side effects arise from a loss of structural rigidity. Lack of structural rigidity is neither inherently good nor bad. All materials lack rigidity to some degree as nothing is entirely rigid. However, ships can become trouble-stricken when their structure gets excited by the impacts and vibration present during regular operation. Ship flexibility is unavoidable and is the modern ships' current state, especially when speed is a priority. Therefore, it is crucial to understand what sources in the ship's environment excite such resonances and inevitably affect onboard 3D printing.

Vibration onboard ships have been researched with several sources identified. Carlton et al. identified the typical sources of vibration on a ship as: "diesel engines, shaft-line dynamics, propeller radiated pressures and bearing forces, air conditioning systems, manoeuvring devices such as transverse propulsion units [bow thrusters], cargo handling and mooring machinery, vortex shedding, intake and exhausts, slamming" [10]. Other authors agree regarding machinery factors [11, 12], with Borelli

et al. [11] categorizes the machines into main engines and auxiliaries. Auxiliaries include generators, pumps, boilers, cargo processing, and ventilation [11] but are not typically the primary source of ship vibration. The ship's structural vibration modes seem to be the worse cause of vibration among these sources, primarily excited by main engines, vortex shedding, slamming, and propulsion mechanisms [9, 10, 12].

2.1.2 Mitigation Schemes

As many sources of noise and vibration are present, there are many theories to mitigate such disturbances. Some authors agree that carefully designed hulls could minimize structural modes by minimizing how much the ship resonates and therefore reduce the effect of excitations from vortex shedding and slamming, which depend on hull shape [10, 11]. Borelli et al. recommended using resilient mounts and repositioning the source for large noise and vibration perpetrators such as the main engines to isolate them from the rest of the ship [11]. Dylejko et al. suggested an approach specifically for propulsion drivetrain vibration mitigation by employing a vibration absorber [12]. Regardless of the mitigation scheme, vibration remains onboard ships and needs to be understood for how it affects onboard AM equipment.

2.2 Focus on Vibration

This research focused on vibration exclusively because it had been previously identified as an issue for AM on Navy ships [13]. Specifically, this research is concerned with vibration up to 100 Hz. The reason for this focus is based on technical standards and intuition. Two documents informed this decision: one from Lloyd's Register [14] and the military standard MIL-STD-810G [15]. In both documents, vibration < 25 Hz is identified as a typical bandwidth due to the ship's global structural vibration response. Vibration slightly higher than 25 Hz is also pointed to but not as often as it depends on localized structures' resonant behavior. Higher frequency vibration is often induced by the main engines and propulsion systems. 100 Hz was chosen as a maximum because it encompassed some of the most prominent vibration ranges as specified by Lloyd's Register and the MIL-STD-810G, and it provided a buffer at the higher end, so no vibration modes near the 25 Hz range would be neglected in the analysis. These ranges are also reasonable because higher frequencies damp out quicker as they transmit through joints and damping elements on a ship.

Chapter 3

Vibration Effects on Additive

Manufactured (AM) Part Quality¹

This chapter is the crux of this thesis, with experiments performed on an extrusion-type AM printer to understand and mitigate the base vibration effects on part quality. The opening section describes how the printer was considered a precision machine and how extensive literature on this topic is applicable. The chapter's focus is then stated, followed by a section justifying part roughness to measure part quality. Three experimental steps were taken: to identify vibration-sensitive components, investigate the vibration of the sensitive components and how they influence the part quality, and application of a passive isolation strategy to minimize the effects that degrade part

¹The material contained in this chapter will be submitted to *Additive Manufacturing*

quality. The chapter closes with the experimental results, discussions, and a summary before transitioning to the thesis's final chapter. The purpose of this chapter is to present the central results of this thesis and extrapolate implications for the U.S. Navy's deployment of AM printers onboard ships.

3.1 Machine Limitations in Harsh Environments

In general, 3D printers can classify as precision machines, which means that machine performance can be undermined without mitigating vibration [16]. The vibration source affecting precision machines could be from the machine or its base. Machine vibration is often due to the rapid movement of machine components, while base vibration originates from external factors like nearby vibrating machines. Both of these effects on machine performance have been studied for decades [16, 17]. Although the ideal solution for such devices is to redesign the entire environment to minimize environmental noise (i.e., an isolated building, foundation, floor, or room) [18], it is typically high-cost and excessive for most scenarios. Therefore, efforts to mitigate environmental harshness affecting precision machine performance pursue two common strategies: 1) adaptive machine control that compensates for the machine or base vibration and 2) isolating the machine, actively or passively, from the machine or base vibration.

3.1.1 Vibration Mitigation Strategies

Duan et al. carried out the first approach using a feedforward control algorithm informed by the printer's near-future route to minimize an extrusion AM printer's trajectory during production [19]. Rivin engaged the second method by passive and active isolation and suggested that passive isolation is sufficient for most scenarios [20]. Active isolation, Rivin said, is beneficial when a process requires extreme machine precision [20]. Though isolation has primarily been pursued as a mitigation strategy to *decouple* the equipment's vibration source from the structural vibration modes, recent work has shown how careful *coupling* of the isolation devices with the machine's structural vibration modes can reduce unwanted vibration for horizontal and rocking motion [21].

3.1.2 State of Research

Regardless of the scheme to mitigate vibration affecting a precision machine, understanding a machine's vibration response is vital [18, 22]. Minimal research is present in the literature about vibration affecting extrusion-type 3D printers. Two groups investigated how fast repositioning of AM print heads excited the printer's structural vibration modes and affected part surface roughness [23, 24]. Nevertheless, neither

group of authors explored base vibration effects and how it contributes to AM part quality.

3.1.3 Research Approach

This chapter has four main points. All four are based on experiments with an extrusion-type printer:

1. Relative vertical motion of a printer's bed and gantry dominate vibration effects on part quality.
2. Vertical base vibration dominates a printer's vibration response, NOT machine vibration.
3. Part quality deteriorates with base vibration, qualitatively and quantitatively.
4. A passive isolation scheme mitigates the vibration effects and improves part quality based on an experimental demonstration.

The first point resulted from pursuing a series of tests ending with a refined modal impact test to identify vibration-sensitive printer components. High-energy vibration modes appeared on the print bed and print head at ≈ 40 Hz. These components were then experimentally targeted to explore vertical base vibration effects on part

quality. The second point is from considering two tests during AM parts production: one excited the printer's vibration modes with machine vibration and vertical base vibration; the other excited the printer's vibration modes with machine vibration only. Post-processing compared the printer's bed and head relative vertical motion for each test to investigate which vibration source dominated the printer's response. The third point is based on considering the print bed and print head relative vertical motion during production versus part surface roughness. The printer's bed and head relative motion was recorded while the printer discharged a material layer. Data were extracted from the relative motion record to inspect the printer's peak movement irrespective of its configuration. Part roughness was observed and measured to assess part quality. The final point involved implementing a passive isolation scheme to mitigate the base vibration effects on AM part quality.

The remainder of this chapter describes the approach for measuring AM part quality, the process of identifying vibration-sensitive printer components, the experiment considering the source of vibration that leads to part quality degradation, and implementing a passive vibration isolation solution to demonstrate improved AM part quality. The overall approach is highlighted in Figure 3.1. The chapter concludes by discussing the experimental results and the implications for other AM equipment that could be placed in vibratory settings.

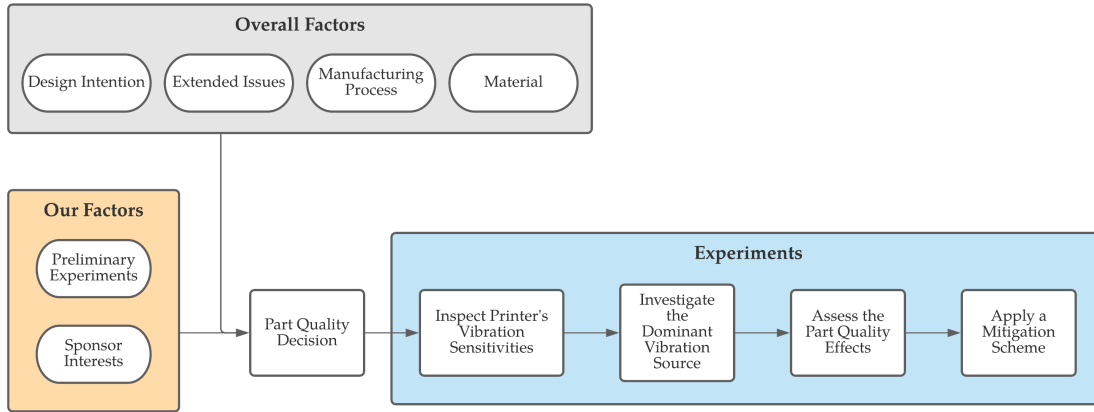


Figure 3.1: Overall approach for this research. The overall factors are common in the AM literature [1]. Our factors are additional for the research at hand. Preliminary experiments indicated vibration effects on part quality to capture, and the sponsor weighed in based on an economical and straightforward interests.

3.2 Additive Manufactured (AM) Part Quality

3.2.1 Factors and Measures

This study focused on part roughness as an identifier of part quality, but in most cases, the quality of AM parts is subjective. Overall factors in Figure 3.1 influence how part quality is assessed; They include design intention, extended issues, manufacturing process, and material [1]. Design intention is often the focus for assessing part quality, for example, strength, durability, density, number and type of allowable defects, and dimensional accuracy. One prolific design concern is part strength, which can be insightful for understanding if, how, and when a part may fail in its prescribed

environment. On a different note, identifying and minimizing part defects [25, 26] has also been essential to AM processes as these processes focus on systematic ways of creating an object, so it is efficient and reproducible. Extended issues, an issue that is an indirect result of some direct issue, can influence how one chooses a part quality metric. Surface quality is one instance where a part's surface can be measured directly and indicate extended part quality issues like geometric inaccuracy and part malfunction [1].

On the other hand, AM processes have specific traits that influence a final part and its quality. Current AM processes include material extrusion, powder fusion, material jetting, binder jetting, energy deposition, vat photo-polymerization, and sheet lamination [7]. Consider powder fusion, comparable to the process of casting - but as an incremental approach - the powdered raw material is melted in layers and cooled to take the shape of the desired object. According to Echeta et al. [27], the porosity of lattice structures made from powder fusion is imperative to consider for a part's life expectancy. They say, "under load, pores form stress concentrations. . . [that] can have a significant effect on fatigue properties". This claim would make a porosity test that measures the "unintentional void within the lattice structure/ratio of pore volume to material volume" [27], an appropriate candidate for identifying part quality. Similar to powder fusion, binder jetting is an AM process that uses a binder for each layer to adhere to the overall object instead of melting/welding the material together. This process is also concerned with the final part's porosity

pertaining to its overall function and life. Lastly, sheet lamination, a process similar to laying fiberglass for a composite material, is prone to poor performance in the shear direction [7]. Therefore, one inspection may include a shear strength test to assess a part's quality.

Material choice also plays a part in how part quality is evaluated. Plastics, metals, ceramics, and composite AM materials have varying mechanical and physical properties resulting in different perspectives when analyzing the part quality of each. Together these factors influence how one would decide to measure part quality for a given situation. Regardless of a study's breadth to establish a catch-all part metric, the situation still resolves to subjectivity, as indicated by Udroui et al. [1].

For this study, two additional factors from Figure 3.1 were considered before selecting part surface roughness as the part quality metric: preliminary experimental observations and sponsor interest corresponding to common knowledge. Preliminary experiments vibrated the printer and informed the decision by indicating surface quality effects. Sponsor interest distilled from intuition and agreement in the AM field [1]. Both factors are discussed in the next section.

3.2.2 Part Roughness

This research focused on extrusion-based PETG parts for use on U.S. Naval ships [5, 13]. The chosen quality metric was average surface roughness (Equation 3.1). Equation 3.1 comprises measured distances of orthogonal points $|z(x)|$ along a surface profile x . The points are averaged for the surface length l to give a unitless surface roughness value R_a .

$$R_a = \frac{1}{l} \int_0^l |z(x)| dx \quad (3.1)$$

The metric was chosen for four main reasons:

1. It visually characterized one of the main effects observed during preliminary vibration testing on a 3D printer.
2. The research sponsor desired an assessment to measure part quality at a qualitative level visually.
3. The research sponsor desired a part quality metric that could be measured with a simple and inexpensive profilometer tool.

4. It would indicate further issues like geometric inaccuracies.

3.2.2.1 Preliminary Experimental Observations

Figure 3.2 illustrates the first point that surface roughness was observed during preliminary experiments; two parts are displayed from a side-view, one printed with and one printed without vertical base vibration. The top part was created without vertical base vibration, and the bottom part with it. The top part had a roughness of $237.65 \mu\text{in}$, while the bottom part $946.15 \mu\text{in}$. Further details of the parts and the corresponding print process are described in Section 3.3.2.2 and Section 3.3.2. Annotating both parts are circles that emphasize the effects of vertical base vibration. One noticeable difference between these two is the “choppiness” of the layers at the edge of the feature indicated. Indirectly, the roughness measurement also captures angularity issues, as shown by the 90° features in Figure 3.2. The highlighted region has a straight edge in the photo where no vibration was present, whereas the part printed with vibration fails to keep the feature straight. These observations provided sufficient evidence for confidence in selecting this metric to gauge part quality.

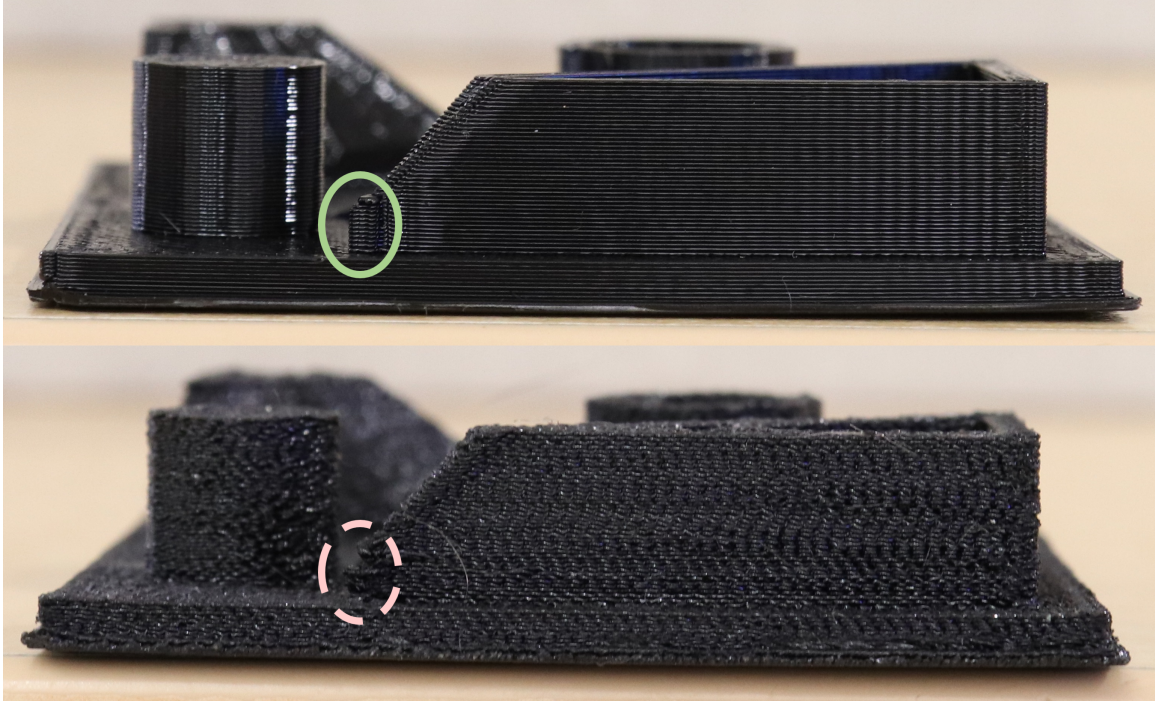


Figure 3.2: Side-view of two AM parts produced by an extrusion process. The top part was generated without vertical base vibration, and the bottom part was produced with it. The roughness values for each were $237.65 \mu\text{in}$ and $946.15 \mu\text{in}$, respectively. The sketches appended to each illustrate the detrimental effects on part surface observed and used to guide the part quality metric selection. “Choppiness” and angularity issues on the highlighted feature were one observed effect.

3.2.2.2 Extended Issues

Although the results discussed above were the primary reasons for selecting part roughness as a measure of AM part quality, this metric likely correlates with other part deficiencies. Things like assembly troubles, dimensional inaccuracies, and wear intolerances are a few that have been explored – primarily for AM with metal materials – in the literature [1, 28, 29]. Although the literature’s material and processes are different from what is considered here, the results are informative to this work. For

instance, it was recently demonstrated that surface roughness was directly related to the fatigue life of powder bed fusion produced metal parts, meaning a rougher surface leads to a shorter fatigue life [29]. This agreement further supports the choice to use part roughness to assess part quality in this study.

3.3 Experiments

This section describes the experimental process shown in Figure 3.3 performed on a MakerBot Method X printer with a dimensional accuracy of 0.2 mm and a composite structure made of steel and aluminum substructures. Several experiments were exercised *before* the refined modal impact test to narrow in on the printer's sensitivities. A refined modal impact test was then performed to identify vibration-sensitive printer components before pursuing the vibration effects experiment. The vibration effects experiment was composed of an extrusion-based 3D printer rigidly mounted to a shake table. The printer was induced with vertical vibration at a single frequency to excite a large energy printer vibration mode. Two sets of parts were printed, and their surface roughnesses were measured: one set with and one set without vertical base vibration. The vibration effects experiment was designed to investigate how base vibration excites a printer's structural modes leading to low AM part quality. A passive isolation scheme was then implemented to demonstrate the experimental approach's final step to mitigate base vibration effects on AM part quality.

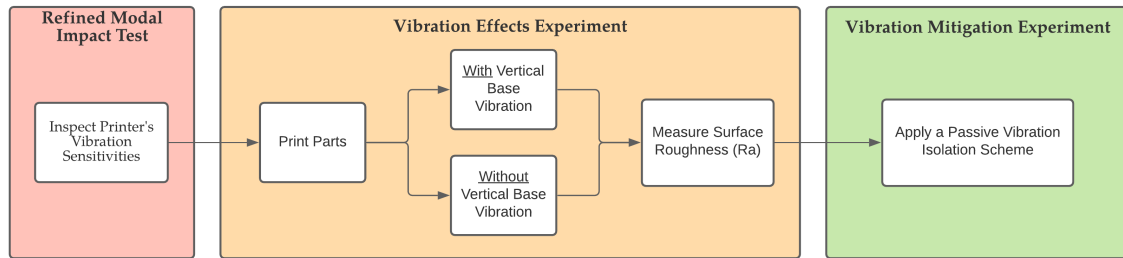


Figure 3.3: Experimental approach. A modal impact test preceded the vibration effects experiment, identifying vibration-sensitive components to target with vertical base vibration. A passive vibration isolation scheme was implemented as an example for vibration mitigation.

3.3.1 Vibration-Sensitive Components

As stated, identifying vibration-sensitive areas on the printer ended with refined modal testing. However, to get to that point, several experiments were performed as described next.

3.3.1.1 Initial Testing

Print Operation Experiment The beginning stages of the vibration testing included a brief disassembly of the printer, specifically its plastic components. Shown in Figure 3.4 are pictures of before and after the disassembly. The main goal for this step was to expose the printer's print heads and frame by removing accessories covering them.

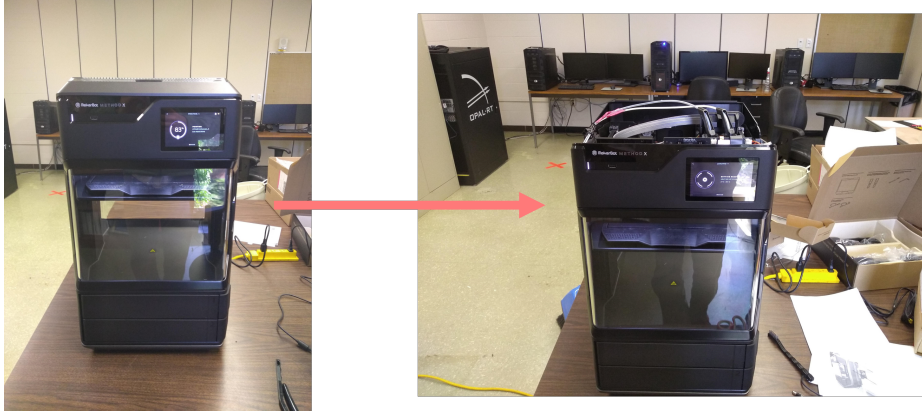


Figure 3.4: Makerbot Method X fully assembled on the left and a slight disassembly of the plastic accessories on the right.

With the printer slightly exposed, the first round of vibration testing involved recording acceleration of the print head while it printed some parts. To do this, accelerometers were placed on the print heads as shown in Figure 3.5. In this figure, two single-axis accelerometer positions are highlighted, one in the negative X-direction and one in a positive Y-direction. These sensors were used to measure the printer's vibration during operation based on the printing pattern shown in Figure 3.6. Figure 3.6 shows an array of printed cylinders at nine locations. The left photo shows the final print, and the right diagram shows the key for each printing position. The purpose of this test was to explore any frequency ranges where the printer had a large vibration response due to the rapid movement of the print heads while printing. An additional motive, emphasized by the nine different locations, was to see if this frequency range varied when the print heads were in different configurations.

Before describing some of the experimental results, please visit the video demonstration of the printer in operation to understand the printing process. The link for the

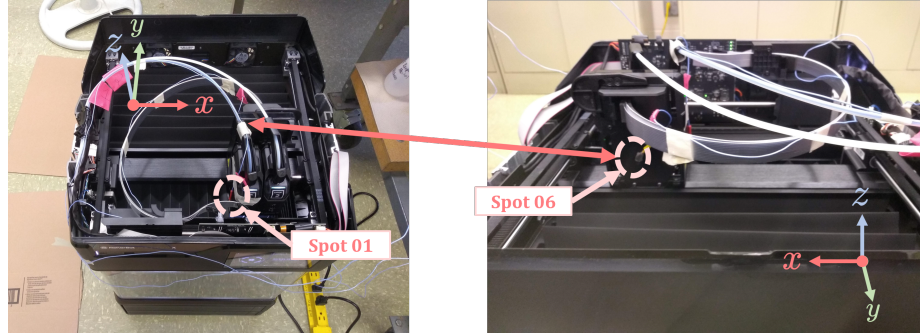


Figure 3.5: Accelerometer placement on the print heads. Two single axis accelerometer positions are highlighted, one in the negative X-direction and one in a positive Y-direction. These sensors were used to measure the printer's vibration during operation based on the printing pattern shown in Figure 3.6

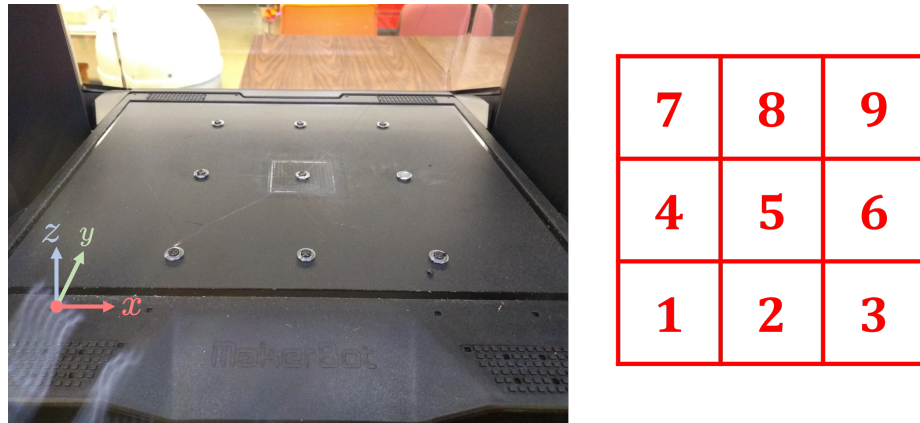


Figure 3.6: Array of parts printed during a vibration experiment. The final parts are the small cylinders shown in the left and the numeric array indicating the spot of each part is shown on the right.

video is shown here: <https://youtu.be/4vz0gf9-Z-4>. Note that the print heads spend about eight seconds printing at each of the nine locations. This time frame was used to record the results presented next.

The measurement procedure for this experiment involved capturing acceleration time histories at each of the nine printed locations for every printed layer. Put another way; this printing process was performed nine different times; each time focused

on recording sensor data at one of the nine locations for every printed layer. The sampling parameters for this experiment are shown in Table 3.1.

The key results of this process are shown in Figure 3.7. This figure shows six of the 18 total plots archived in A.1. The six plots included here are for the positions across the width of the printer's motion as the gantry was in the center. For reference, the key for the nine locations is shown again in Figure 3.7. The six plots displayed correspond to positions four, five, and six.

One thing to note about these results from Figure 3.7 is the low-frequency response. At less than 10 Hz, large values are present in each plot. One explanation for this result is that the data was collected while the print heads had rigid body motion, motion near zero Hz.

Table 3.1

Experiment parameters for the vibration test while printing parts in an array with accelerometers on the print heads.

Parameter	Value	Unit
Frequency Resolution (Δf)	1.46484	Hz
Averages	8	Null
Sampling Frequency (f_s)	12	kHz

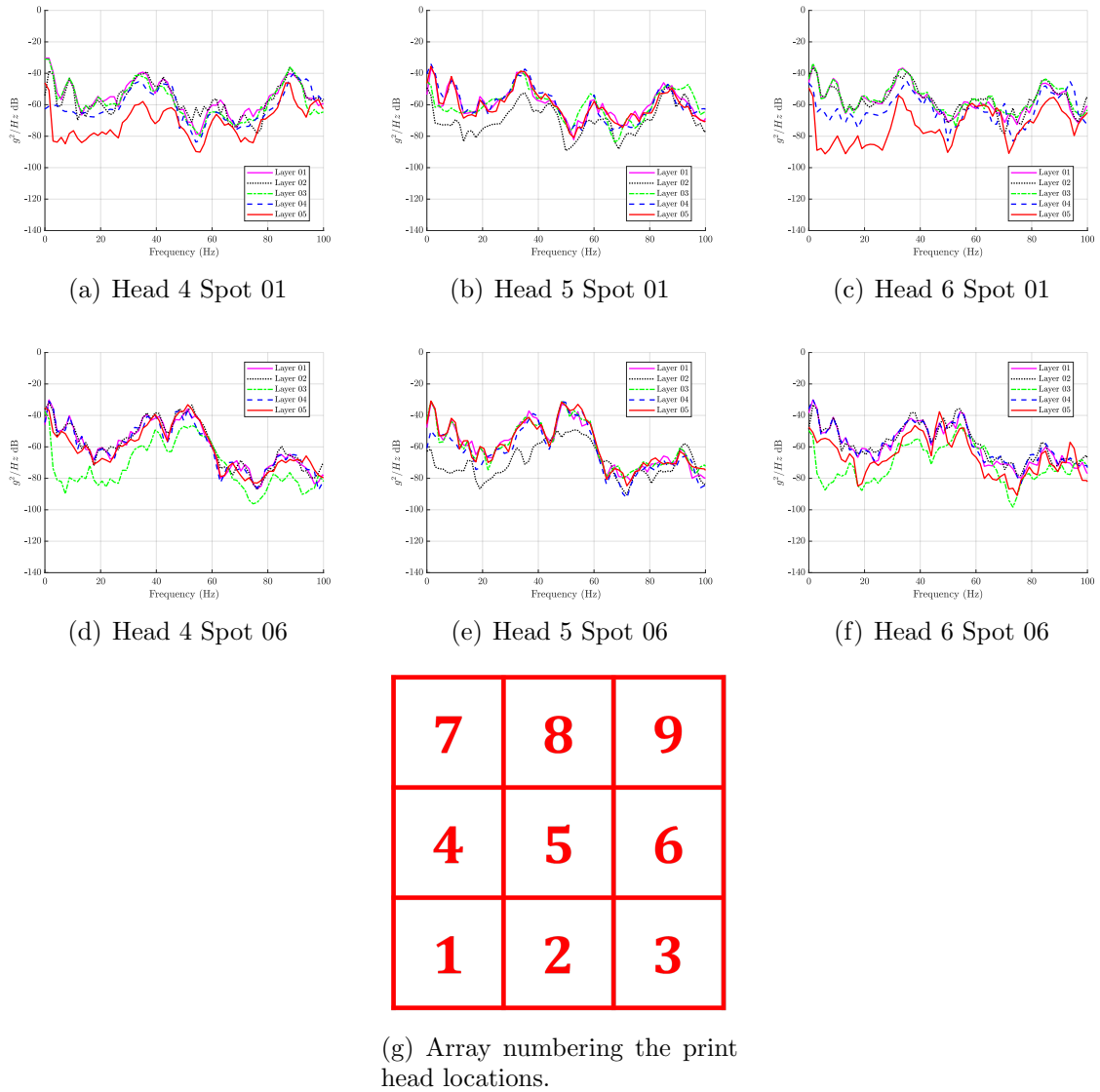


Figure 3.7: Averaged power spectral density functions (PSDs) for the two accelerometer locations in Figure 3.5 and for several print head locations. The array is a key for the print head location for each measurement. Plotted on the top are curves recorded during each material layer. All 18 plots, nine for each sensor location, are archived in A.1.

Horizontal Modal Impact Test The next test performed before the refined modal impact test was a modal impact test that explored the horizontal vibration response of the printer’s main frame. This approach was chosen because it is quick and reliable

for characterizing a structure's vibration response. A load-cell instrumented hammer was used to strike the printer in various locations while sensors measured transient acceleration response. Figure 3.8 illustrates the setup for this experiment. In this figure, six accelerometers were placed on alternating sides of the printer, each set to record acceleration in the positive or negative X-directions. With the accelerometers in place, a small modal impact hammer with a load cell was used to excite the structure and record the load-induced. The corresponding experiment parameters are shown in Table 3.2.

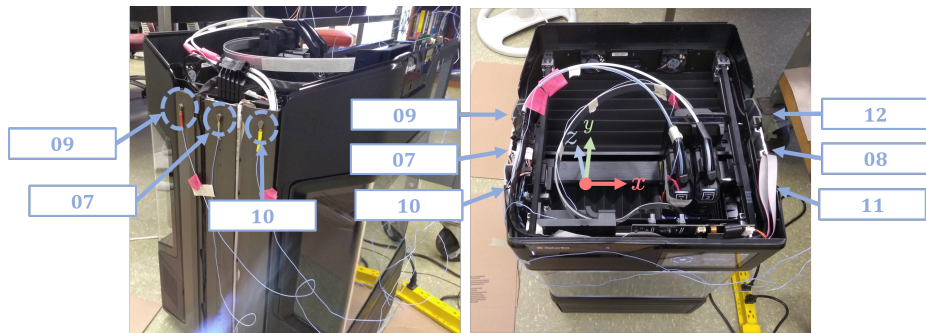


Figure 3.8: Experimental setup for the modal impact test in the horizontal direction. Highlighted are the locations of six single axis accelerometers that were used to record the printer's vibration response in the positive or negative X-directions. These same locations were also impacted with a modal hammer.

Table 3.2

Experiment parameters for the horizontal modal impact test.

Parameter	Value	Unit
Frequency Resolution (Δf)	2.92969	Hz
Averages	5	Null
Sampling Frequency (f_s)	12	kHz
Estimator	H1	Null

The locations of the accelerometers shown in Figure 3.8 were chosen because other

directions from the printer's frame were difficult to measure and excite with the hammer. Figure 3.9 illustrates this point as it shows the tight space on the right frame top.

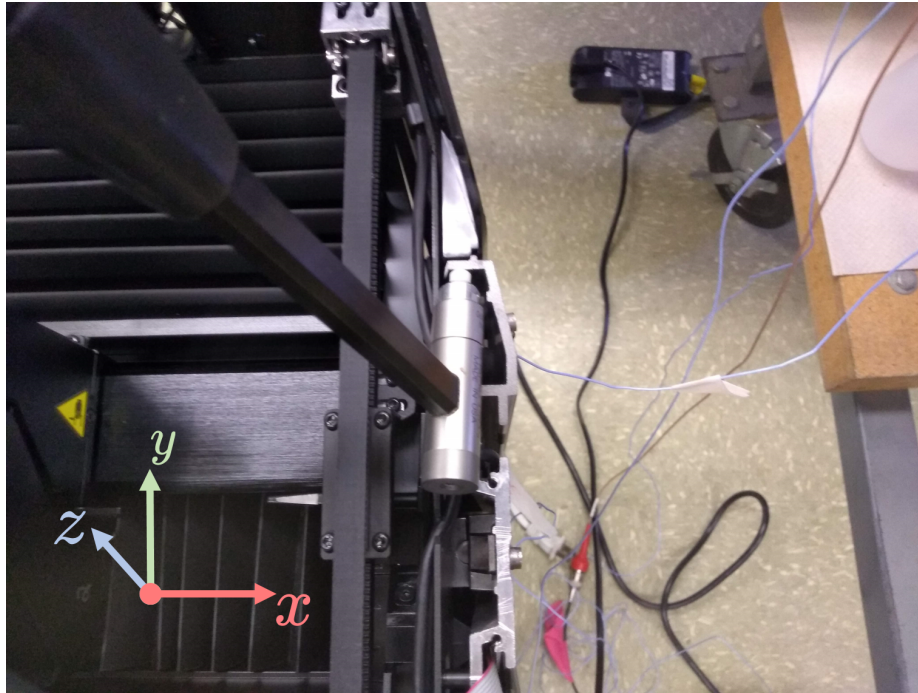


Figure 3.9: Illustration of the limited areas that could be used for measurements and impacts during the horizontal modal impact test. This image shows an impact hammer trying to strike the printer's frame in the Y-direction. However, the area is too tight to get a clear hit.

The experiment results are somewhat incomplete due to data corruption, but some are included in Figure 3.10. Shown here are a few transfer frequency response function estimates (FRFs) in the horizontal X direction between several impacts and response locations. Two things about these results are their high coherence values and the correlation with the previous experimental results in Figure 3.7. Coherence values for all the curves shown in Figure 3.10 are near 1, indicating a high correlation between

the input and output measurements. This high correlation is a valuable fact to consider compared to the previous experiment's results shown in Figure 3.7. In Figure 3.7, the vibration was recorded in the horizontal X-direction with the accelerometer placed on the print head. This previous experiment did not permit measuring the input from the printer's motion and motors vibrating, so there was limited confidence in the results indicated. However, the modal impact results in the horizontal direction in Figure 3.10 can correlate the input to the output. This correlation helps to see that similar peaks from Figure 3.10 at around 10 and 95 Hz are also present in the results from the previous experiment shown in Figure 3.7 for Spot 01.

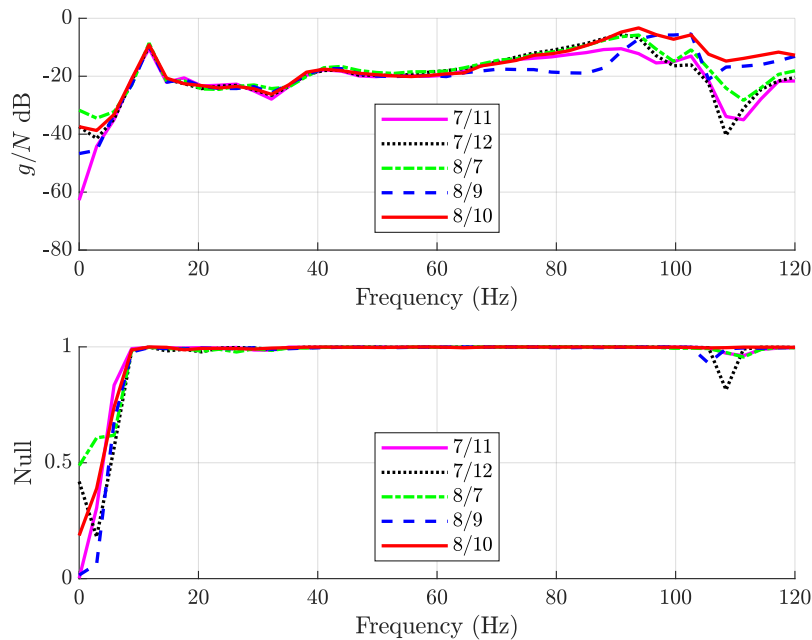


Figure 3.10: Horizontal X-direction frequency response function estimates (FRFs) and coherence from modal impact test. The legend shows the output/input location for each function.

These horizontal modal results represent some of the agreement in the literature that

relative motion between a workpiece and a tool, or in this case, the print heads and the print bed, is a dominant source of vibration that affects a machine's precision [16, 20, 22]. In addition to this agreement, the literature indicates that the direction of a machine's sensitivity depends on the specific machine's design [20, 22]. Although Rivin mentions that "vibration-sensitive machines most frequently have their axes of maximum sensitivity in a horizontal plane" [30], this situation with the MakerBot seemed to be an exception. Due to the horizontal modal results having a smaller magnitude than the vertical ones, which will be discussed in the next section with Figure 3.14 and Figure 3.15, the vertical direction seems more sensitive and therefore critical to the printer's performance. This lack of horizontal sensitivity is supplemented by the fact that the manufacturer advertises this printer as "rigorously tested and ultra-rigid full-body metal frame design eliminates flexing that typically occurs during high-speed print movements" (https://www.youtube.com/watch?v=O4mRZE8S5yY&ab_channel=MakerBot), which likely refers to the manufacturer's pursuit to stiffen the printer horizontally. Although these modal results in the horizontal X-direction indicate a few modes within the 100 Hz frequency range, further modal testing in this direction was not continued due to the vertical Z-direction results described next.

3.3.1.2 Refined Testing

The results from the prior two experiments served as the foundation for the refined modal impact test. The refined test, first introduced in Figure 3.3, is described in this section.

A full-day modal impact test was performed to identify vibration-sensitive components of the MakerBot Method X printer (Figure 3.11), exclusively measured in the vertical direction.

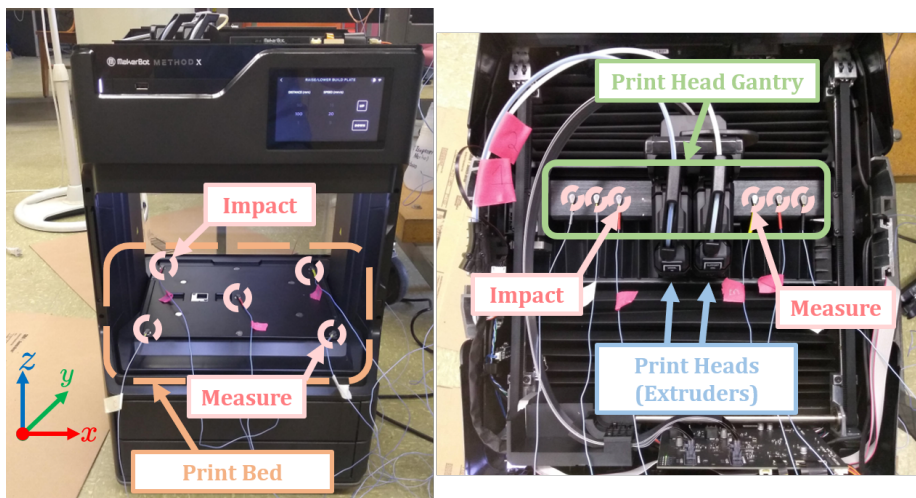


Figure 3.11: Experimental setup for the refined modal impact test that preceded the vibration effects experiment. Accelerometer locations are highlighted on the print bed and print head gantry. Impact and measurement locations are indicated for results discussed in Figure 3.15. The figures represent two asynchronous tests as only six accelerometers were used.

Sensor locations were explored based on parts that may directly affect print quality.

The print bed and print head gantry were candidates as their motion has a primary

role in printing a part's geometry. Other areas were excluded based on testing the vibration response at specific points because they had measurable compliance. Compliance does not lend to clear results through modal analysis, so these areas were not considered further. A few examples are the corner drive mounts for the gantry as they were assembled with the belts' rotation pieces, the X-Z face of the gantry and print heads, and the Y-Z face of the print heads.

Once sensor locations were established, the two testing scenarios in Figure 3.11 were set up: one with impacts and measurements on the print bed as in the left photo, the other tested the print head gantry as in the right photo. This process was repeated at several impact locations with the parameters in Table 3.3 leading to the use of modal analysis to synthesize the results.

Since modal analysis relies on a static configuration of a structure, several configurations were tested to understand how the printer's vibration modes varied with the different print head and print bed positions. The series of configurations for these tests are shown in Figure 3.12. Four configurations were explored, two adjusting the motion of the print heads horizontally on the gantry and two modifying the location of the print bed vertically.

Some results of the process are shown in the form of mode shapes in Figure 3.13 and FRFs in Figure 3.14 and Figure 3.15, while the remainder of the modal results are shown in A.2. Note that these modal analysis results were calculated for one

Table 3.3

Experimental parameters for the refined modal impact test.

Parameter	Value	Unit
Hammer Tip	Soft Rubber	Null
Frequency Resolution (Δf)	2.92969	Hz
Averages	5	Null
Sampling Frequency (f_s)	12	kHz
Estimator	H1	Null

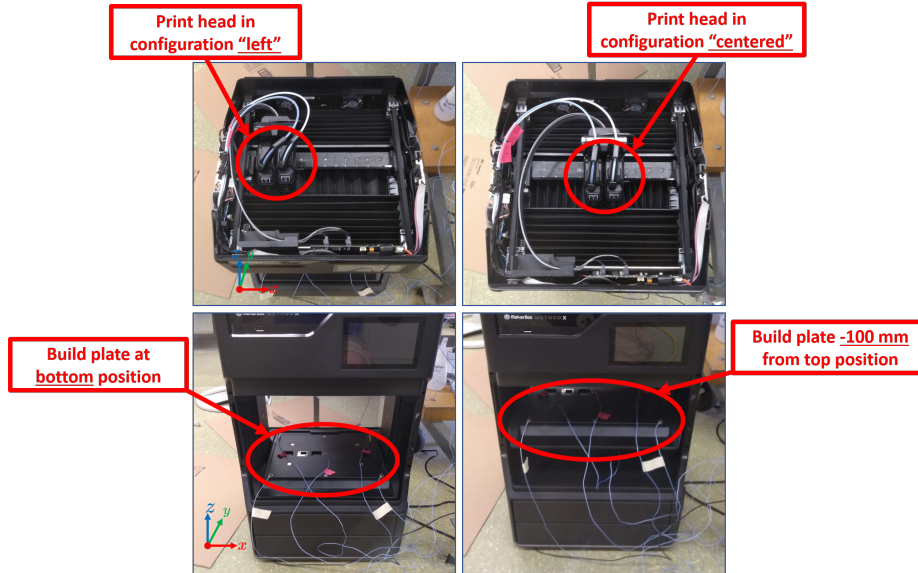
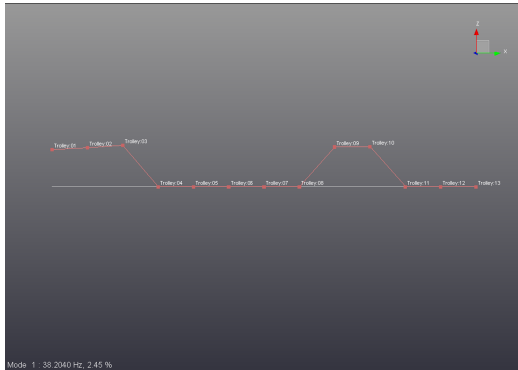


Figure 3.12: Varying printer configurations for the refined modal impact test. The top set and bottom set of photos represent two asynchronous tests as only six accelerometers were used as described in Figure 3.11.

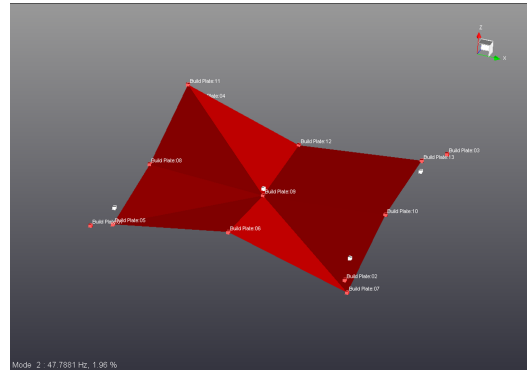
configuration, with the printer in the “centered” bottom configuration as shown in Figure 3.12.

Represented in Figure 3.13, are two large energy modes identified on the gantry and print bed. Although the gantry mode has a strange look because of the lack of vibration data collected at specific nodes, a shape is noticeable as the nodes all pivot about the right end together. The print bed mode shape appears to have a flapping

shape with the largest amplitude response in the upper left corner at node 11.



(a) Gantry/trolley mode shape at ≈ 38 Hz. Mode shapes manifest on the gantry. Note that nodes without motion correspond to areas where data was not collected or was corrupted. The main obstruction was the print heads centered on the gantry.

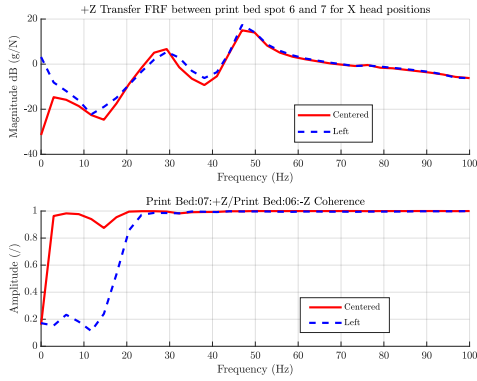


(b) Print bed/build plate mode shape at ≈ 47 Hz.

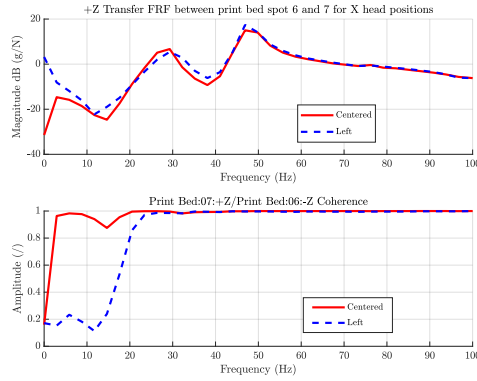
Figure 3.13: Mode shapes of the printer manifest on the gantry and print bed. The modal analysis was performed when the printer was in the “centered” bottom configuration as shown in Figure 3.12.

Figure 3.14 comprises several comparisons of FRFs for the printer in the several configurations from Figure 3.12. All of the curves from the print bed match well for varied print bed and print head positions. The FRFs from the gantry, however, match for different print bed locations but not for different print head locations.

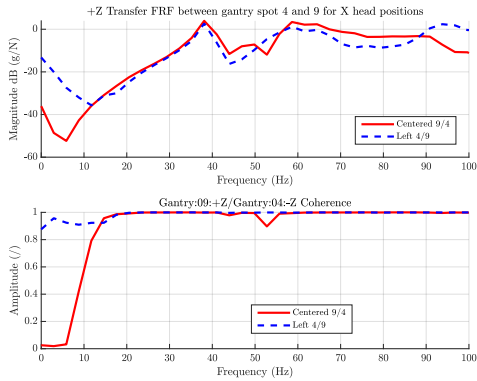
Furthermore, two example FRFs from the tests are shown in Figure 3.15. The print bed’s and print head gantry’s curves were estimated from an impact and measurement shown in the left and right photos in Figure 3.11. The shaded region centers on 40.7 Hz with a 10% bound in both directions. This shaded region indicates the targeted region during the vibration effects experiment for the printer’s resonance to be excited



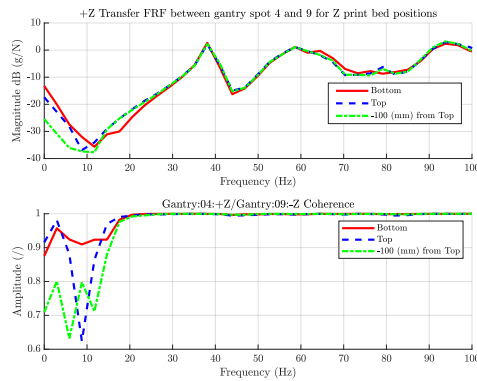
(a) Comparing the response on the print bed for varying print head positions.



(b) Comparing the response on the print bed for varying print bed positions.



(c) Comparing the response on the gantry for varying print head positions.



(d) Comparing the response on the gantry for varying print bed positions.

Figure 3.14: Frequency response function estimates (FRFs) and coherence compared on the print bed and gantry for varying print bed and print head locations. The varying locations are illustrated in Figure 3.12. The plot titles referring to different locations on the gantry and print bed refer to the node names from the shapes in Figure 3.13. An alternate reference for the geometry used to map the test results can be found in Figure A.3 and Figure A.7.

(see Section 3.3.2). The overall observations shown below served as a basis for the vibration effects experiment discussed next.

1. A high-energy resonance manifested at ≈ 40 Hz on the print bed and print head

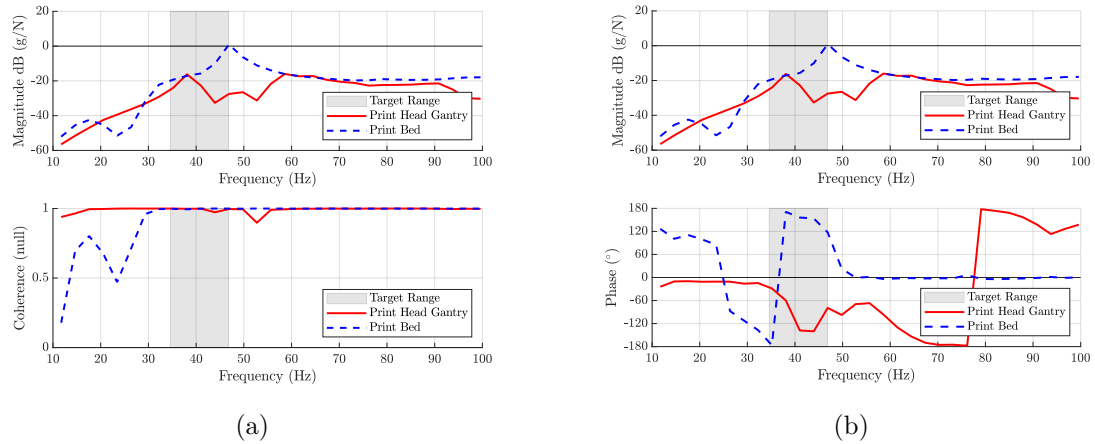


Figure 3.15: Frequency response function estimates (FRFs) in the top left and top right, coherence (left bottom), and phase (right bottom) for the print bed and print head gantry as indicated in Figure 3.11. One FRF from the print head gantry and print bed shows the vibration effects experiment's targeted resonance area. A mode is present on the print head gantry at ≈ 38 Hz, and another is present on the print bed at ≈ 47 Hz. The shaded region centers on 40.7 Hz with a 10% bound in either direction, which was the vibration effects experiment's excitation. Another vibration mode is also present at ≈ 58 Hz on the print head gantry.

gantry. Several other resonances were identified under 100 Hz.

2. The corners of the print bed and center of the gantry were the printer's most flexible features, those with a high amplitude vibration response.
3. The resonant motion of the print bed and print head gantry occurred within a small frequency range, which indicated a possible large relative motion between the two components during production.
4. This test was not exhaustive though it showed that the print bed's local modes did not vary with print bed or print head positions and local modes on the gantry did not vary with print bed position but did with print head position.

3.3.1.3 Shaker Testing Preparation

With the refined modal test completed to understand the printer's vibration-sensitive components according to Figure 3.3, preparation for the Dongling shaker experiment was next. First, the printer was disassembled further by removing plastic accessories then modal shaker tests were performed. The printer's further disassembly was pursued to remove any accessories that exhibited parasitic damping on the printer's underlying structural vibration response. This step was performed with incremental measurements to assure that the printer's response did not change drastically with removing these accessories. The modal shaker tests were performed as a simple bench-testing exploration before mounting the full printer on the large Dongling equipment.

Printer Disassembly Figure 3.16 shows that two key locations for the disassembly process of the printer. Two accelerometers were positioned: one on the gantry and one on the print bed. The printer's vibration response of these two locations were the references for each step of disassembly. The iterative disassembly process is shown in Figure 3.17. The experimental parameters are shown in Table 3.4, and the results of this process are represented in Figure 3.18 and summarized in Figure 3.19.

The main conclusion from these disassembly tests was that the printer could exhibit

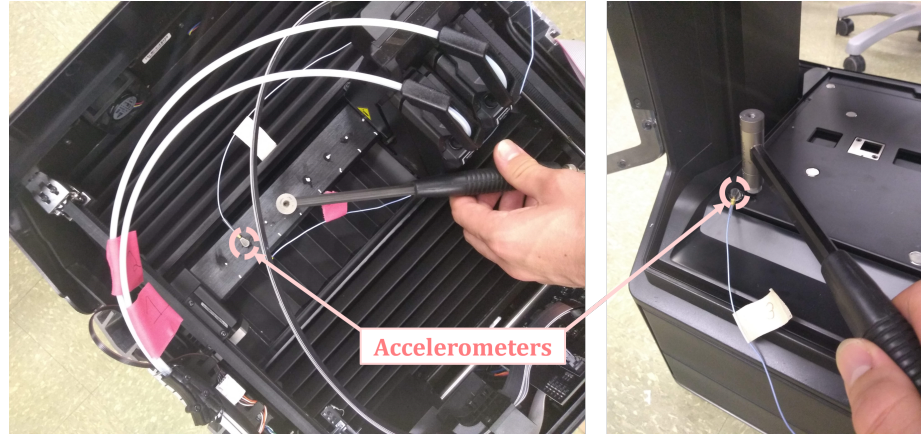


Figure 3.16: Accelerometer locations for the printer disassembly process and tests. The left photo shows the location of the accelerometer on the printer's gantry. The right photo shows the accelerometer position on the printer's print bed.

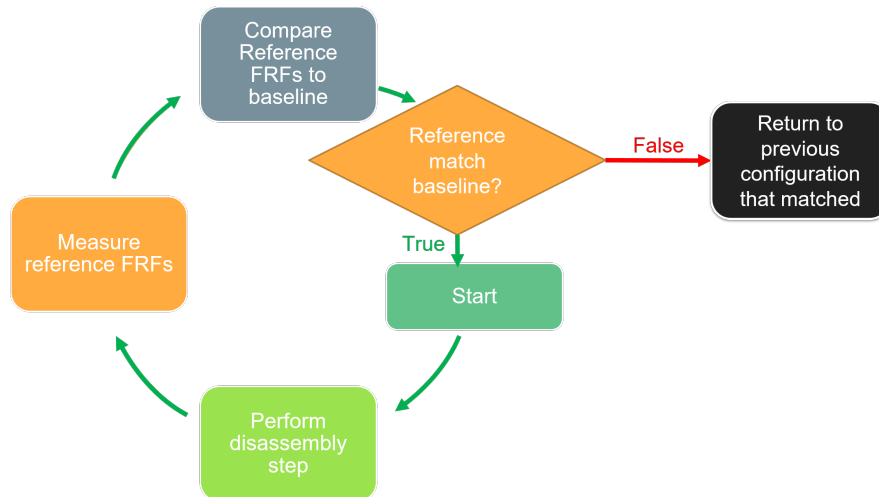


Figure 3.17: The procedure for disassembling the printer's accessories. The iterative process was used to assure that the printer's vibration response did not vary following the removal of plastic components. Once the printer's response changed after a disassembly step, the previous disassembly state was determined as final.

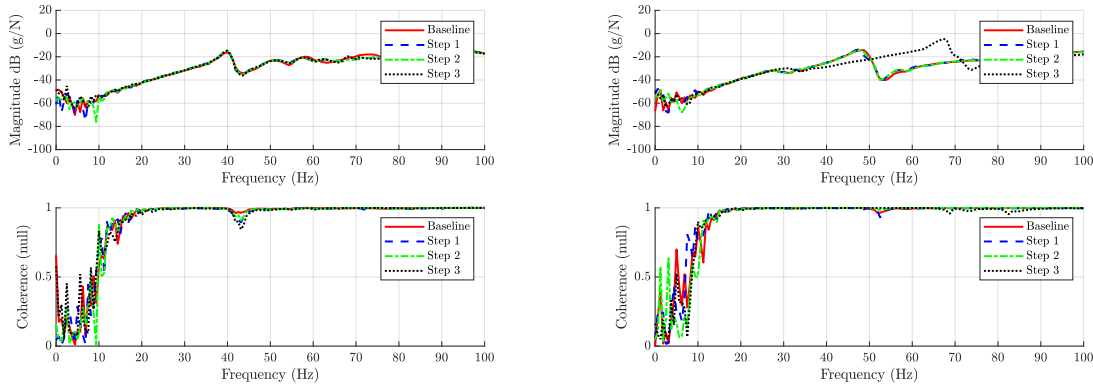
the same dominant vibration characteristics following slight disassembly. This conclusion is evident based on the results shown in Figure 3.18. The frequency response function estimates (FRFs) located on the gantry and print bed are shown in this

Table 3.4

Testing parameters for the printer disassembly tests.

Parameter	Value	Unit
Frequency Resolution (Δf)	0.625	Hz
Averages	5	Null
Sampling Frequency (f_s)	5.12	kHz
Estimator	H1	Null

figure. It is clear from these results is that both the responses on the gantry and the print bed all match up to assembly step 2. After step 2, the response on the print bed changes drastically. This evidence contributed to the understanding that the second disassembly step was final to maintain the same vibration characteristics but with minimal accessories assembled.



(a) Frequency response function estimates (FRFs) on the gantry.

(b) Frequency response function estimates (FRFs) on the print bed.

Figure 3.18: Frequency response function estimates (FRFs) for the printer disassembly test. The left figure are measurements from the gantry. The right figure are measurements from the print bed. Step 2 was deemed as the final disassembly state for the printer, while it maintained a similar vibration response to the baseline data. These measurements were recorded according to Figure 3.16. The gantry response was at point 03 and the impact at point 05 according to Figure A.7. The print bed response was at point 05 and the impact at point 05 according to Figure A.3.

Disassembly Step	Details	Result
Baseline	Door open, rubber coated build plate removed	Reference
Step 1	Removed back plastic panel, unplugged idle fans	MATCH
Step 2 (final)	Removed front door	MATCH
Step 3	Removed print bed flanges	DON'T MATCH

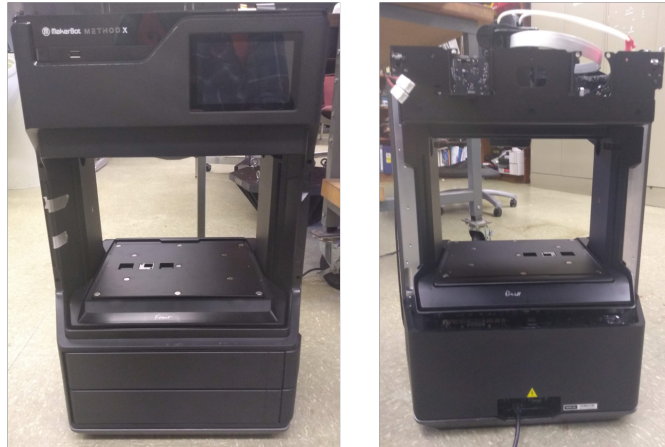


Figure 3.19: A table representing the disassembly step details and two photos showing the final disassembly state of the printer. These photos correspond to the state of the printer after disassembly step 2.

Modal Shaker Tests The modal shaker experiments were performed in three configurations as shown in Figure 3.20. Although each of these configurations was part of the process of the modal shaker tests, Figure 3.21 represents the configuration, from which the following colormap vibration results are shown.

Two tests were performed with the configuration shown in Figure 3.21: a manual frequency sweep between ≈ 25 -50 Hz and a single frequency input at ≈ 40 Hz. Each of these inputs was induced by the modal shaker as shown in Figure 3.21. The complete results from both tests are shown in A.3, but a few results from the sweep test are shown next.

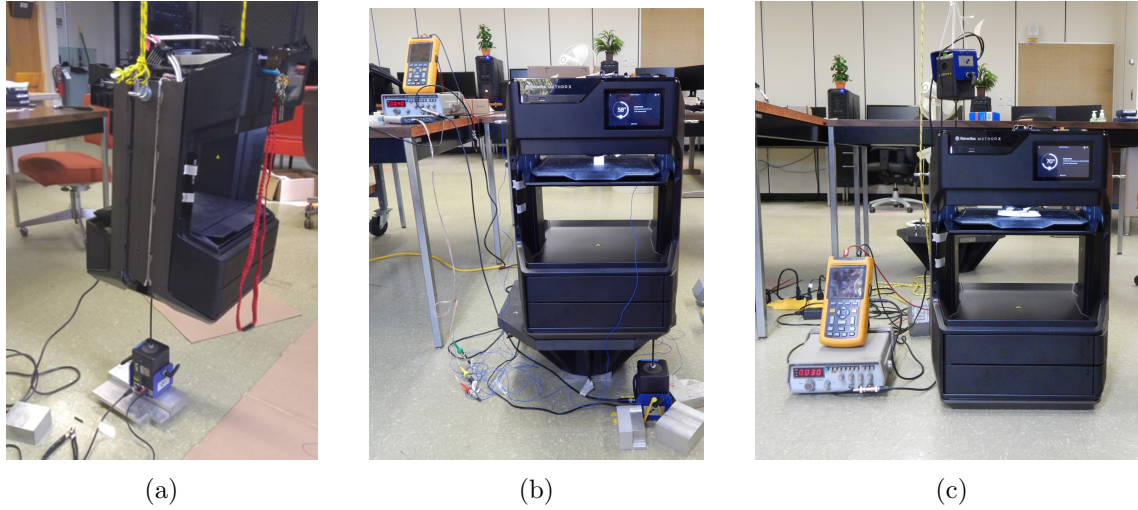


Figure 3.20: Three test setups for modal shaker tests. The left photo has the printer hanging from the ceiling with the shaker exciting the base plate. The middle photo has the printer grounded on a standoff while excited from the bottom by the shaker. The right photo has the printer grounded with the shaker exciting the top left corner of the structure that supports the gantry.

Figure 3.22 displays a few crosspower colormaps from the sweep test acquired with the parameters in Table 3.5. Something interesting about each of the tests is the correlation of peak responses with those identified in the refined impact tests. For instance, the 40 and 47 Hz regions for all these colormaps have commonality with the FRFs from the refined modal impact test. This result was a helpful piece of evidence to inform the Dongling shaker experiments, specifically what frequency ranges to target when trying to induce poor parts. The complete colormap results from these tests are shown in A.3.

Table 3.5
Experiment parameters for the modal shaker tests.

Parameter	Value	Unit
Frequency Resolution (Δf)	1	Hz
Sampling Frequency (f_s)	0.8	kHz

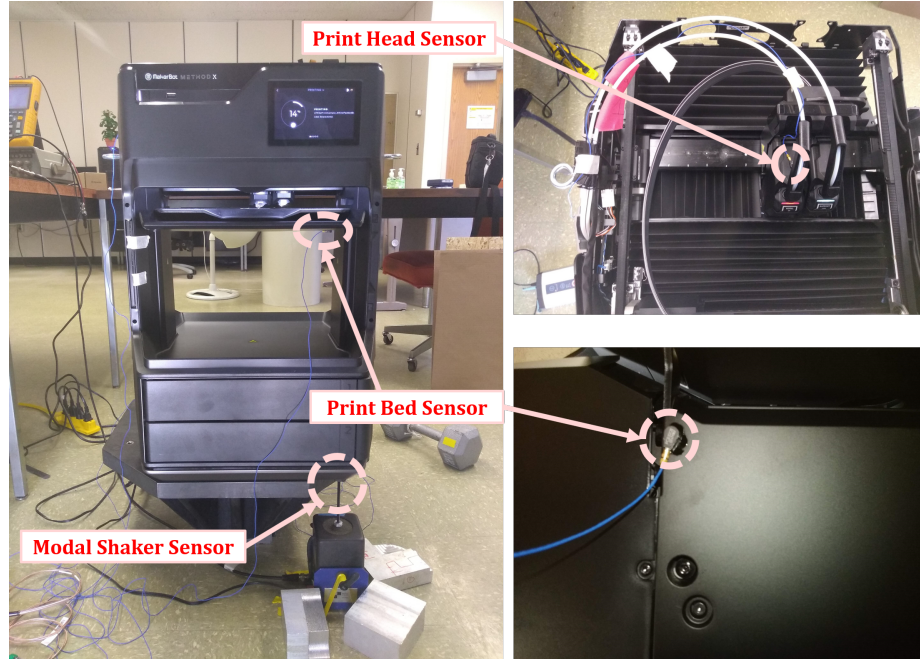
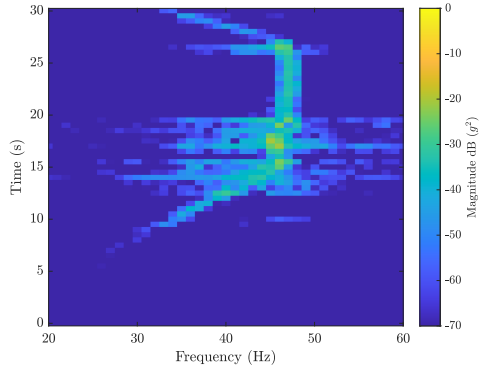
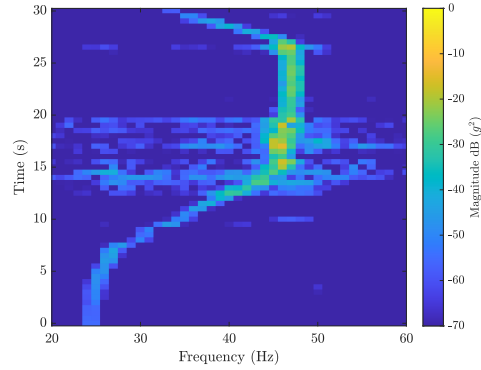


Figure 3.21: One of the three configurations for the modal shaker tests from Figure 3.20(b). The overall setup is shown on the left with arrows pointed at the accelerometers placed during the tests. The top right photo displays an accelerometer placed on top of the primary print head, recording acceleration in the positive Z-direction. The bottom right photo shows an accelerometer placed under the closest right corner, recording acceleration in the negative Z-direction. In addition, but not visible here, an accelerometer was placed by the excitation location of the shaker measuring in the input in the negative Z-direction.

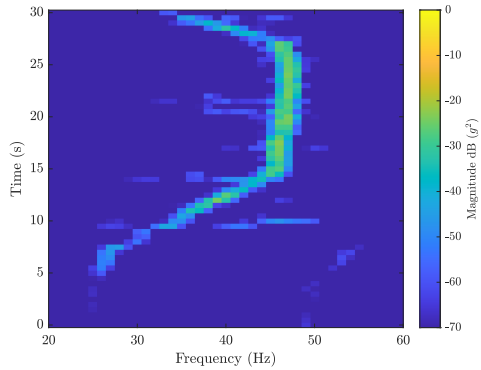
Some printed results of these modal shaker experiments are shown in Figure 3.23. The observable differences between parts printed without and with vibration are primarily regarding part surface roughness, as was described previously.



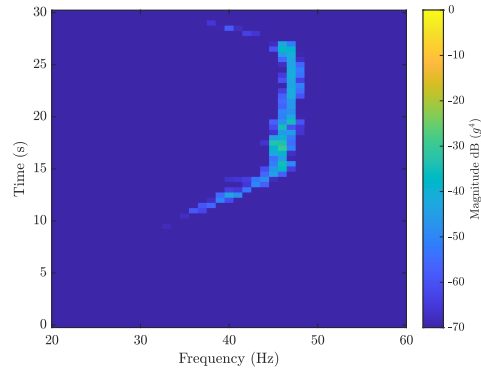
(a) Crosspower colormap of the shaker and print head accelerometer. The complex conjugate of the shaker was premultiplied by the print head; both were linear spectrum acceleration data. Key point(s): 40, 46-47 Hz



(b) Crosspower colormap of the shaker and print bed accelerometer. The complex conjugate of the shaker was premultiplied by the print bed; both were linear spectrum acceleration data. Key point(s): 45-47 Hz

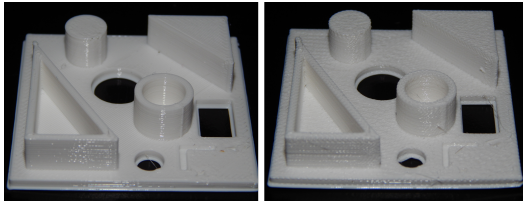


(c) Crosspower colormap of the print head and print bed accelerometer. The complex conjugate of the print head was premultiplied by the print bed; both were linear spectrum acceleration data. Key point(s): 40, 46-47 Hz

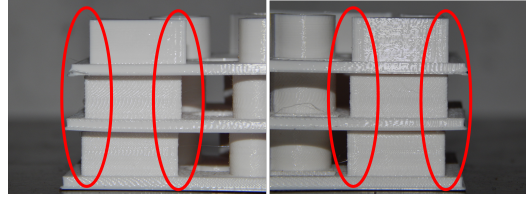


(d) Crosspower colormap of the shaker and print head/print bed crosspower from Figure 3.22(c) accelerometer. The complex conjugate of the shaker was premultiplied by the print head/print bed crosspower from Figure 3.22(c); both were linear spectrum acceleration data. Key point(s): 45-47 Hz

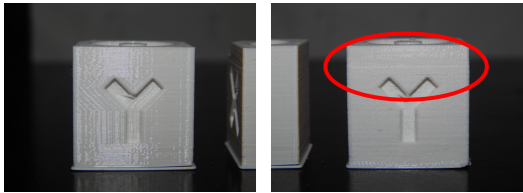
Figure 3.22: Crosspower colormap recordings during a manual sine sweep from ≈ 25 -50 Hz corresponding to Figure 3.21.



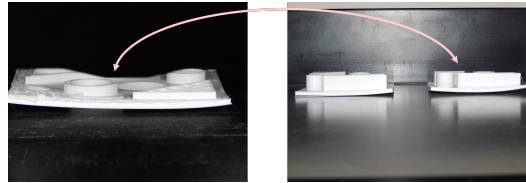
(a) Top-view of two 3D printed parts. The left was printed with no modal shaker vibration present. The right was printed with the test configuration in Figure 3.20(c) using a sine input at 30 Hz at an amplitude of 0.32 g.



(b) Side-views of three 3D printed parts. The top part was printed with no modal shaker vibration present. The middle part was with the test configuration in Figure 3.20(c), using a sine input at 30 Hz at an amplitude of 0.32 g. The bottom part was printed with the test configuration in Figure 3.20(b) with a sine input at 40 Hz with an amplitude of 0.05 g. Highlighted by the circles is layer separation for parts printed with modal shaker vibration, which was not present for the top part printed without vibration.



(c) Side-view of two 3D printed parts. The left was printed with no modal shaker vibration present. The right was printed with the test configuration in Figure 3.20(b) using a sine input at 40 Hz at an amplitude of 0.05 g. Highlighted by the circle is a layering difference for the part printed with modal shaker vibration, which was not present for the left part printed without vibration. Notice that the area circled has a line separating the two areas of printed layers. This line represents the moment when the modal shaker was shutoff. Meaning, below the line are layers printed with vibration, and above the line is printed with not vibration.



(d) Two photos representing catastrophic failure of a part printed with vibration. The isolated part on the left corresponds to the right part in the right photo, which was printed with the test configuration in Figure 3.20(c) using a sine input at 30 Hz at an amplitude of 0.32 g. The left photo was taken while the printer was in operation. Notice the melt areas on the left of the part. This was where the heated print head tip ran into the curled part. The right photo shows a part printed without vibration (left) and with vibration (right). Notice the amplified curling for the part on the right when the shaker vibration was induced.

Figure 3.23: Printed part results from the modal shaker tests.

3.3.1.4 Summary

To summarize this subsection, three stages of testing were performed to identify vibration-sensitive components on the MakerBot Method X printer. The initial testing comprised two steps: an experiment with sensors on the print heads while the printer manufactured nine parts in an array and a modal impact test in the horizontal X-direction. These tests helped refine the testing procedure, which led to a refined modal impact test measuring vibration in the vertical Z-direction. The refined modal impact test was performed on both the gantry and the print bed. Then, in preparation for the Dongling shaker tests in the following discussion, the printer was exposed to two more sets of tests: a set of disassembly tests and modal shaker tests.

3.3.2 Setup

Following the flow of Figure 3.3, the next step in the experimental process was the vibration effects experiment. This section contains the setup, results, and discussion for experiments performed on the Dongling shaker. Throughout the section, many key results will be given and discussed with various pointers given to Appendix B where all of the results from these tests are stored.

3.3.2.1 Hardware Arrangement

The vibration effects experiment setup (Figure 3.24) included the MakerBot Method X and an ES-10D-240 Dongling shaker. The software Vibration Research VibrationVIEW version 10 commanded the shaker. Two custom mounting plates – spaced with aluminum inserts – united the printer base’s and the shake table head expander’s (the device that extends the shaking platform) unique interfaces. Two deployed PCB[®] accelerometers recorded vibration intensity, a 352A24 under the print bed center (origin of the parts built) and a 352C22 on the top of the primary print head. Each channel recorded data while the stepper motor belt driven gantry (with X-Y motion) and stepper motor leadscrew driven print bed (with Z motion) moved during production (see Figure 3.27(c) for further details). A Simcenter SCADAS XS served as the data acquisition (DAQ) system, configured with Simcenter Testlab 2019.1. Vibration came from two sources: the machine’s vibration and the vertical shaker. The machine’s vibration was excited by rapid print head motion with the printer set to a max print head travel speed of $500 \frac{mm}{s}$. The vertical excitation was set to a peak amplitude between 0.0325 and 0.13 g. A series of tests were performed between these amplitudes. Discrete setpoints were used with a frequency of 40.7 Hz for the entire print-time. The intent was to target the print bed and head’s relative vertical motion, which dominates the printer’s vibration response at ≈ 40 Hz. The input levels were

chosen based on them being below the threshold of where the printer would be damaged by resonance yet high enough to excite the printer noticeably. Data collection occurred with a frequency resolution (Δf) of 0.2 Hz and a sampling frequency (f_s) of 2560 Hz. Both DAQ channels were windowed with a flattop function.

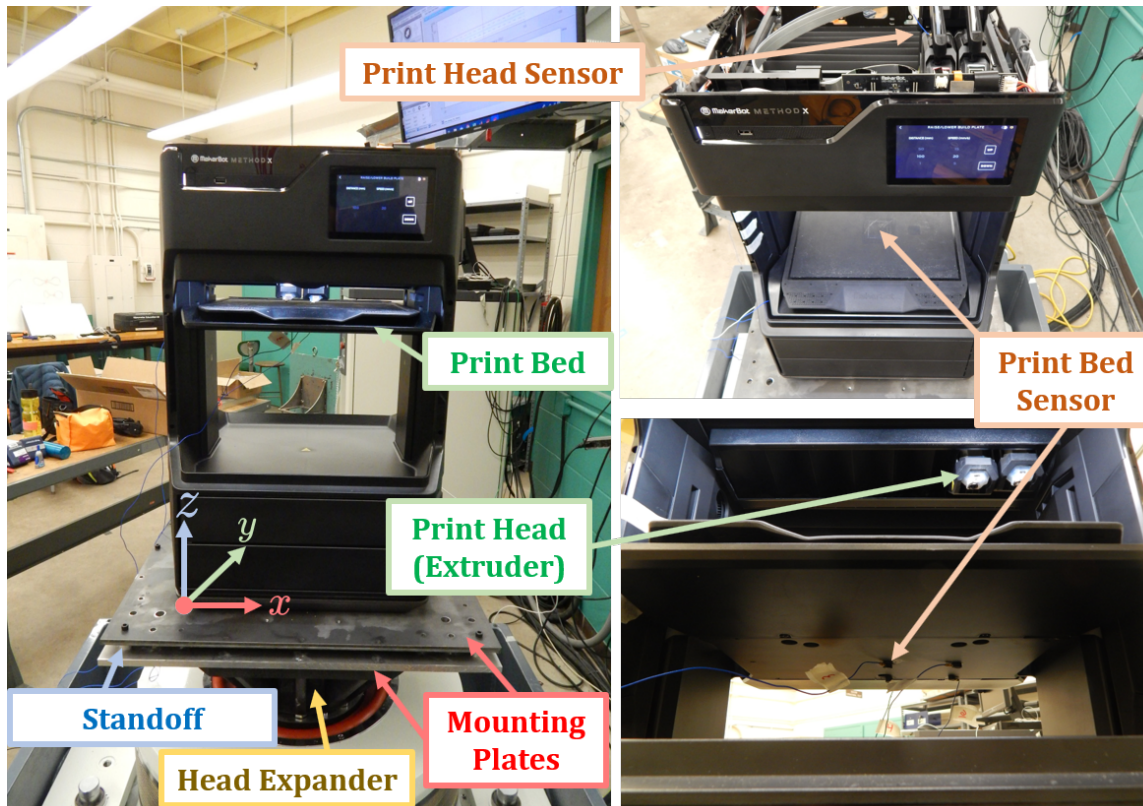


Figure 3.24: Experimental setup of the MakerBot Method X printer rigidly mounted to an ES-10D-240 Dongling shaker. Two mounting plates, separated by aluminum standoffs, provide a mating interface for the printer base and the Dongling head expander/spacer. Two accelerometers/sensors were positioned to measure the vibration of the printer: on top of the primary print head (administers X-Y motion with stepper motors driving the belt-fed gantry) and underneath the center of the print bed (provides Z motion via a leadscrew driven by a stepper motor) where a part would be built.

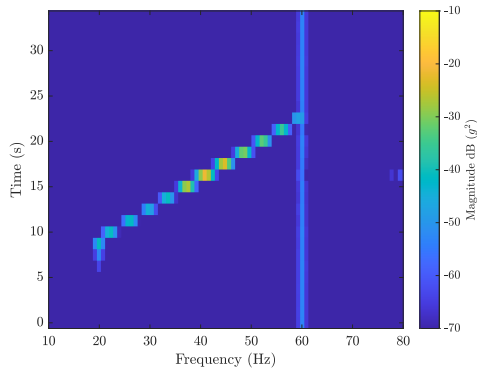
A sweep test was performed with measurements recorded like with the modal shaker to confirm the target frequency range with new boundary conditions on the Dongling

setup. The parameters used for this test are shown in Table 3.6 and some of the results are in Figure 3.25. Figure 3.25 represents a series of colormaps similar to what was introduced regarding the modal shaker tests in Section 3.3.1.3. One thing to notice about these results is regarding Figure 3.25(d). This figure is a result of three signals in a composite crosspower. Physically, it is abstract, with the units being g^4 . However, intuitively, this result represents how the relative vertical motion of the print head and print head gantry correlate with the input from the shaker. And, as it can be observed, Figure 3.25(d) has a high amplitude region around 40 Hz. This result was slightly different than what was observed with the preliminary modal testing in Section 3.3.1.3, so it clarified the decision to target ≈ 40 Hz for the vibration effects experiment. The complete colormap results from these tests are shown in B.1.

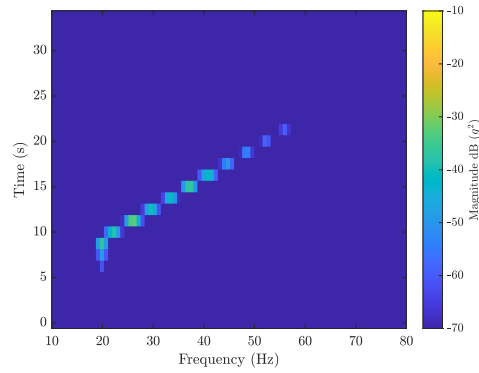
Table 3.6

Experiment parameters for a sweep test on the Dongling shaker to check the new boundary conditions.

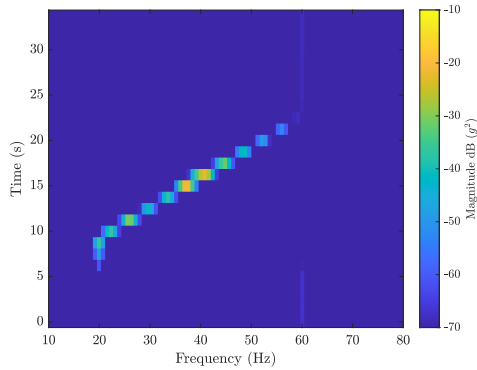
Parameter	Value	Unit
Frequency Resolution (Δf)	0.8	Hz
Sampling Frequency (f_s)	2.56	kHz



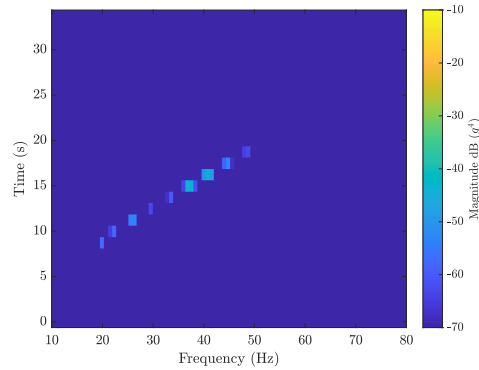
(a) Crosspower colormap of the shaker and print head accelerometer. The complex conjugate of the shaker was premultiplied by the print head; both were linear spectrum acceleration data.



(b) Crosspower colormap of the shaker and print bed accelerometer. The complex conjugate of the shaker was premultiplied by the print bed; both were linear spectrum acceleration data.



(c) Crosspower colormap of the print head and print bed accelerometer. The complex conjugate of the print head was premultiplied by the print bed; both were linear spectrum acceleration data.



(d) Crosspower colormap of the shaker and print head/print bed crosspower from Figure 3.25(c) accelerometer. The complex conjugate of the shaker was premultiplied by the print head/print bed crosspower from Figure 3.25(c); both were linear spectrum acceleration data.

Figure 3.25: Crosspower colormap recordings during a sine sweep from \approx 20-60 Hz corresponding to Figure 3.24.

3.3.2.2 Part Production Procedure

Two sets of parts were printed with (qty: 10) and without vibration (qty: 33) based on the geometry in Figure 3.26. These part features were not chosen based on any standard for evaluating AM products as many AM standards are being developed [1]. Instead, the features were designed based on discussions with the research sponsors as they contained several primitive features typical for 3D printed parts. Cylinders, cutouts, chamfers, and varying angle edges were included to represent typical features of 3D parts that could indicate how various geometries would be affected by vibration. The chamfers were specifically chosen because of the preliminary observations of vibration effects as these features exposed the layer separation described in Section 3.2.2.1.

Parts printed with vertical base vibration were excited with amplitude inputs between 0.0325 and 0.13 g. Since the analysis described later in Section 3.3.3 is based on relative comparisons between parts printed with the same printing parameters, the parameters are not provided here. A Mitutoyo SJ-210, featuring a range of 14200 μin and an error of 0.8 μin was used to measure part roughness. All parts were subjected to a roughness measurement encircled in Figure 3.26 following production. The dissimilar sample sizes of printed parts were due to needing an observer present for the entire ≈ 1 hr production during the vibration tests, but not for tests without

vibration. Regardless, both sample sizes were still large enough to explain the key observations in the next section.

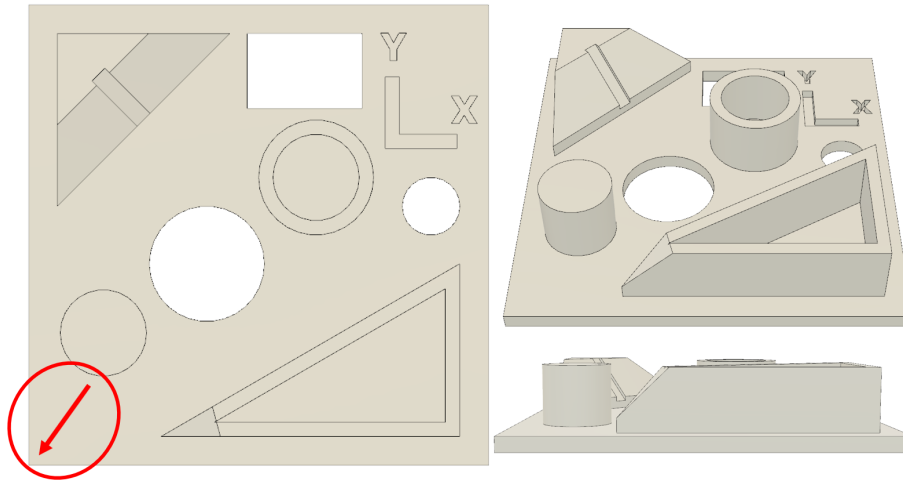


Figure 3.26: Geometry of parts produced during vibration experiments. The part's base is approximately 2" x 2". The circled area and arrow is the area and the direction the surface roughness measurements were acquired using a Mitutoyo SJ-210 profilometer. This measurement location was used because it was one of the few areas that permitted enough space for the profilometer tool to perform a full measurement stroke.

3.3.3 Results and Discussion

3.3.3.1 Printer Response from Base Vibration and Machine Vibration

Considering the experimental results center on how base vibration affects part quality, it is appropriate to identify the dominant vibration source present during production. Figure 3.28 represents base vibration and machine vibration to illustrate this point.

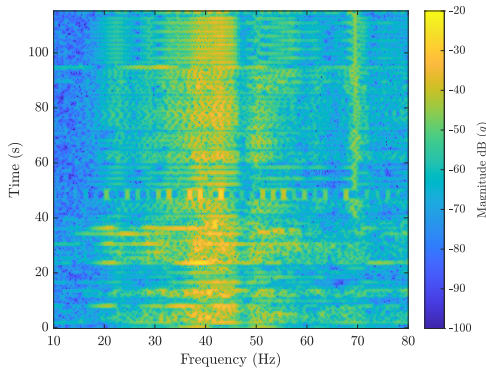
However, before addressing the main results in Figure 3.28, an explanation is needed to clarify where these results originated. The results for this test comparing vibration sources were acquired with the parameters in Table 3.7. The acceleration data was acquired from each sensor as described in Figure 3.24 and as illustrated in Figure 3.27(c). Figure 3.27(c) is provided as a simple illustration for the acquisition setup. The accelerometers are marked with solid red dots, and the dashed yellow line indicates the relative motion. The relative motion of print bed and print head gantry was acquired by subtracting the time-histories via a virtual channel in the Testlab software. Following some fast-Fourier transforms (FFTs), the colormap results in Figure 3.27 were calculated.

Table 3.7

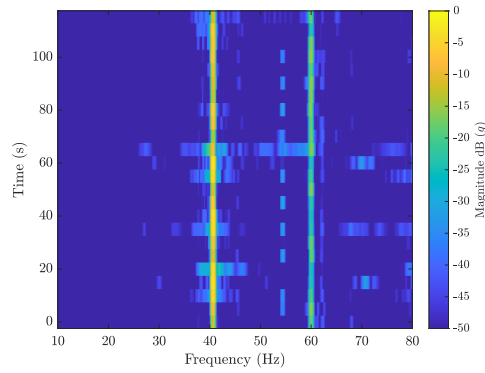
Experiment parameters for a test on the Dongling shaker to compare the sources of vibration.

Parameter	Value	Unit
Frequency Resolution (Δf)	0.2	Hz
Sampling Frequency (f_s)	2.56	kHz

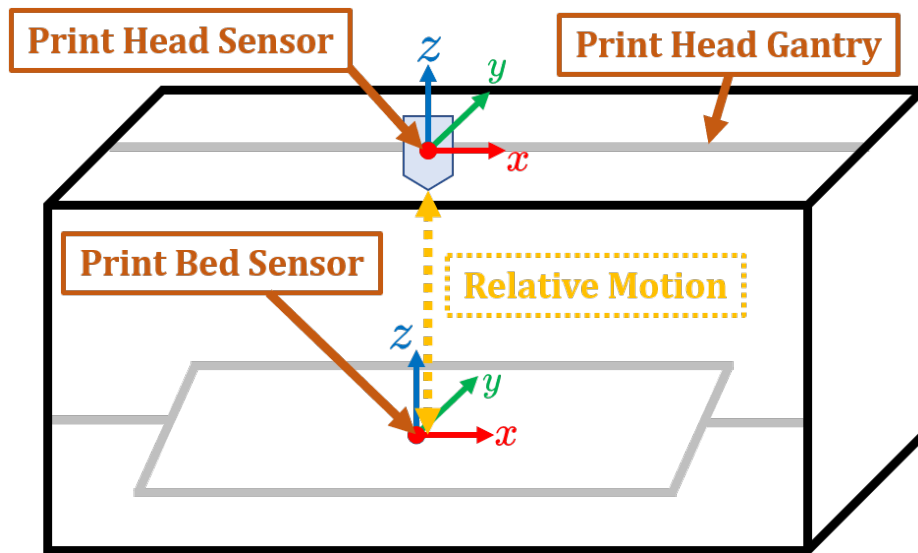
Now onto the main results, the curves in Figure 3.28 are calculations of the maximum relative motion between the accelerometers exposed in Figure 3.24 and Figure 3.27(c). They illustrate how the part on the print bed moved relative to the print head extruder during one production layer. Data was recorded for one production layer, and the maximum amplitude frequency response dataset was extracted for Figure 3.28. The curve for without vibration in Figure 3.28 was extracted from Figure 3.27(a) at 24 seconds and the curve for with vibration in Figure 3.28 was extracted from Figure



(a) Relative motion without vertical base vibration.



(b) Relative motion with vertical base vibration.



(c) MakerBot Method X printer sketch of motion components targeted in an experiment. The print bed enables Z-direction motion and X-Y motion is permitted by the print head gantry. The coordinate frames present on the print bed and print head indicate where two accelerometers were positioned for measuring and calculating relative motion between them.

Figure 3.27: Diagram and data representing the relative motion between the print head and print bed for two scenarios: with and without vertical base vibration. Rapid motion from the print head travel set to a maximum of $500 \frac{mm}{s}$ for inducing machine vibration in each case. Relative motion was measured between the print head and print bed accelerometers (see Figure 3.24). The base vibration scenario was excited by a 0.1 g sinusoid at 40.7 Hz for the entire production. The plots show the results for approximately one extruded material layer.

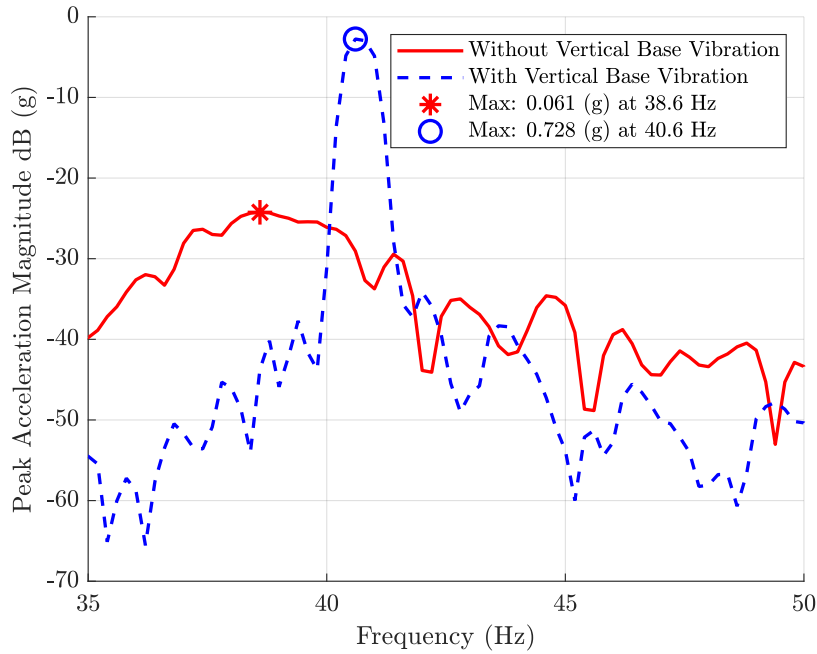


Figure 3.28: Relative motion measured between the print head and print bed accelerometers (see Figure 3.24). The base vibration scenario was excited by a 0.1 g sinusoid at 40.7 Hz for the entire production. The curves are maximum values for data recorded while the printer applied one extruded material layer. Notice the peak of each curve is near the large energy resonance that was identified in the refined modal impact test. In addition, the maximum value for the base vibration case is over 10× larger than without base vibration. Rapid motion from the print heads set to a maximum travel speed of 500 $\frac{mm}{s}$ induced machine vibration in each case.

3.27(b) at 60 seconds. This approach sought to avoid difficulties acquiring data at an exact interval of the production cycle for each test case, as it focused on the overall peak motion during a printed layer rather than a subpeak at a specific interval. The print bed and head's relative vertical motion was targeted with a vertical sinusoidal excitation set to an amplitude of 0.1 g at 40.7 Hz. It was expected for both curves to have a peak at the ≈ 40 Hz resonance; however, the response with base vibration was larger.

The curves in Figure 3.28 were extracted from a test with and without vertical base vibration. Machine vibration was present in both cases as the print head travel speed was set to a maximum of $500 \frac{mm}{s}$ to excite the printer's modes. However, Figure 3.28 indicates that machine vibration is $10\times$ less significant of a vibration source than vertical base vibration. The comparison is not a *like-to-like* comparison as the vertical base vibration is trying to excite a resonance with vertical components. In contrast, the machine vibration relies on horizontal to vertical coupling to excite the same resonance. A few other things that could have attributed to the curves' differences are the print head mass and the printer structure's stiffness and damping in the vertical and horizontal planes. The mass of the MakerBot printer is 29.5 kg, and the total mass of the print heads is 0.64 kg, which is a small fraction of the total printer mass at slightly over 2%. Therefore, when the print head makes rapid movements, only a small force is exerted, resulting in a low amplitude for the machine vibration source. The printer's rapid motion directly moved the horizontal components of the printer. So, if these components were stiffer or damped the response more, then the printer's overall response would be less in the 40 Hz region targeted. A similar explanation arises when considering that the horizontal resonances may have been entirely decoupled from the identified vertical resonance, based on the manufacturer's design (see Section 3.3.1.1), resulting in low amplitude response from the machine vibration compared to the base vibration. Extended work on this topic may include further testing of horizontal and vertical resonance effects from machine vibration and vertical and horizontal base

vibration. Although this result has a condition that makes the comparison less than ideal, it fits the common understanding present in the literature that base vibration often dominates machine vibration for precision machines [16, 20, 22].

3.3.3.2 Part Roughness With and Without Base Vibration

Part roughness was chosen to quantify base vibration effects on AM part quality. The collection of measurements is displayed in Figure 3.29, with part count and roughness values shown for each test case. First, notice the similar shape and skewness of the base vibration (10 parts) and no base vibration (33 parts) cases with values of 0.33 and 0.54, respectively. Though the base vibration data set had over twice the samples due to the extended production time described in Section 3.3.2.2, both data sets share a mutual distribution. Parts subject to base vibration have a median that is two times larger than those printed without base vibration. Regarding the spread, the standard deviation of parts with vibration is nearly double that of parts without vibration, with values of 349.01 μin and 187.71 μin , respectively. Although part photos are not provided here, several fascinating photos can be found in B.4.

These results (Figure 3.29) suggest that part quality is affected by base vibration – quantified with surface roughness – for two reasons. Low-quality parts are more likely when base vibration is present, and part quality is less predictable under the same conditions. The minimal sample sizes hinder the statistical basis for analyses, but

both distributions' mutual shape suggests that the samples collected were sufficient for the analysis presented here. Further work for this approach may include larger sample sizes to strengthen the statistical basis for analysis.

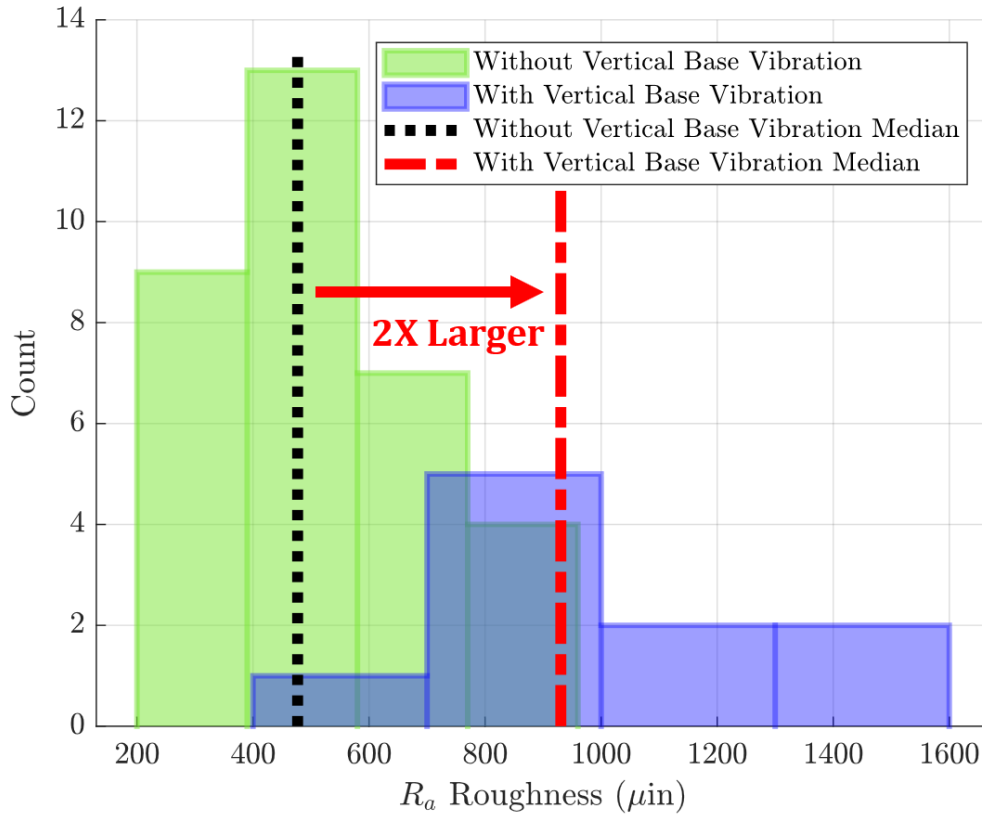


Figure 3.29: Histogram of part roughness measurements R_a collected for parts printed with (qty: 10) and without base vibration (qty: 33). Parts printed with vertical base vibration had amplitude inputs between 0.0325 and 0.13 g. Different sample sizes were due to the long print time for the base vibration test that required an observer. Bin values are counts for a range of roughness values. Included are the median values for each sample set. Both data sets have a similar skewness. However, the median of parts printed with base vibration is two times higher than those printed without base vibration. Meaning, parts are expected to be of lower quality when printed amidst base vibration. Lastly, the spread of the parts printed with base vibration (Std Dev: 349.01 μin) is nearly double that of the parts without base vibration (Std Dev: 187.71 μin). This comparison indicates that part quality is also less predictable when vertical base vibration is present.

3.3.3.3 A Path for Other Printers in Harsh Environments

A passive isolation scheme was implemented as a demonstration of the prescribed experimental approach (Figure 3.3). Three Inglasco sponge rubber hockey pucks (<https://www.icewarehouse.com/Inglasco/descpage-SPGP.html>) replaced the standoffs shown in Figure 3.24 and acted as isolators to decouple the vertical base vibration from the printer's structural vibration. The same experimental setup in Section 3.3.2 and Section 3.3.2.2 were used to print parts with vertical base vibration and with or without passive isolation. Minimal work was done to tune the passive isolation design. However, results for some simple tuning are in B.2. Actual design work should reduce the vibration and improve the part quality more.

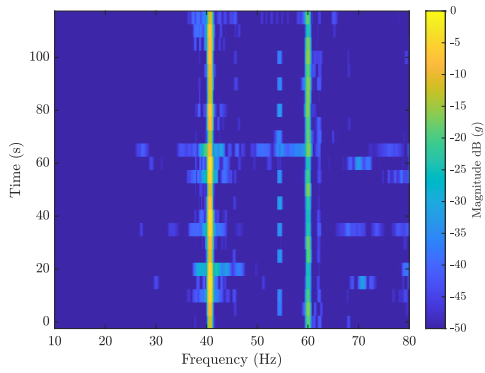
Before presenting and discussing the results of this demonstration, please visit the following videos to illustrate how the vibration was reduced on the print heads. A video where the printer has no isolation is shown here https://youtu.be/1fzCmz0Bd_4. A video where the printer has passive isolation is shown here <https://youtu.be/XtFirRXzL10>.

Figure 3.30 demonstrates how passive isolation effectively minimized the relative vertical motion of the print bed and print head. Similarly, as was described in Section 3.3.3.1, colormaps were recorded, and the maximum value slices were extracted. Two curves are plotted, contrasted with one from a test without passive isolation and the

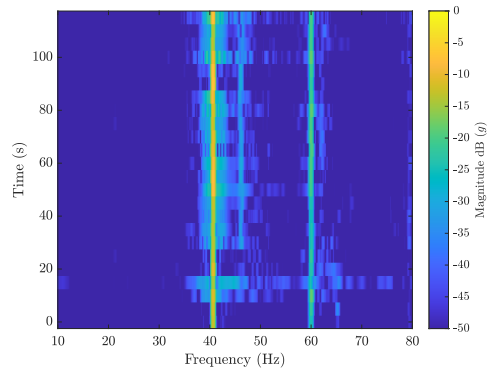
other with it. The vertical base vibration was set to 0.1 g at 40.7 Hz for both to target the same resonances described previously. The curve for without isolation in Figure 3.30(c) was extracted from Figure 3.30(a) at 60 seconds and the curve for with isolation in Figure 3.30(c) was extracted from Figure 3.30(b) at 90 seconds.

Two considerations based on the annotations in Figure 3.30 are the new mode at 46 Hz and the reduced peak amplitude at 40.7 Hz. The new mode was an expected artifact of passive isolation as the scheme introduces another subsystem mode to form an aggregate system. Although the new mode is a side effect, it is minor to the dominant frequency range of the printer response as it is 22 times lower than the peak at 40.7 Hz. Future work may include refining the isolation setup to push the new mode to a higher frequency and damp it more. The peak reduction at 40.7 Hz is an effect of decoupling via passive isolation. The result was a 38% reduction which pointed to the improved part roughness results. In addition to the parts discussed in Section 3.3.3.2, part roughness values were recorded for parts produced with passive isolation. The seven samples had an average roughness of 850.39 μin . This result was a 16% reduction compared to those printed without isolation as those ten parts had a mean of 1015.60 μin . This analysis has a weak statistical basis like the discussion from Section 3.3.3.2 due to its sample size, which could be improved by collecting more samples. Although this passive isolation scheme was not optimized, it improved part quality in quantitative part roughness and demonstrated vibration mitigation as a helpful scheme for improving AM part quality.

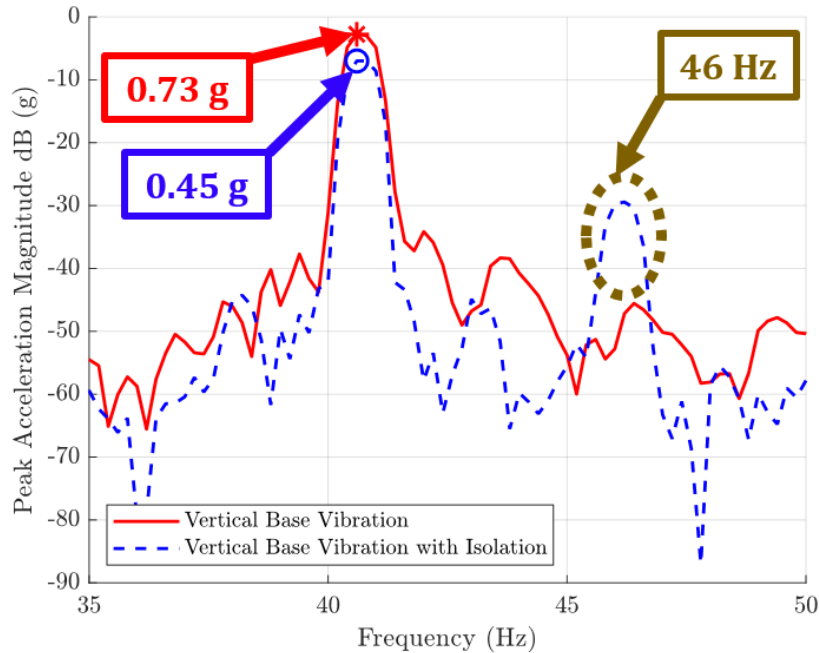
A few more tests were performed on the Dongling shaker and are omitted here, but their results are in B.3. These tests include no vibration without isolation, vibration at an input threshold with and without isolation, and vibration at other input levels with and without isolation. Note that the test with vibration at an input threshold refers to a test where the use of passive isolation resulted in similar part quality as parts printed without vibration or isolation. Put another way; the amplitude threshold was an input level that the isolation design could sufficiently mitigate vibration effects on part quality. Comparisons of parts printed during the tests in B.3 are in B.4.



(a) No isolation.



(b) With 3 sponge rubber hockey puck isolation.



(c) The curves are maximum values for data recorded while the printer applied one extruded material layer. One curve was from a test with passive isolation and the other without. Both resulted from vertical base vibration on the printer at 0.1 g and 40.7 Hz. Circled at 46 Hz is a new mode that is an artifact of using passive isolation. This new mode is still a factor of 22 lower than the targeted frequency of 40.7 Hz. Notice the 38% reduction of the response once isolation is introduced.

Figure 3.30: Relative motion between the print head and print bed for two scenarios: with and without passive vibration isolation. The data was measured between the print head and print bed accelerometers (see Figure 3.24).

3.3.3.4 Summary

An overall practical approach to understand how base vibration affects AM part quality was given in Figure 3.1. However, with the understanding developed through this study, a modified approach is suggested for future work to mitigate vibration effects on AM part quality directly. The adapted approach in Figure 3.31 has the same structure as Figure 3.1, but with a modified path to go straight from a part quality metric decision to assessing how the metric is affected by base vibration and then mitigate it. Although the present work is not exhaustive, the modified path is recommended. This study's results showed that relative vertical motion between the print bed and head dominated the printer's vibration response, which can serve as an assumption for future work. The main thing needed then before analyzing the vibration effects and applying a mitigation strategy is an understanding of the print bed and head relative motion response for a frequency range of interest. Understanding this response would reveal the printer's vibration modes and an allowable amplitude threshold that could be targeted with an active or passive vibration mitigation scheme. With the current groundwork laid, the vast literature of vibration mitigation for precision machines can be investigated to select an appropriate scheme to enable AM deployment in harsh environments.

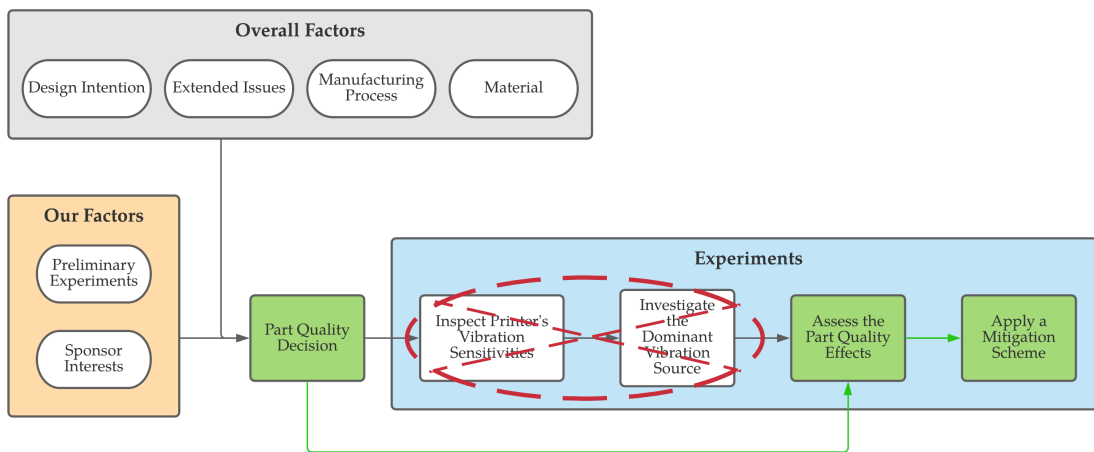


Figure 3.31: An adapted overall approach of this research indicates how future work can use the present results to move directly from a part quality metric decision to testing vibration effects and mitigating them. The present results support the assumption that relative vertical print bed and head vibration dominate an extrusion printer's vibration response and should be the focus for applying a vibration mitigation scheme.

Chapter 4

Final Remarks¹

This chapter concludes the thesis with a summary of the preceding chapters followed by future work suggestions for continuing and extending this research. The experimental efforts are described first; then, a brief description zooms out to the U.S. Navy's hopes for AM at large. The purpose of this chapter is to wrap up the discussions of this thesis.

¹Portions of this chapter will be submitted to *Additive Manufacturing*

4.1 Summary and Conclusion

Experimental Efforts

In summary, part surface roughness was selected to measure additive manufactured (AM) part quality for an extrusion-type printer. The decision was based on preliminary experimental observations and the design intention informed by the research sponsor. The printer's vibration-sensitive components were identified as the print bed and print head gantry by a refined modal impact test. The printer's vibration response was considered to have two sources: machine vibration from rapid printer motion and experimentally induced base vibration. Base vibration effects dominated the response, but future experiments using horizontal excitation to excite resonances in the horizontal direction could provide further understanding. The relative motion between the print bed and print head gantry indicates an area to target with vibration mitigation strategies for similar printers and environments. Part roughness correlated with base vibration intensity for an experiment that vertically vibrated the printer during part production. A passive vibration mitigation scheme was implemented to demonstrate the overall experimental approach.

Previous work in the literature has only investigated how machine vibration affects

AM part quality, whereas this thesis touched on machine vibration *and* base vibration as sources. Base vibration effects were the focus as they were shown to dominate the printer's vibration response. Because of AM machine sensitivities to vibration, such equipment was considered as precision machinery. Precision machines have been studied, and mitigation solutions applied extensively in the literature. The primary issue for precision machines is often the relative motion between their components, which hinders machine function and accuracy. The same issue is valid for AM equipment as vibration misaligns components which leads to low part quality.

The U.S. Navy's Situation

The efforts provided in this thesis were distilled from an understanding of U.S. Navy ship environments. Vibration was the focus up to 100 Hz as it was previously identified as an issue for AM on Navy ships. Factors generating noise and vibration in military marine environments have received mitigation attempts in the literature. However, the noise is not expected to be gone completely, so this research to enable AM on ships is needed.

The U.S. Navy wants vibration effects on AM printing addressed to exploit AM to simplify their supply chains and minimize the dependency on docking for supplies. Furthermore, others may benefit from this work as it points towards other harsh

environments that AM could advance.

4.2 Work Outlook

Several points of future work were described throughout the thesis but are reiterated and extended here for completeness. Consider the future work based on three thought streams:

1. Experimental identification of AM printers' vibration responses.
2. Understanding vibration effects on AM part quality and mitigating them.
3. Extending this research's findings to other harsh environments.

The first two points are closely connected to the present work and are derived from the updated flowchart (Figure 3.31) in Chapter 3. The first point considers the crossed-out steps in the flowchart. These steps were crossed out because they were part of the conclusion from the experimental results to focus on the print bed and print head gantry relative motion for mitigating vibration effects. These steps were *not* crossed out because they were exhausted, as it is understood that further work could be done here. A few ideas for future work include:

- Examine horizontal base vibration effects and vibration mode coupling between

horizontal and vertical.

- Experiments on more printers to validate that the print bed and head relative motion dominate the vibration response leading to AM part quality.
- Explore ways of online identification of low order modes since these results showed that damping the low order mode reduced the peak vibration response leading to improved part quality.
- Further exploration of resonance variance with the printer moving. Modal analysis assumes a static structure while the printer moves and varies the mode shapes and frequencies.

The second thought stream could trigger the following future work:

- Explore different methods for measuring AM part quality (i.e., internal defects and strength).
- Explore different printed materials (i.e., metal may be desirable for the U.S. Navy and others).
- Test vibration mitigation schemes using traditional methods or modern ones, including machine learning².

²This is next on the timeline for the funding project [13].

Finally, on the last point, with a small step here, others could jump on the bandwagon to begin efforts for deploying AM on moving vehicles, on spacecraft, on airplanes (Figure 4.1).

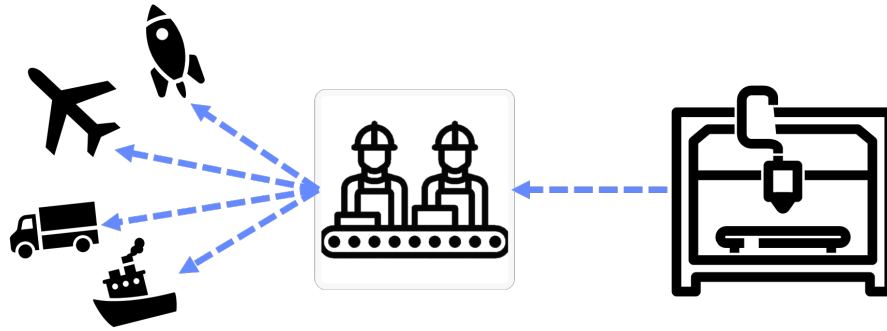


Figure 4.1: Potential future of AM deployed in harsh environments.

References

- [1] Udriou, R.; Braga, I. C.; Nedelcu, A. *Materials* **2019**.
- [2] Huang, S. H.; Liu, P.; Mokasdar, A.; Hou, L. *International Journal of Advanced Manufacturing Technology* **2012**.
- [3] Kenney, M. E. Cost reduction through the use of additive manufacturing (3d printing) and collaborative product lifecycle management technologies to enhance the navy's maintenance programs Master's thesis, Naval Postgraduate School, **2013**.
- [4] 3d printing: Imagine a brigade producing parts on battlefield. Jeckell, J. January , **2014**.
- [5] Department of the navy (don) additive manufacturing (am) implementation plan v2.0 (2017). Burrow, J.; Cullom, P.; Dana, M. May , **2017**.
- [6] Navy warship is taking 3d printer to sea; don't expect a revolution. Freedberg, S. J. April , **2014**.

- [7] Strickland, J. D. In *Proceedings of the 13th International Symposium on PRactical Design of Ships and Other Floating Structures (PRADS' 2016)*, 2016.
- [8] Deja, M.; Siemiatkowski, M. S.; Zielinski, D. *POLISH MARITIME RESEARCH* **2020**.
- [9] Omer, H.; Bekker, A. feb **2018**, *67*, 71–82.
- [10] Carlton, J. S.; Vlašić, D. In *1st International Ship Noise and Vibration Conference: London, June 20-21, 2005*, 2005.
- [11] Borelli, D.; Gaggero, T.; Rizzuto, E.; Schenone, C. *Noise Mapping* **2016**, *3*, 107–119.
- [12] Dylejko, P. G.; Kessissoglou, N. J.; Tso, Y.; Norwood, C. J. feb **2007**, *300*(1-2), 101–116.
- [13] Ship vibration mitigation for additive manufacturing equipment: Navy sttr 2020.a - topic n20a-t010. Putnam, D. January , **2020**.
- [14] General overview of ship structural vibration problems Technical report, Lloyd's Register, **2015**.
- [15] Mil-std-810h - environmental engineering considerations and laboratory tests Technical report, Department of Defense, **2019**.
- [16] DeBra, D. B. *Annals of the CIRP* **1992**, *41*.

- [17] Perner, M.; Algermissen, S.; Keimer, R.; Monner, H. P. *Robotics and Computer-Integrated Manufacturing* **2016**, *38*, 82–92.
- [18] Gordon, C. G. In *Proceedings of SPIE*, Vol. 1619, 1992.
- [19] Duan, M.; Yoon, D.; Okwudire, C. E. *Mechatronics* **2017**.
- [20] Rivin, E. I. *Precision Engineering* **1995**, *17*, 41–56.
- [21] Lee, J.; Okwudire, C. E. *Precision Engineering* **2016**, *43*, 164–177.
- [22] Kim, C.-J.; Oh, J.-S.; Park, C.-H. *CIRP Annals - Manufacturing Technology* **2014**, *63*, 349–352.
- [23] Kam, M.; Saruhan, H.; İpekçi, A. *Düzce Üniversitesi Bilim ve Teknoloji Dergisi* **2019**, *7*, 147–157.
- [24] Pilch, Z.; Domin, J.; Szlapa, A. In *2015 Selected Problems of Electrical Engineering and Electronics (WZEE)*, 2015.
- [25] Johnson, K.; Blough, J.; Barnard, A.; Hartwig, T.; Brown, B.; Soine, D.; Cullom, T.; Kinzel, E.; Bristow, D.; Landers, R. In *Proceedings of the 29th Annual International Solid Freeform Fabrication Symposium*, 2018.
- [26] Allen, A.; Johnson, K.; Blough, J. R.; Barnard, A.; Hartwig, T.; Brown, B.; Soine, D.; Cullom, T.; Bristow, D.; Landers, R.; Kinzel, E. In *Sensors and Instrumentation, Aircraft/Aerospace, Energy Harvesting & Dynamic Environments Testing*, Vol. 7, pages 77–84, 2021.

- [27] Echeta, I.; Feng, X.; Dutton, B.; Leach, R.; Piano, S. *The International Journal of Advanced Manufacturing Technology* **2020**.
- [28] Townsend, A.; Senin, N.; Blunt, L.; Leach, R.; Taylor, J. *Precision Engineering* **2016**, *46*, 34–47.
- [29] Sanaei, N.; Fatemi, A. *Theoretical and Applied Fracture Mechanics* **2020**.
- [30] Rivin, E. I. *Passive Vibration Isolation*; The American Society of Mechanical Engineers (ASME), 2003.
- [31] Crede, C. E. *Vibration and Shock Isolation*; John Wiley and Sons, Inc., 1951.

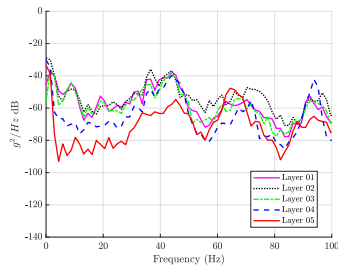
Appendix A

Vibration-Sensitive Components

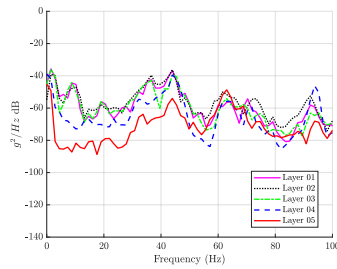
Data

A.1 Initial Testing

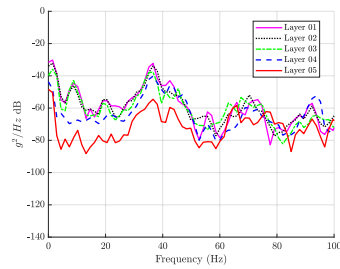
Print Operation Experiment



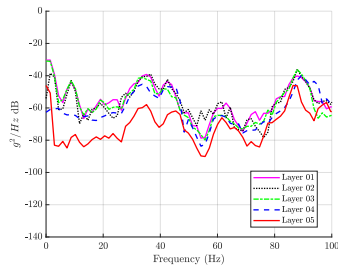
(a) Head 7



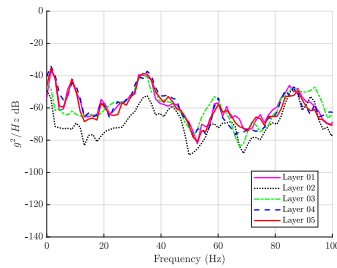
(b) Head 8



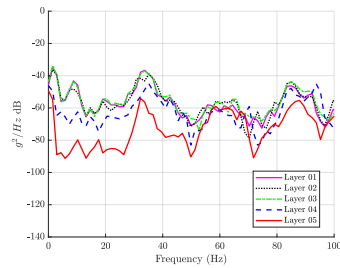
(c) Head 9



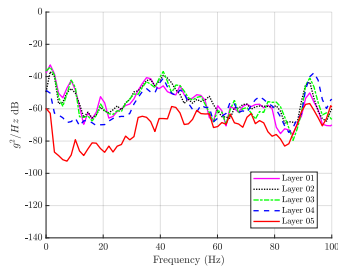
(d) Head 4



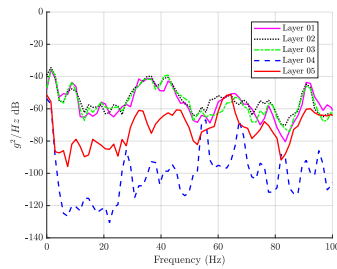
(e) Head 5



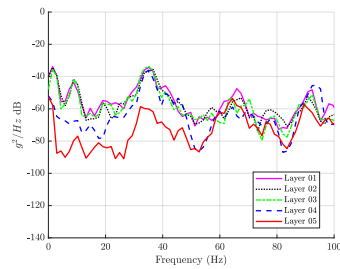
(f) Head 6



(g) Head 1

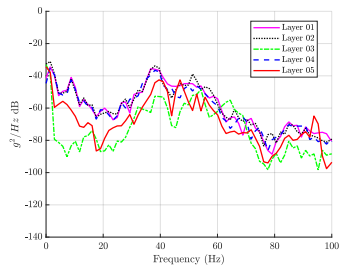


(h) Head 2

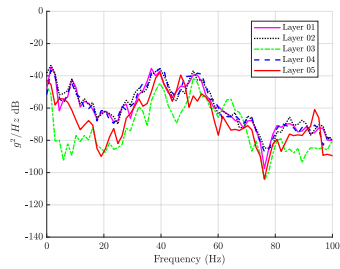


(i) Head 3

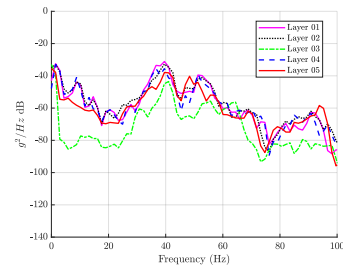
Figure A.1: Averaged power spectral density functions (PSDs) for the Spot 01 accelerometer location from Figure 3.5. Plotted are curves recorded during each material layer for a given print head position as in Figure 3.6.



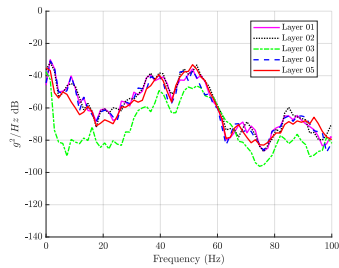
(a) Head 7



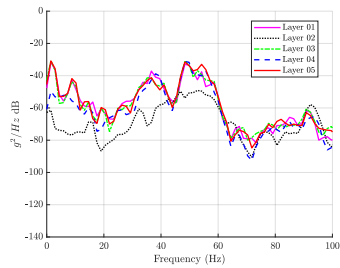
(b) Head 8



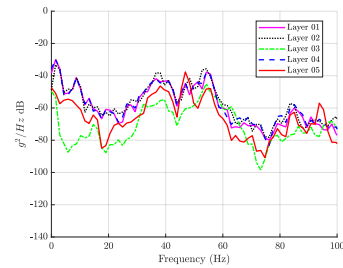
(c) Head 9



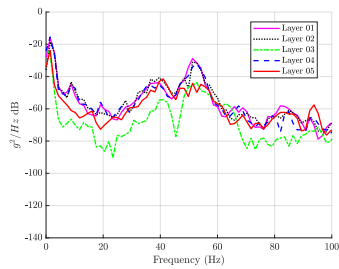
(d) Head 4



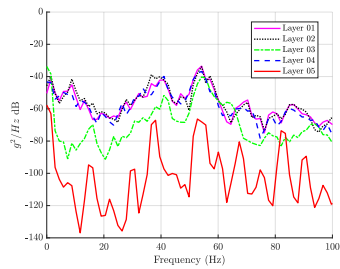
(e) Head 5



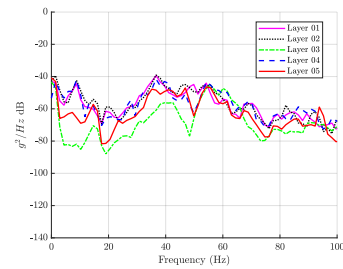
(f) Head 6



(g) Head 1



(h) Head 2



(i) Head 3

Figure A.2: Averaged power spectral density functions (PSDs) for the Spot 06 accelerometer location from Figure 3.5. Plotted are curves recorded during each material layer for a given print head position as in Figure 3.6.

A.2 Refined Testing

The modal analysis for both the print bed and gantry shown here was performed when the printer was in the “centered” bottom configuration as shown in Figure 3.12.

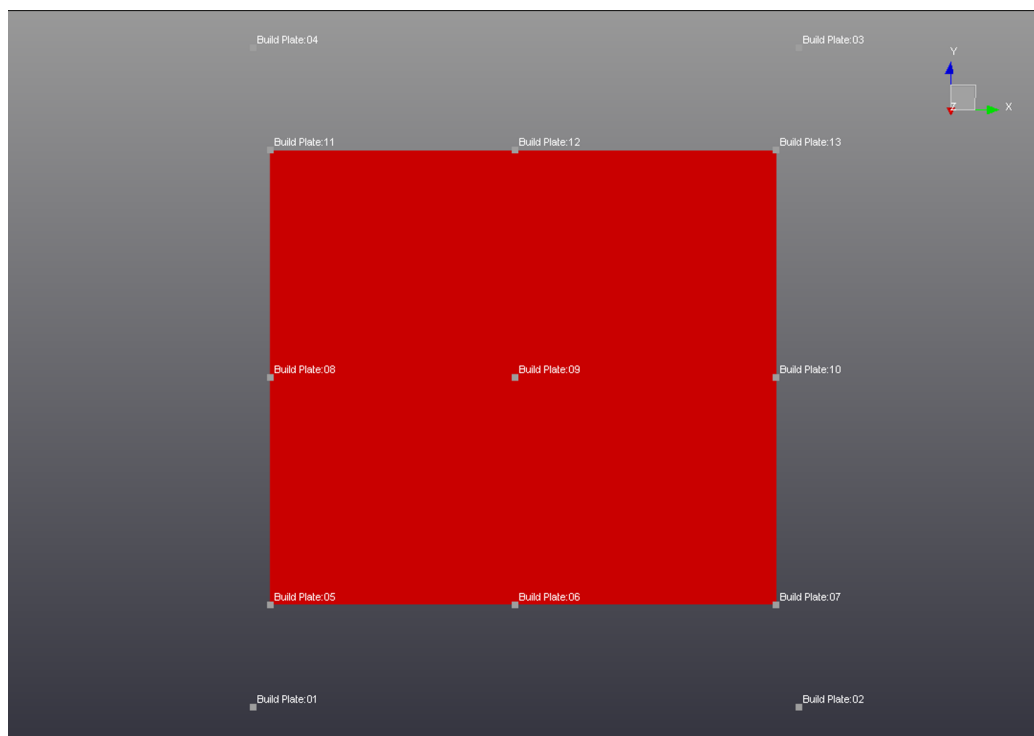


Figure A.3: Print bed/build plate geometry. This layout was used for recording vibration data according to specific nodes.

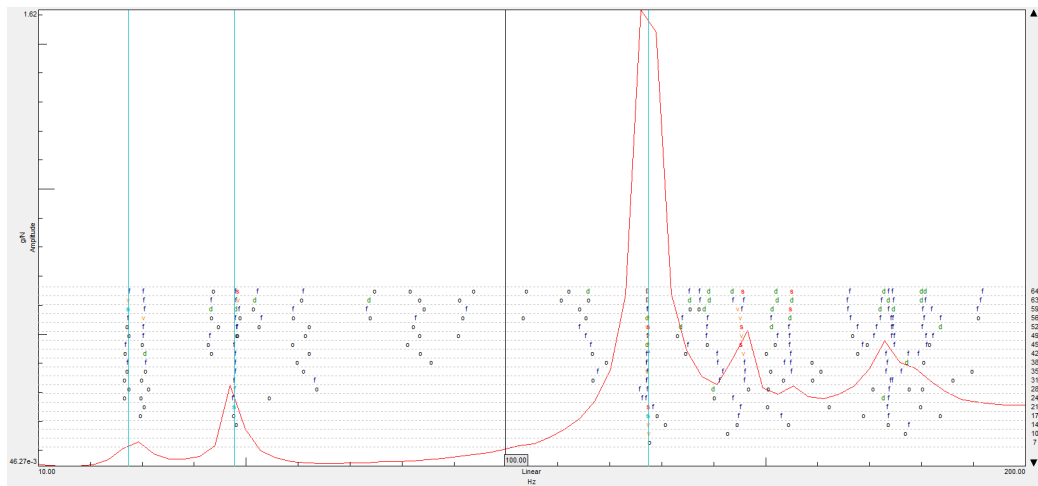
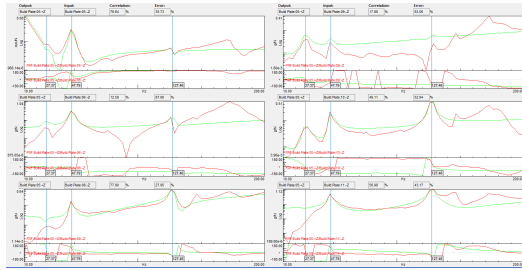
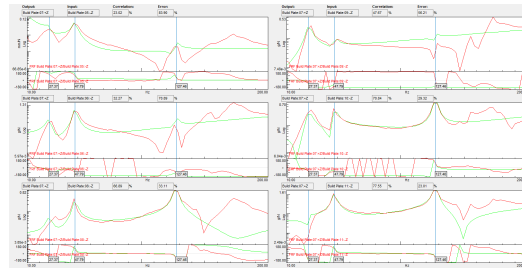


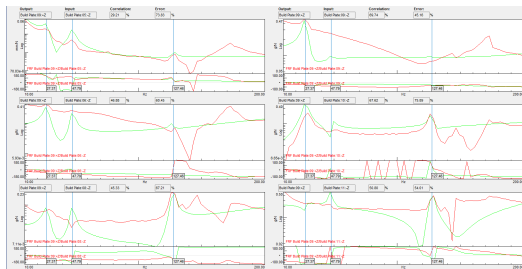
Figure A.4: Stabilization diagram for modal analysis with the print bed vibration data. Pole selections are highlighted.



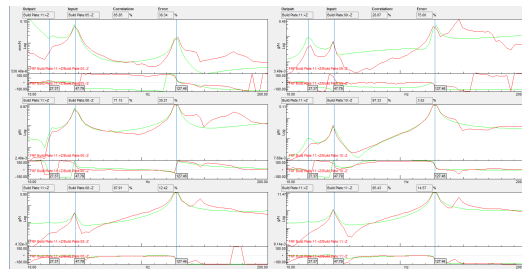
(a)



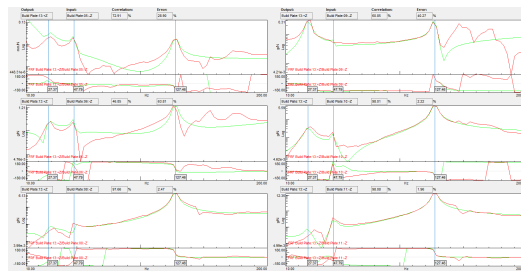
(b)



(c)

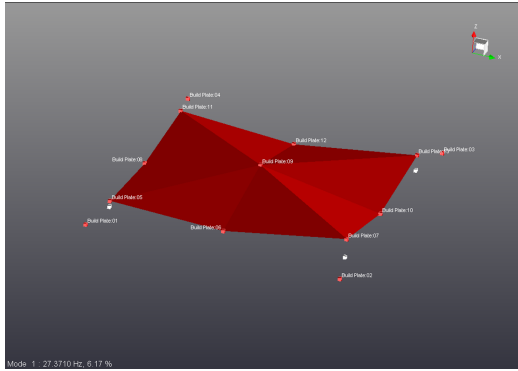


(d)

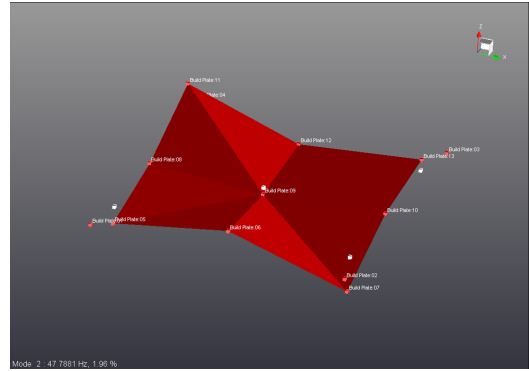


(e)

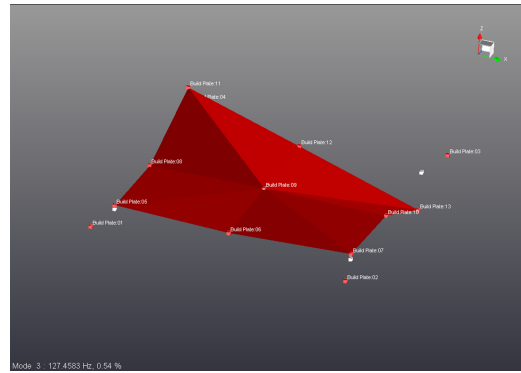
Figure A.5: Experimental and synthesized frequency response function estimates (FRFs) for the print bed modal analysis. Pole selections are highlighted.



(a)



(b)



(c)

Figure A.6: Mode shapes manifest on the print bed.

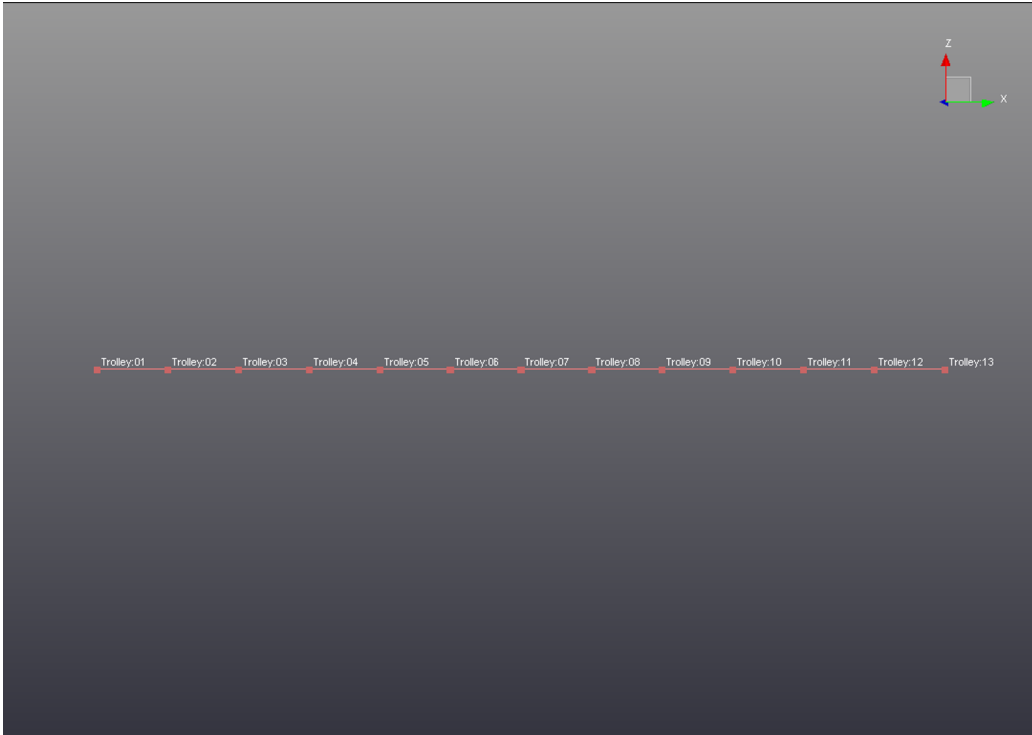


Figure A.7: Gantry/trolley geometry. This layout was used for recording vibration data according to specific nodes.

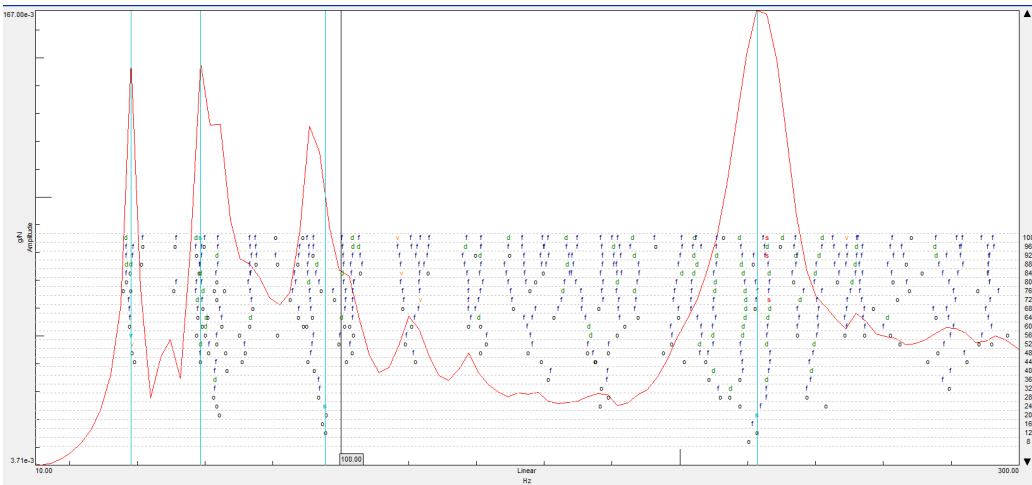
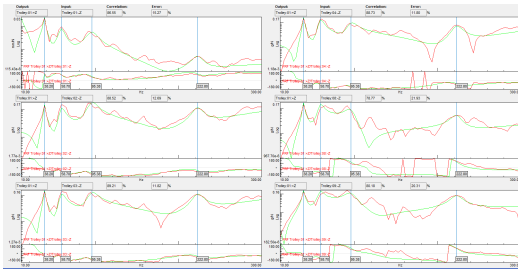
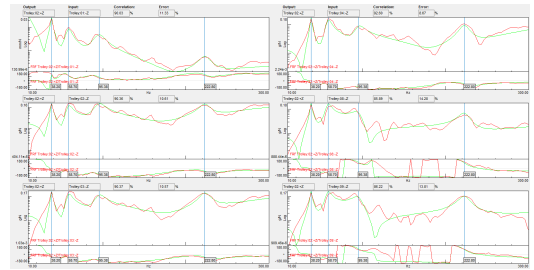


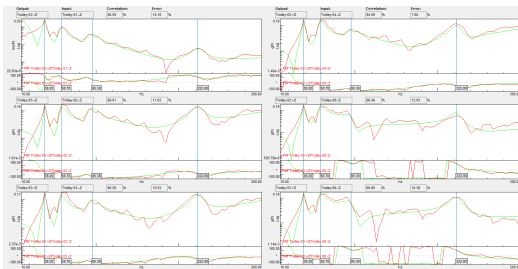
Figure A.8: Stabilization diagram for modal analysis with the gantry vibration data. Pole selections are highlighted.



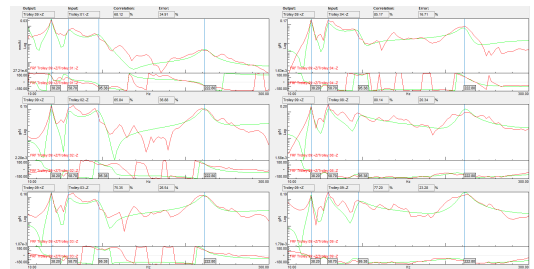
(a)



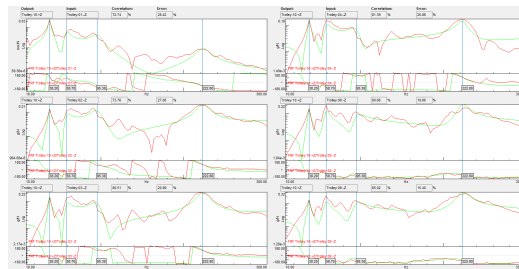
(b)



(c)

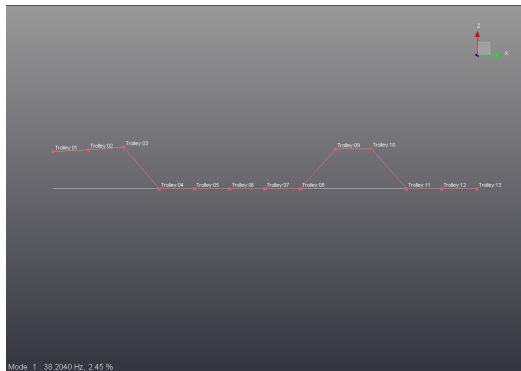


(d)

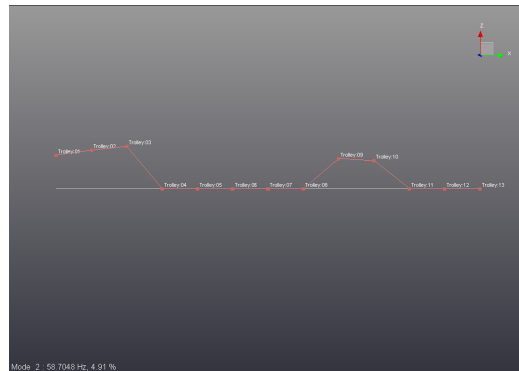


(e)

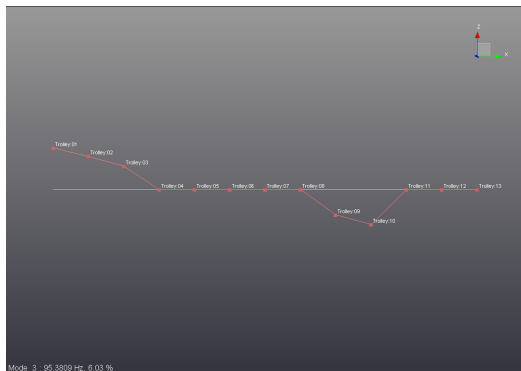
Figure A.9: Experimental and synthesized frequency response function estimates (FRFs) for the gantry modal analysis. Pole selections are highlighted.



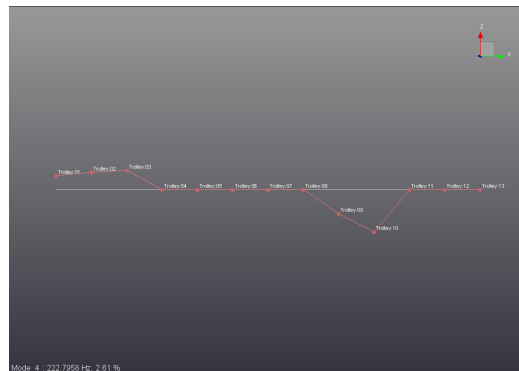
(a)



(b)



(c)

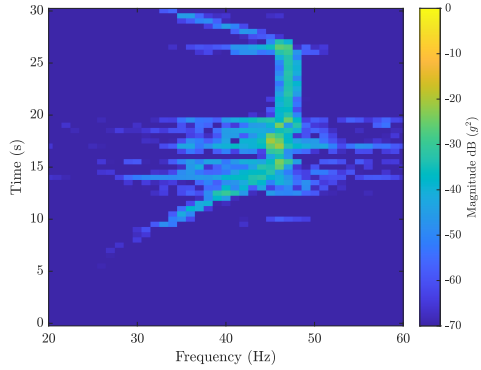


(d)

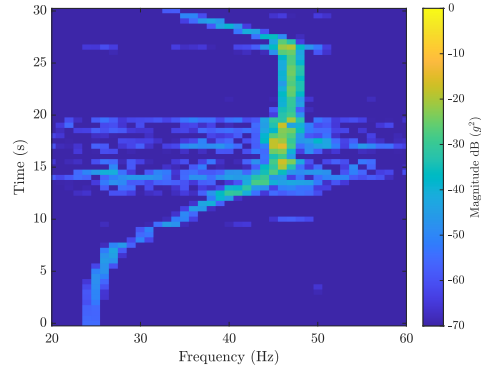
Figure A.10: Mode shapes manifest on the gantry. Note that nodes without motion correspond to areas where data was not collected or was corrupted. The main obstruction was the print heads centered on the gantry.

A.3 Shaker Testing Preparation

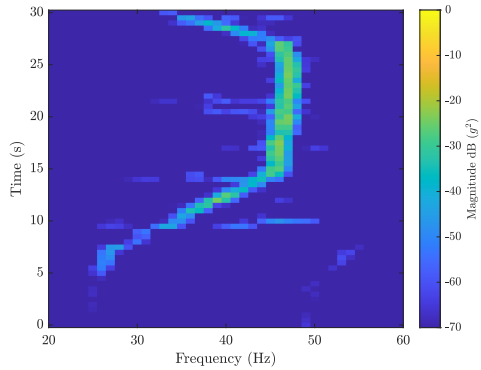
Modal Shaker Tests



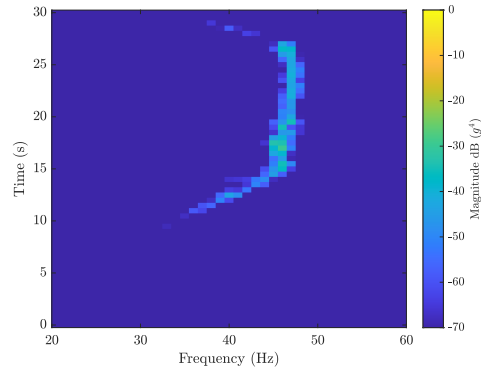
(a) Crosspower colormap of the shaker and print head accelerometer. The complex conjugate of the shaker was pre-multiplied by the print head; both were linear spectrum acceleration data. Key point(s): 40, 46-47 Hz



(b) Crosspower colormap of the shaker and print bed accelerometer. The complex conjugate of the shaker was pre-multiplied by the print bed; both were linear spectrum acceleration data. Key point(s): 45-47 Hz

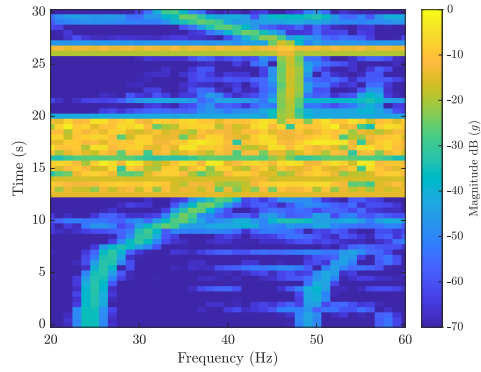


(c) Crosspower colormap of the print head and print bed accelerometer. The complex conjugate of the print head was pre-multiplied by the print bed; both were linear spectrum acceleration data. Key point(s): 40, 46-47 Hz

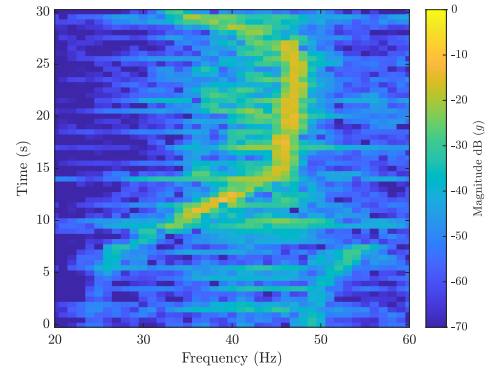


(d) Crosspower colormap of the shaker and print head/print bed crosspower from Figure 3.22(c) accelerometer. The complex conjugate of the shaker was pre-multiplied by the print head/print bed crosspower from Figure 3.22(c); both were linear spectrum acceleration data. Key point(s): 45-47 Hz

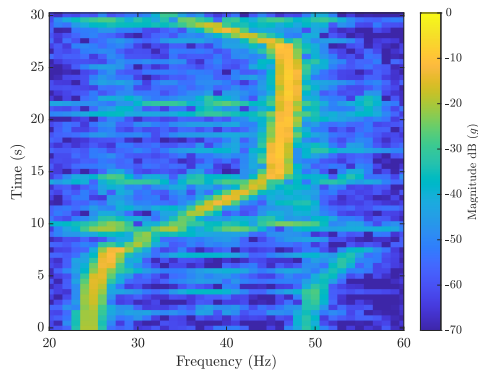
Figure A.11: Crosspower colormap recordings during a manual sine sweep from ≈ 25 -50 Hz.



(a) Colormap of the shaker linear spectrum acceleration data. Key point(s): 46-47 Hz

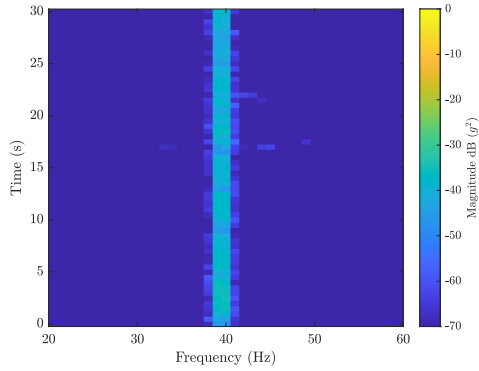


(b) Colormap of the print head linear spectrum acceleration data. Key point(s): 34-47 Hz

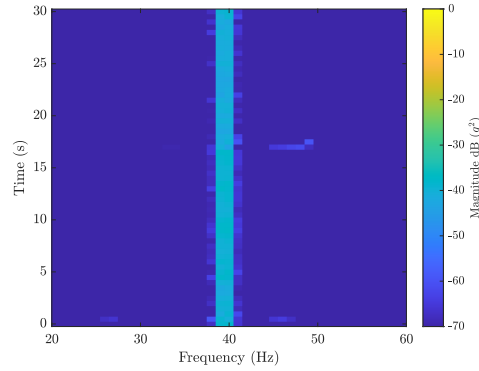


(c) Colormap of the print bed linear spectrum acceleration data. Key point(s): 24-28, 37-47 Hz

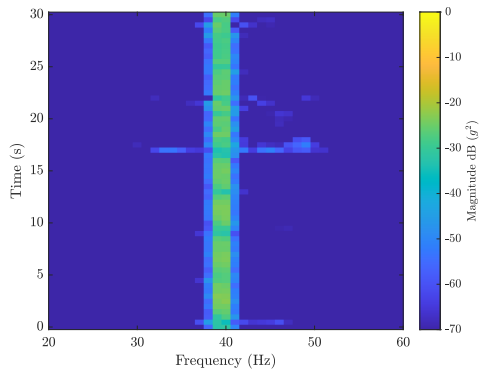
Figure A.12: Colormap recordings during a manual sine sweep from \approx 25-50 Hz.



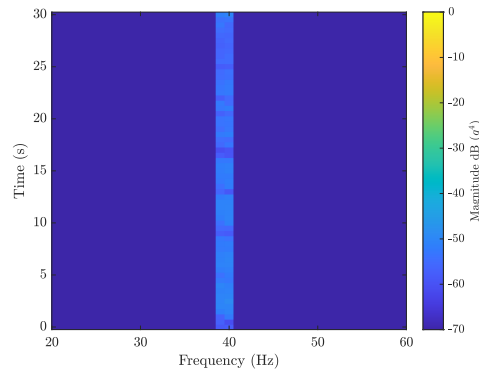
(a) Crosspower colormap of the shaker and print head accelerometer. The complex conjugate of the shaker was pre-multiplied by the print head; both were linear spectrum acceleration data.



(b) Crosspower colormap of the shaker and print bed accelerometer. The complex conjugate of the shaker was pre-multiplied by the print head; both were linear spectrum acceleration data.

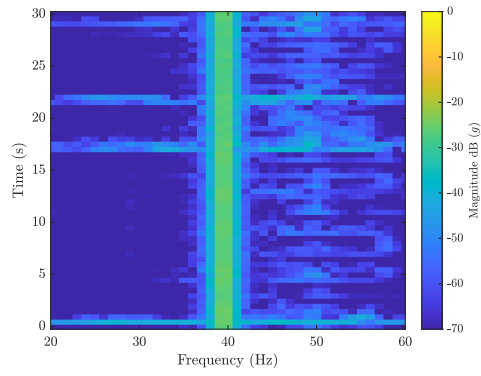


(c) Crosspower colormap of the print head and print bed accelerometer. The complex conjugate of the shaker was pre-multiplied by the print head; both were linear spectrum acceleration data.

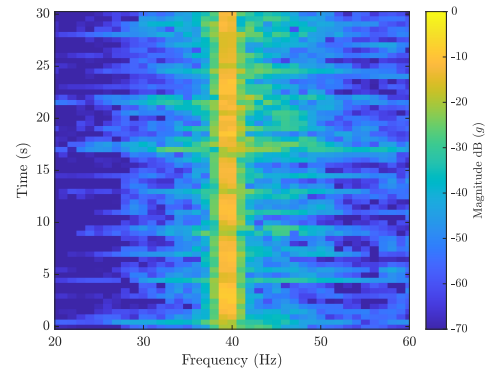


(d) Crosspower colormap of the shaker and print head/print bed crosspower from Figure 3.22(c) accelerometer. The complex conjugate of the shaker was pre-multiplied by the print head/print bed crosspower from Figure 3.22(c); both were linear spectrum acceleration data.

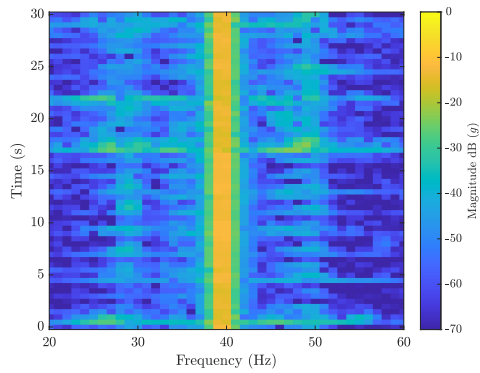
Figure A.13: Crosspower colormap recordings during a sine input at ≈ 40 Hz.



(a) Colormap of the shaker linear spectrum acceleration data.



(b) Colormap of the print head linear spectrum acceleration data.



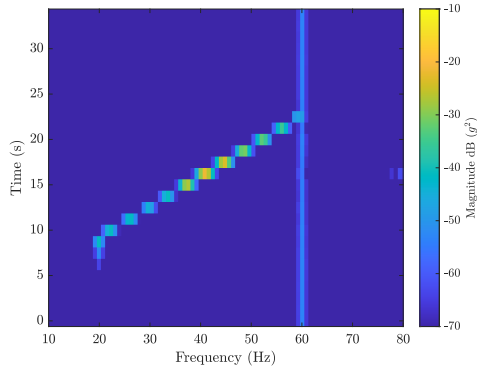
(c) Colormap of the print bed linear spectrum acceleration data.

Figure A.14: Colormap recordings during a sine input at ≈ 40 Hz.

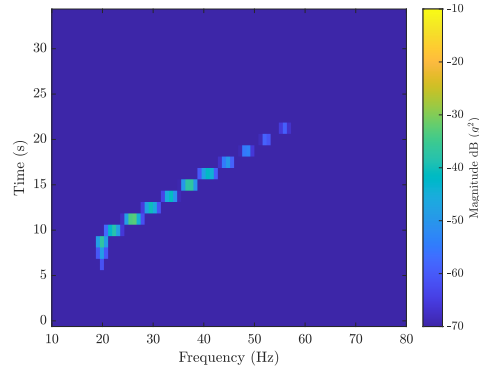
Appendix B

Vibration Effects Experiment Data

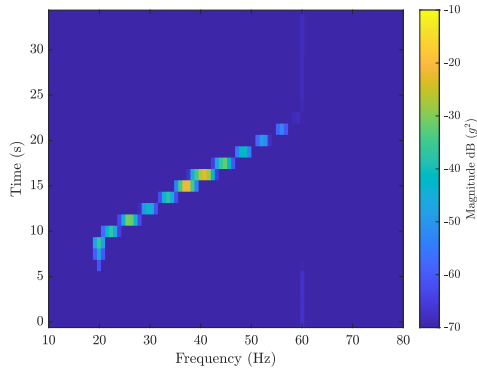
B.1 Dongling Shaker Sweep Boundary Condition Check



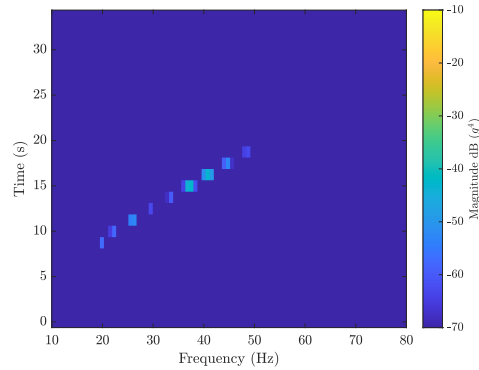
(a) Crosspower colormap of the shaker and print head accelerometer. The complex conjugate of the shaker was pre-multiplied by the print head; both were linear spectrum acceleration data.



(b) Crosspower colormap of the shaker and print bed accelerometer. The complex conjugate of the shaker was pre-multiplied by the print bed; both were linear spectrum acceleration data.

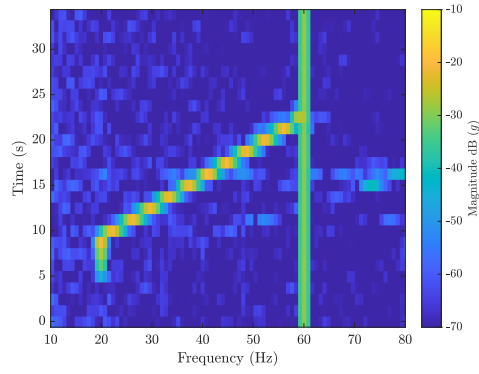


(c) Crosspower colormap of the print head and print bed accelerometer. The complex conjugate of the print head was pre-multiplied by the print bed; both were linear spectrum acceleration data.

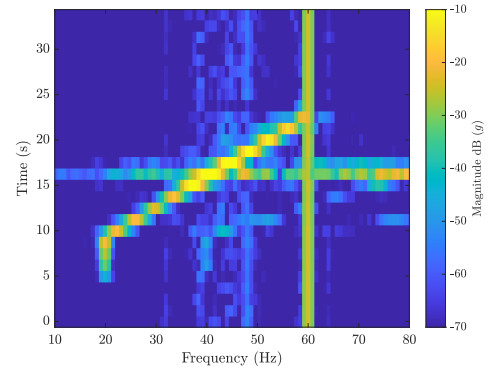


(d) Crosspower colormap of the shaker and print head/print bed crosspower from Figure 3.25(c) accelerometer. The complex conjugate of the shaker was pre-multiplied by the print head/print bed crosspower from Figure 3.25(c); both were linear spectrum acceleration data.

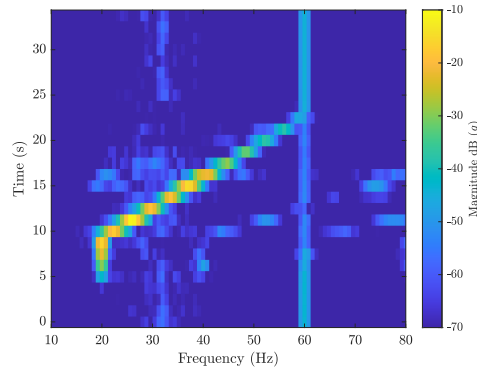
Figure B.1: Crosspower colormap recordings during a sine sweep from \approx 20-60 Hz corresponding to Figure 3.24.



(a) Colormap of the shaker linear spectrum acceleration data.



(b) Colormap of the print head linear spectrum acceleration data.



(c) Colormap of the print bed linear spectrum acceleration data.

Figure B.2: Colormap recordings during a sine sweep from ≈ 20 -60 Hz.

B.2 Dongling Shaker Passive Isolation Tuning

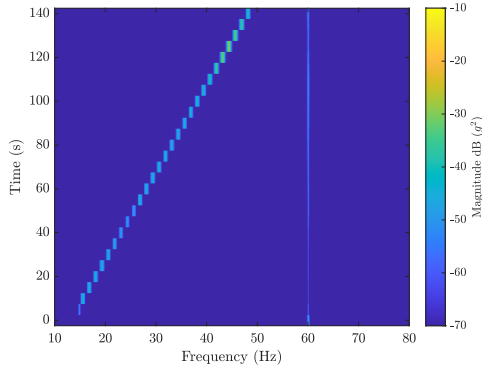
Parameters for the following results are shown in Table B.1.

Table B.1

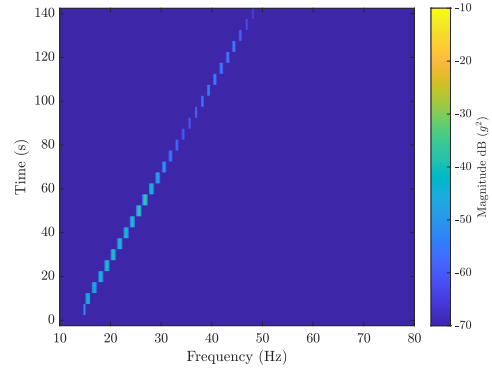
Experiment parameters for tests on the Dongling shaker to tune the passive isolation strategy.

Parameter	Value	Unit
Frequency Resolution (Δf)	0.2	Hz
Sampling Frequency (f_s)	2.56	kHz

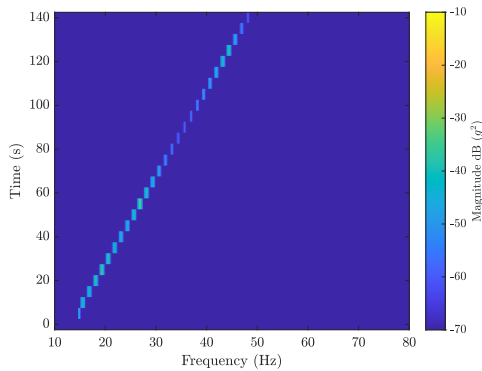
Three Sponge Rubber Hockey Pucks



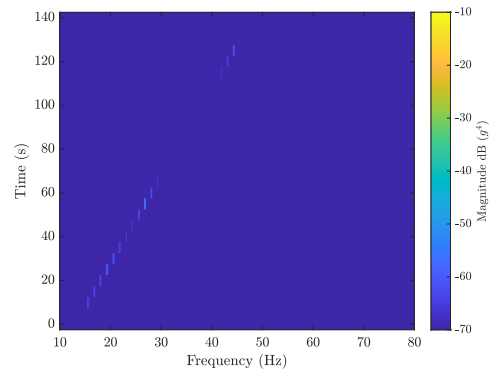
(a) Crosspower colormap of the shaker and print head accelerometer. The complex conjugate of the shaker was premultiplied by the print head; both were linear spectrum acceleration data.



(b) Crosspower colormap of the shaker and print bed accelerometer. The complex conjugate of the shaker was premultiplied by the print bed; both were linear spectrum acceleration data.

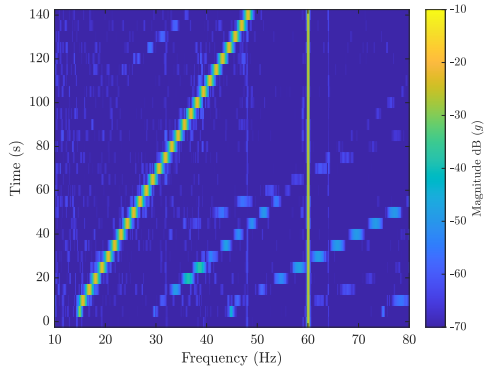


(c) Crosspower colormap of the print head and print bed accelerometer. The complex conjugate of the print head was premultiplied by the print bed; both were linear spectrum acceleration data.

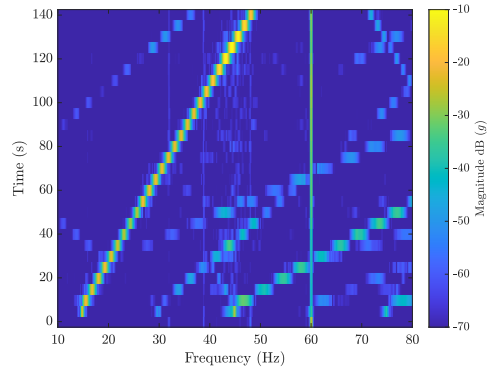


(d) Crosspower colormap of the shaker and print head/print bed crosspower from Figure B.3(c) accelerometer. The complex conjugate of the shaker was premultiplied by the print head/print bed crosspower from Figure B.3(c); both were linear spectrum acceleration data.

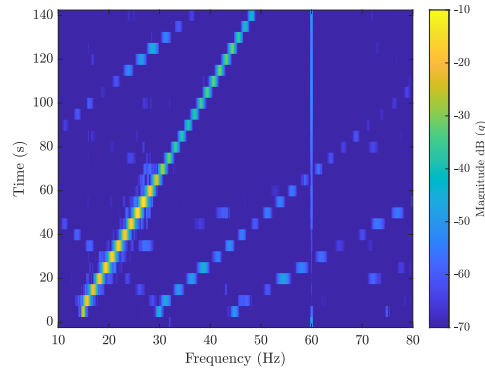
Figure B.3: Crosspower colormap recordings during a sine sweep corresponding to Figure 3.24.



(a) Colormap of the shaker linear spectrum acceleration data.



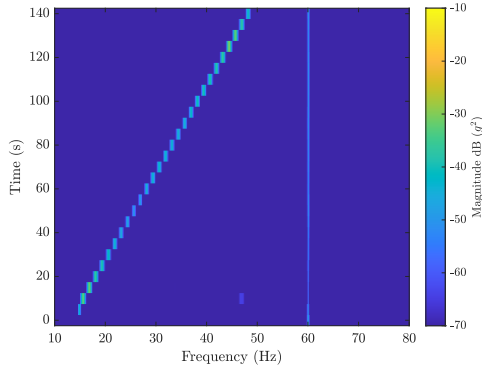
(b) Colormap of the print head linear spectrum acceleration data.



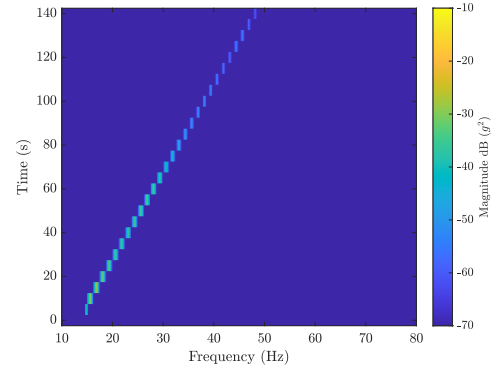
(c) Colormap of the print bed linear spectrum acceleration data.

Figure B.4: Colormap recordings during a sine sweep.

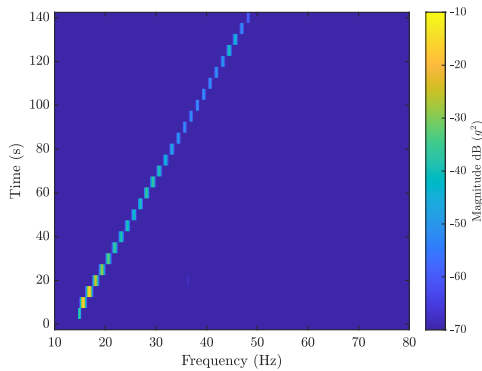
Four Sponge Rubber Hockey Pucks



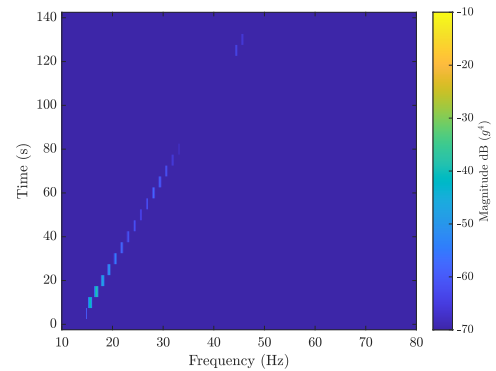
(a) Crosspower colormap of the shaker and print head accelerometer. The complex conjugate of the shaker was pre-multiplied by the print head; both were linear spectrum acceleration data.



(b) Crosspower colormap of the shaker and print bed accelerometer. The complex conjugate of the shaker was pre-multiplied by the print bed; both were linear spectrum acceleration data.

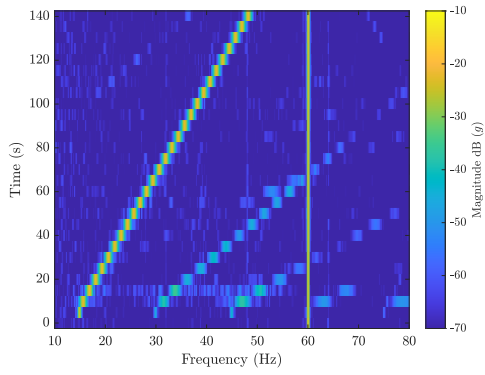


(c) Crosspower colormap of the print head and print bed accelerometer. The complex conjugate of the print head was pre-multiplied by the print bed; both were linear spectrum acceleration data.

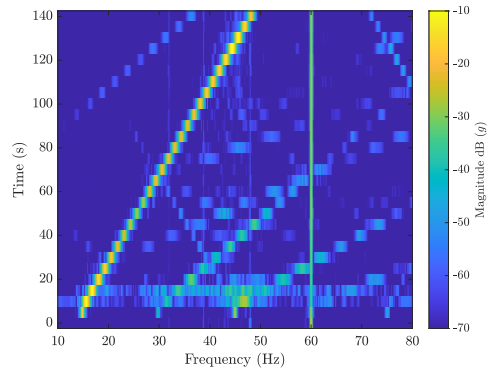


(d) Crosspower colormap of the shaker and print head/print bed crosspower from Figure B.5(c) accelerometer. The complex conjugate of the shaker was pre-multiplied by the print head/print bed crosspower from Figure B.5(c); both were linear spectrum acceleration data.

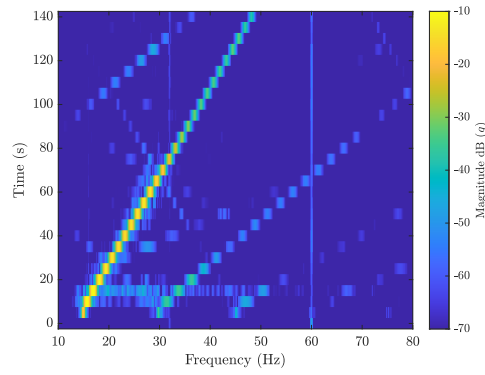
Figure B.5: Crosspower colormap recordings during a sine sweep corresponding to Figure 3.24.



(a) Colormap of the shaker linear spectrum acceleration data.



(b) Colormap of the print head linear spectrum acceleration data.



(c) Colormap of the print bed linear spectrum acceleration data.

Figure B.6: Colormap recordings during a sine sweep.

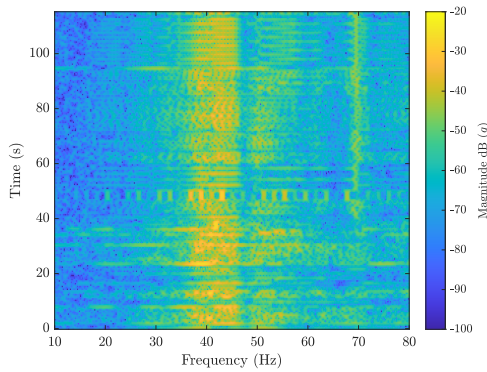
B.3 Dongling Shaker Other Tests

No Vibration and No Isolation

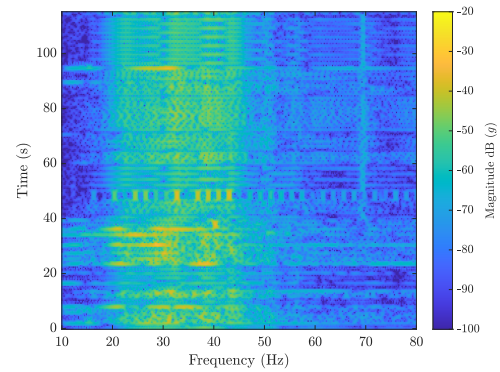
Parameters for the following results are shown in Table B.2.

Table B.2
Experiment parameters for tests on the Dongling shaker.

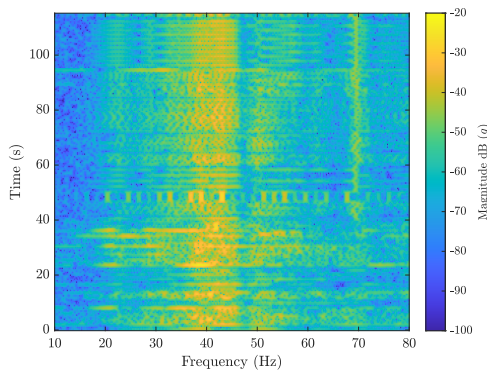
Parameter	Value	Unit
Frequency Resolution (Δf)	0.2	Hz
Sampling Frequency (f_s)	2.56	kHz



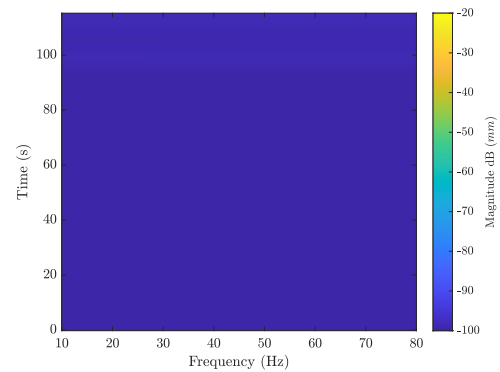
(a) Colormap of the print head linear spectrum acceleration data.



(b) Colormap of the print bed linear spectrum acceleration data.



(c) Colormap of the relative motion between the print head and print bed linear spectrum acceleration data.



(d) Colormap of the relative motion between the print head and print bed linear spectrum displacement data.

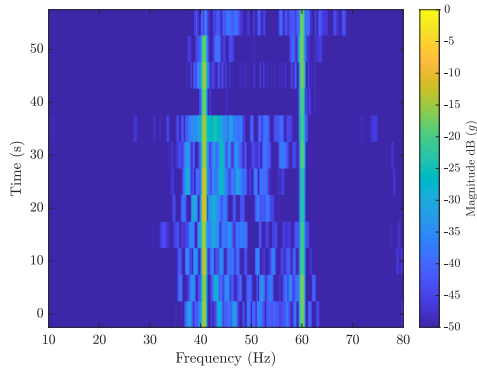
Figure B.7: Colormap recordings.

Vibration at an Input Threshold of 0.0325 g and No Isolation

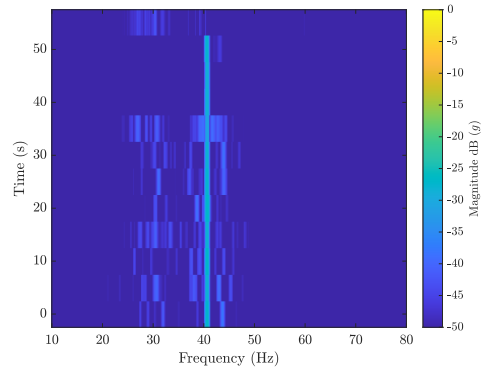
Parameters for the following results are shown in Table B.3.

Table B.3
Experiment parameters for tests on the Dongling shaker.

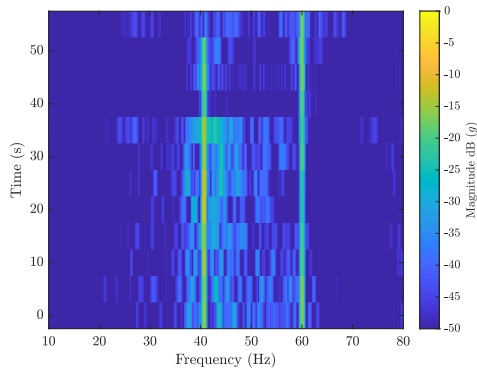
Parameter	Value	Unit
Frequency Resolution (Δf)	0.2	Hz
Sampling Frequency (f_s)	2.56	kHz



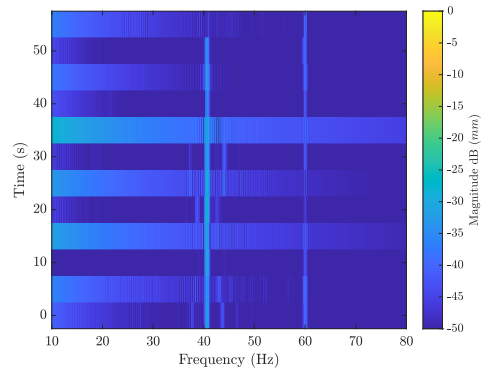
(a) Colormap of the print head linear spectrum acceleration data.



(b) Colormap of the print bed linear spectrum acceleration data.



(c) Colormap of the relative motion between the print head and print bed linear spectrum acceleration data.



(d) Colormap of the relative motion between the print head and print bed linear spectrum displacement data.

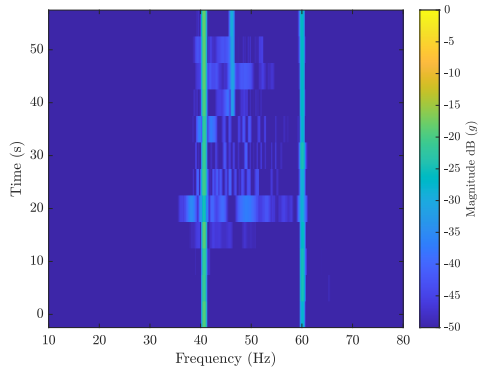
Figure B.8: Colormap recordings.

Vibration at an Input Threshold of 0.0325 g and 3 Sponge Rubber Hockey Puck Isolation

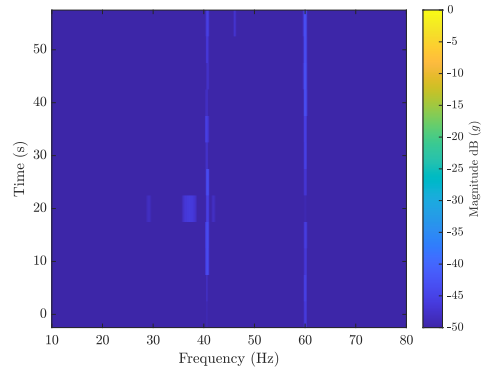
Parameters for the following results are shown in Table B.4.

Table B.4
Experiment parameters for tests on the Dongling shaker.

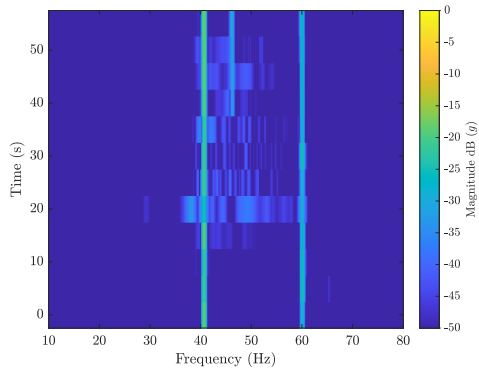
Parameter	Value	Unit
Frequency Resolution (Δf)	0.2	Hz
Sampling Frequency (f_s)	2.56	kHz



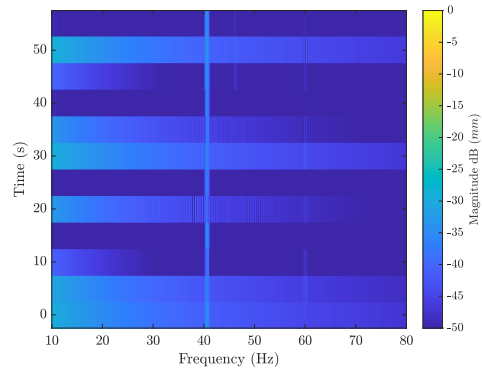
(a) Colormap of the print head linear spectrum acceleration data.



(b) Colormap of the print bed linear spectrum acceleration data.



(c) Colormap of the relative motion between the print head and print bed linear spectrum acceleration data.



(d) Colormap of the relative motion between the print head and print bed linear spectrum displacement data.

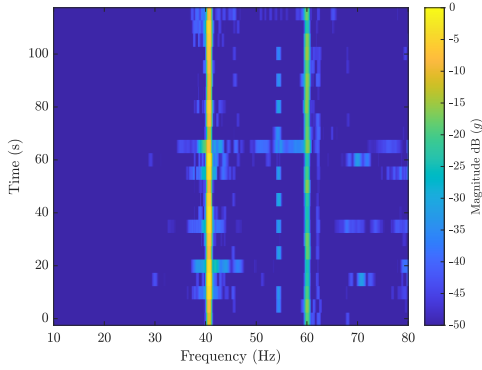
Figure B.9: Colormap recordings.

Vibration at an Input of 0.1 g and No Isolation

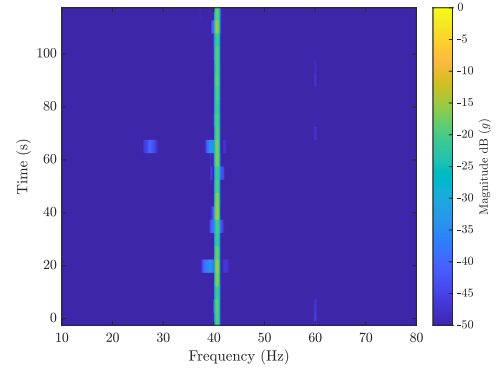
Parameters for the following results are shown in Table B.5.

Table B.5
Experiment parameters for tests on the Dongling shaker.

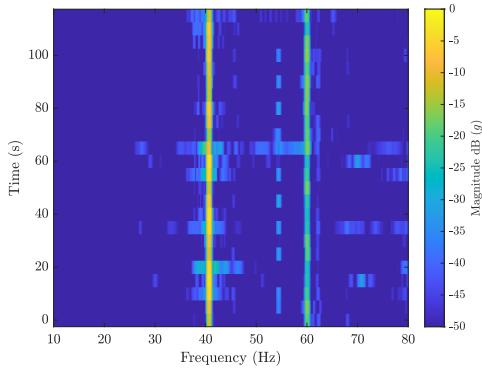
Parameter	Value	Unit
Frequency Resolution (Δf)	0.2	Hz
Sampling Frequency (f_s)	2.56	kHz



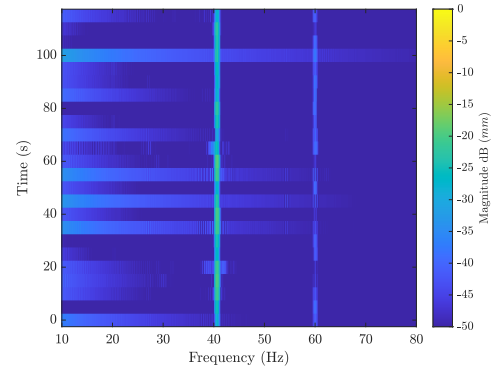
(a) Colormap of the print head linear spectrum acceleration data.



(b) Colormap of the print bed linear spectrum acceleration data.



(c) Colormap of the relative motion between the print head and print bed linear spectrum acceleration data.



(d) Colormap of the relative motion between the print head and print bed linear spectrum displacement data.

Figure B.10: Colormap recordings.

Vibration at an Input of 0.1 g and 3 Sponge Rubber Hockey

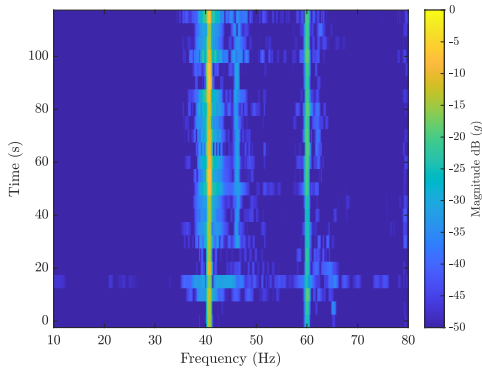
Puck Isolation

Parameters for the following results are shown in Table B.6.

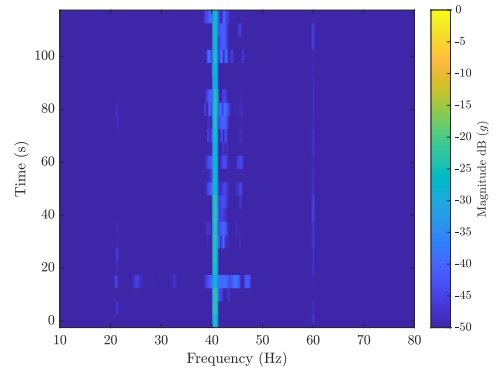
Table B.6

Experiment parameters for tests on the Dongling shaker.

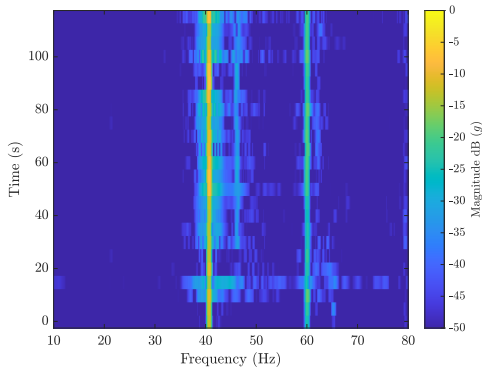
Parameter	Value	Unit
Frequency Resolution (Δf)	0.2	Hz
Sampling Frequency (f_s)	2.56	kHz



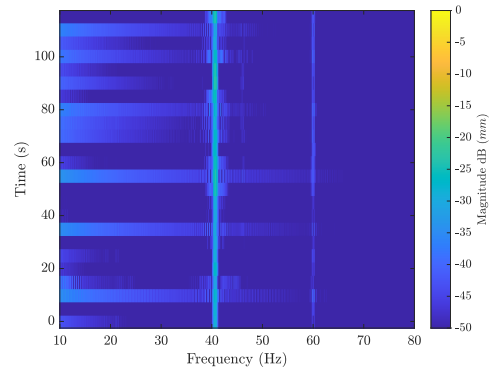
(a) Colormap of the print head linear spectrum acceleration data.



(b) Colormap of the print bed linear spectrum acceleration data.



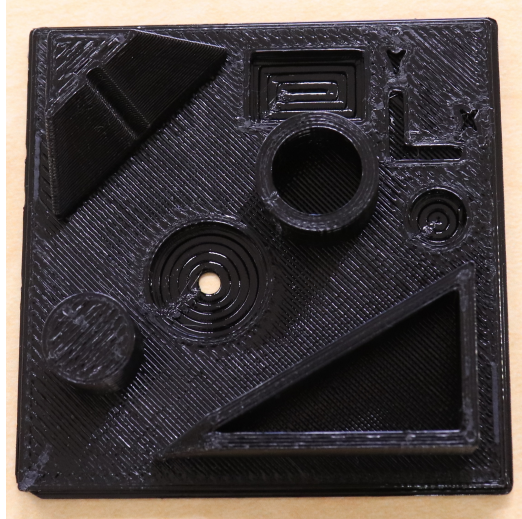
(c) Colormap of the relative motion between the print head and print bed linear spectrum acceleration data.



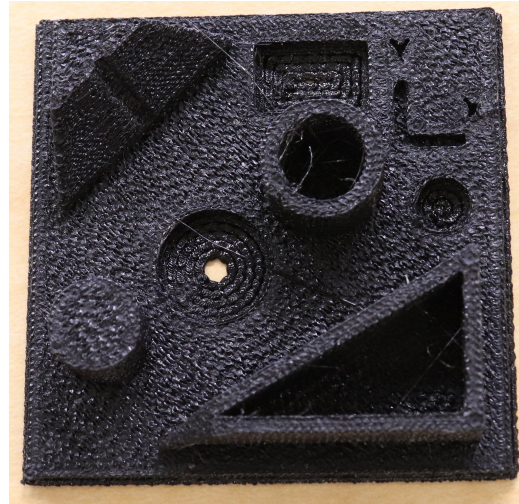
(d) Colormap of the relative motion between the print head and print bed linear spectrum displacement data.

Figure B.11: Colormap recordings.

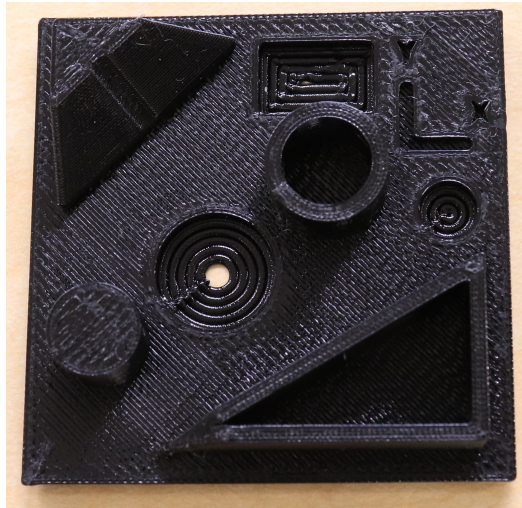
B.4 Printed Part Photos



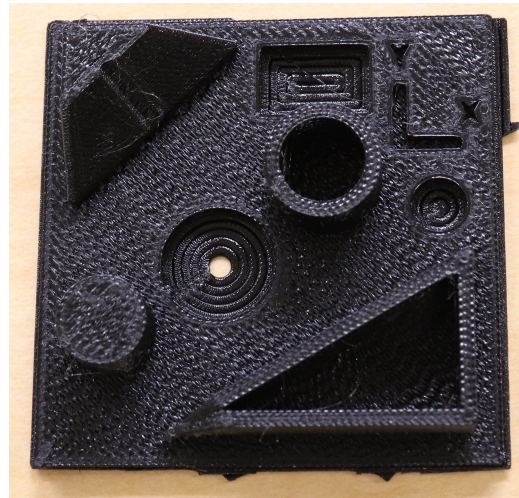
(a) No vibration. No isolation. Ra roughness: 237.65 μin .



(b) 0.13 g vibration at 40.7 Hz. No isolation. Ra roughness: 946.15 μin .

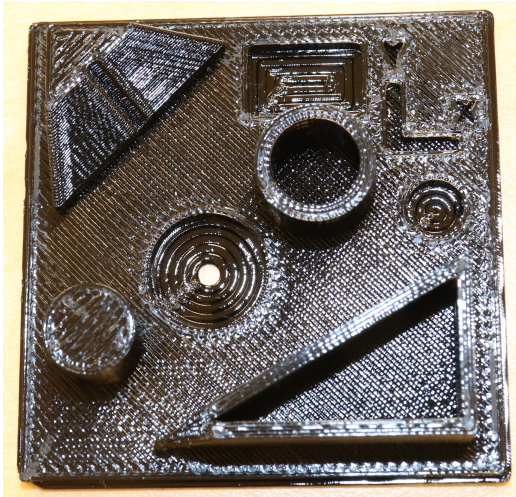


(c) 0.0325 g vibration at 40.7 Hz. 3 sponge hockey puck isolation. Ra roughness: 290.64 μin .

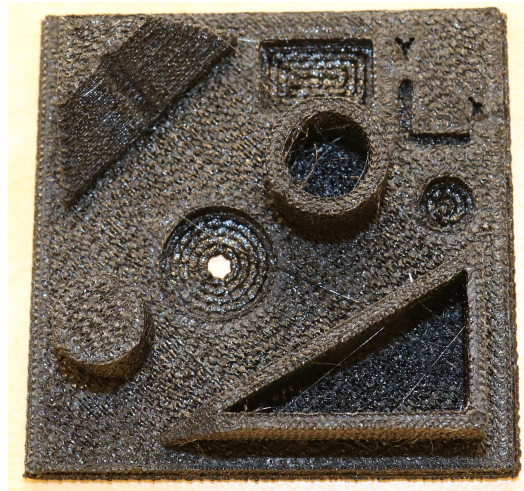


(d) 0.0325 g vibration at 40.7 Hz. No isolation. Ra roughness: 849.71 μin .

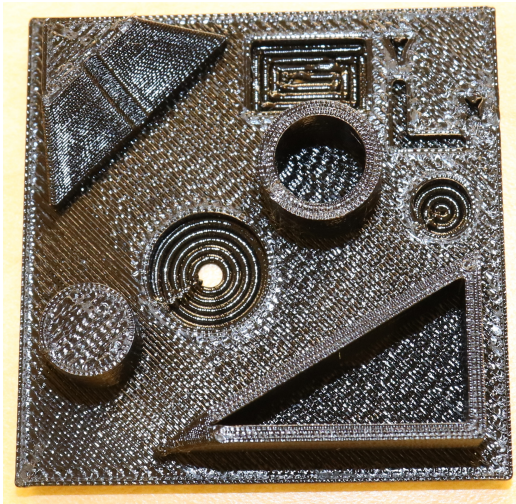
Figure B.12: Top-view of PETG part photos for various testing scenarios.



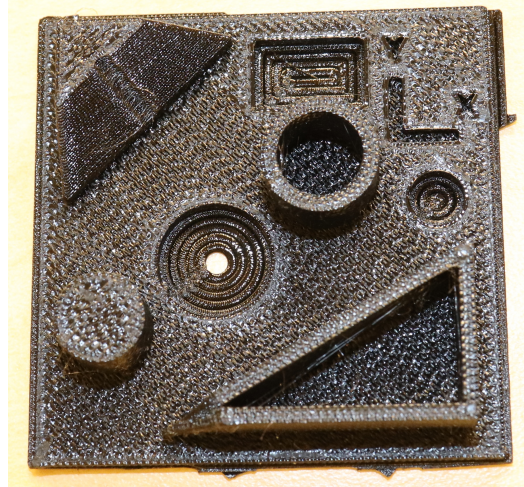
(a) No vibration. No isolation. Ra roughness: 237.65 μin .



(b) 0.13 g vibration at 40.7 Hz. No isolation. Ra roughness: 946.15 μin .

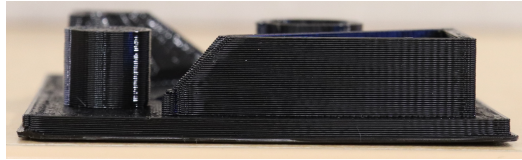


(c) 0.0325 g vibration at 40.7 Hz. 3 sponge hockey puck isolation. Ra roughness: 290.64 μin .



(d) 0.0325 g vibration at 40.7 Hz. No isolation. Ra roughness: 849.71 μin .

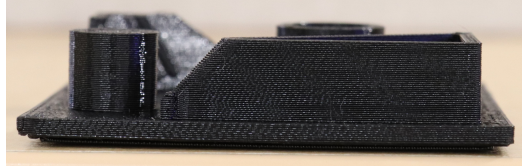
Figure B.13: Top-view of PETG part photos with camera flash for various testing scenarios.



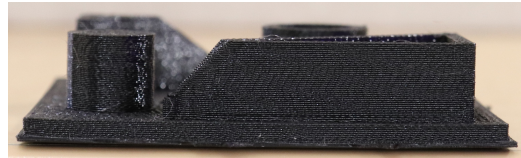
(a) No vibration. No isolation. Ra roughness: 237.65 μin .



(b) 0.13 g vibration at 40.7 Hz. No isolation. Ra roughness: 946.15 μin .

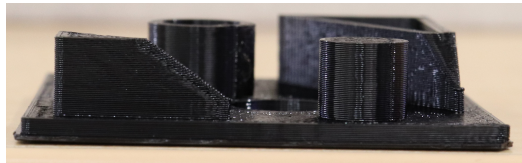


(c) 0.0325 g vibration at 40.7 Hz. 3 sponge hockey puck isolation. Ra roughness: 290.64 μin .

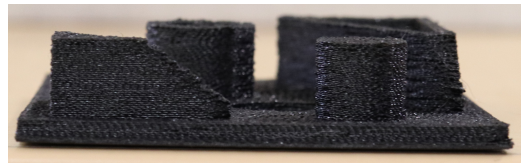


(d) 0.0325 g vibration at 40.7 Hz. No isolation. Ra roughness: 849.71 μin .

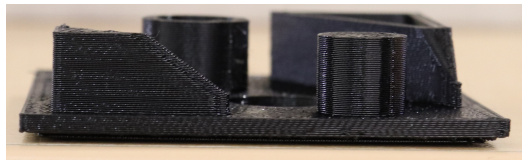
Figure B.14: Front-view of PETG part photos for various testing scenarios.



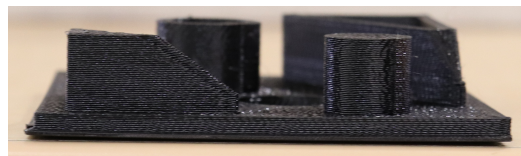
(a) No vibration. No isolation. Ra roughness: 237.65 μin .



(b) 0.13 g vibration at 40.7 Hz. No isolation. Ra roughness: 946.15 μin .



(c) 0.0325 g vibration at 40.7 Hz. 3 sponge hockey puck isolation. Ra roughness: 290.64 μin .



(d) 0.0325 g vibration at 40.7 Hz. No isolation. Ra roughness: 849.71 μin .

Figure B.15: Left-view of PETG part photos for various testing scenarios.